

DISSERTATION

THREE-DIMENSIONAL WATER VAPOR RETRIEVAL USING A NETWORK OF SCANNING COMPACT MICROWAVE RADIOMETERS

Submitted by

Sharmila Padmanabhan

Department of Electrical and Computer Engineering

In partial fulfillment of the requirements

for the Degree of Doctor of Philosophy

Colorado State University

Fort Collins, Colorado

Spring 2009

UMI Number: 3374610

INFORMATION TO USERS

The quality of this reproduction is dependent upon the quality of the copy submitted. Broken or indistinct print, colored or poor quality illustrations and photographs, print bleed-through, substandard margins, and improper alignment can adversely affect reproduction.

In the unlikely event that the author did not send a complete manuscript and there are missing pages, these will be noted. Also, if unauthorized copyright material had to be removed, a note will indicate the deletion.

UMI[®]

UMI Microform 3374610
Copyright 2009 by ProQuest LLC
All rights reserved. This microform edition is protected against
unauthorized copying under Title 17, United States Code.

ProQuest LLC
789 East Eisenhower Parkway
P.O. Box 1346
Ann Arbor, MI 48106-1346

COLORADO STATE UNIVERSITY

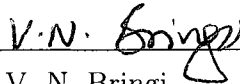
November 17, 2008

WE HEREBY RECOMMEND THAT THE DISSERTATION PREPARED UNDER OUR SUPERVISION BY SHARMILA PADMANABHAN ENTITLED THREE-DIMENSIONAL WATER VAPOR RETRIEVAL USING A NETWORK OF SCANNING COMPACT MICROWAVE RADIOMETERS BE ACCEPTED AS FULFILLING IN PART REQUIREMENTS FOR THE DEGREE OF DOCTOR OF PHILOSOPHY.

Committee on Graduate Work



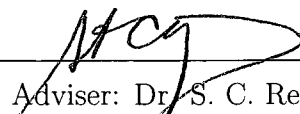
Dr. J. Vivekanandan



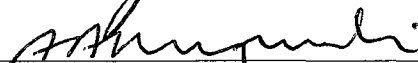
Dr. V. N. Bringi



Dr. C. Kummerow



Adviser: Dr. S. C. Reising



Department Head: Dr. A. A. Maciejewski

ABSTRACT OF DISSERTATION

THREE-DIMENSIONAL WATER VAPOR RETRIEVAL USING A NETWORK OF SCANNING COMPACT MICROWAVE RADIOMETERS

Quantitative precipitation forecasting is currently limited by the paucity of observations on sufficiently fine temporal and spatial scales. In particular, convective storms have been observed to develop in regions of strong and rapidly evolving moisture gradients that vary spatially on sub-meso γ scales (2 - 5 km). Therefore, measurements of water vapor aloft with high time resolution and sufficient spatial resolution have the potential to improve forecast skill for the initiation of convective storms. Such measurements may be used for assimilation into and validation of numerical weather prediction (NWP) models.

Currently, water vapor density profiles are obtained using in-situ sensors on radiosondes and remotely using lidars, GPS ground-based networks, GPS radio occultation from satellites and a relatively small number of space-borne microwave and infrared radiometers. In-situ radiosonde measurements have excellent vertical resolution but are severely limited in temporal and spatial coverage. In addition, each radiosonde takes 45-60 minutes to rise from ground level to the tropopause, and is typically advected by upper-level winds up to tens of km horizontal displacement from its launch site. Tomographic inversion applied to ground-based measurements of GPS wet delay is expected to yield data with 0.5-1 km vertical resolution at 30-minute intervals. COSMIC and CHAMP satellites in low earth orbit (LEO) provide measurements with 0.1-0.5 km vertical resolution at 30-minute intervals but only 200-600 km horizontal resolution, depending on the magnitude of the path-integrated refractivity. Microwave radiometers in low-earth orbit provide reasonable vertical resolution (2 km) and mesoscale horizontal resolution (20 km) with long repeat times.

Both the prediction of convective initiation and quantitative precipitation require knowledge of water vapor variations on sub-meso γ scales (2-5 km) with update times on the order of a few tens of minutes. Due to the relatively high cost of both commercially-available

microwave radiometers for network deployment and rapid radiosonde launches with close horizontal spacing, such measurements have not been available. Measurements using a network of multi-frequency microwave radiometers can provide information to retrieve the 3-D distribution of water vapor in the troposphere. An Observation System Simulation Experiment (OSSE) was performed in which synthetic examples of retrievals using a network of radiometers were compared with results from the Weather Research Forecasting (WRF) model at a grid scale of 500 m. These comparisons show that the 3-D water vapor field can be retrieved with an accuracy varying from 15-40% depending on the number of sensors in the network and the location and time of the *a priori*.

To deploy a network of low cost radiometers, the Compact Microwave Radiometer for Humidity profiling (CMR-H) was developed by the Microwave Systems Laboratory at Colorado State University. Using monolithic microwave integrated circuit technology and unique packaging yields a radiometer that is small (24 x 18 x 16 cm), light weight (6 kg), relatively inexpensive and low-power consumption (25-50 W, depending on weather conditions). Recently, field measurements at the DOE Atmospheric Radiation Measurement (ARM) Southern Great Plains site in Oklahoma have demonstrated the potential for coordinated, scanning microwave radiometers to provide 0.5-1 km resolution both vertically and horizontally with sampling times of 15 minutes or less. This work describes and demonstrates the use of algebraic reconstruction tomography to retrieve the 3-D water vapor field from simultaneous brightness temperatures using radiative transfer theory, optimal estimation and Kalman filtering.

Sharmila Padmanabhan
Electrical and Computer Engineering Department
Colorado State University
Fort Collins, CO 80523
Spring 2009

ACKNOWLEDGMENTS

First and foremost, I would like to express my gratitude to Professor Steven C. Reising, my advisor, for supporting and promoting my efforts with enthusiasm and dedication. Secondly, I would like to give my wholehearted thanks to Dr. J. Vivekanandan, my advisor at the National Center for Atmospheric Research (NCAR), for his cheerful guidance and valuable suggestions. I thank Professors Kummerow, Bringi and Chandra for their valuable scientific suggestions and for serving on my dissertation committee.

I would like to thank Brad Orr, John Schatz, Dave Breedlove and Dan Rusk of Atmospheric Radiation Measurement (ARM), for hosting and assisting in our experiments at Billings, OK. I would also like to thank the METAWAVE team in Italy, that includes Dr. N. Pierdicca, Dr. D. Cimini and Dr. F. Marzano, for their help and support during the field measurements.

Current and past graduate students of the Microwave Systems laboratory have contributed to this work. I would like to thank Flavio Iturbide-Sanchez, Willow Foster and Swaroop Sahoo for their help and support during the fabrication and deployment of the radiometers at Boulder, Oklahoma and Rome, Italy.

I am grateful to my parents, Padmanabhan and Parvathy, for their love and support. I thank my sister, Dr. Sandhya Padmanabhan, for her constant motivation and always believing in my potential for success. Finally, I want to thank my husband, Dr. Dinesh Ramakrishnan, for being very patient and supportive.

Sharmila Padmanabhan

DEDICATION

To my father, Padmanabhan, mother, Parvathy, sister, Sandhya and husband
Dinesh.

Contents

1	Introduction	1
1.1	Scientific Background	1
1.2	Summary of Chapters	6
1.3	Contributions of this Dissertation	8
2	Compact Microwave Radiometer for Humidity Profiling (CMR-H)	10
2.1	8-by-16 Box Horn Array	12
2.1.1	Beam Efficiency	12
2.1.2	Spatial Resolution	14
2.1.3	Losses	15
2.1.4	Effect of Radome Reflectivity on Antenna Performance	16
2.2	CMR-H3 : Design Modifications	20
2.3	Sensitivity of CMR-H3 Radiometer	28
3	3-D Water Vapor Retrieval Using Tomographic Inversion	34
3.1	Inversion of Single-Radiometer Brightness Temperatures	35
3.2	Algebraic Tomographic Reconstruction to Retrieve the 3-D Water Vapor Field	41

3.2.1	Forward Model	43
3.2.2	Inversion: Optimal Estimation and Kalman Filtering	46
3.2.3	Kriging	50
4	Observation System Simulation Experiment (OSSE)	53
4.1	Weather Research and Forecasting Model	54
4.2	Spatial Scales of Variation of Water Vapor Densities	58
4.3	OSSE: Three Radiometer Network	60
4.3.1	Measurement Configuration	60
4.3.2	OSSE Results	62
4.4	Retrieval Sensitivity	62
4.4.1	Retrieval Sensitivity to the Time of the <i>A-priori</i> Profile	65
4.4.2	Retrieval Sensitivity to the Location of <i>A-priori</i> Profile	66
4.4.3	Retrieval Sensitivity to the Number of Radiometers in the Network	67
5	2-D and 3-D Field Measurements	72
5.1	2-D Water Vapor Measurement	72
5.2	3-D Water Vapor Measurement	75
5.2.1	3-D Measurements in Oklahoma	75
5.2.2	3-D Measurements in Rome, Italy	76
6	Summary and Suggestions for Future Work	86
6.1	Summary	86
6.2	Suggestions for Future Work	88

A	Field Operation of CMR-H	91
A.0.1	Hardware connections	92
A.0.2	Temperature control	93
A.0.3	Communication with radiometer embedded computer	93
A.0.4	Positioner Control	94
A.0.5	Calibration target control	98

List of Figures

2.1	Photo of the Compact Microwave Radiometer for Humidity Profiling (CMR-H)	11
2.2	E-plane antenna pattern of the 8-by-16 box-horn array at 22.12 GHz	13
2.3	Normalized radiation pattern of the 8 by 16 box horn array	14
2.4	Mismatch planes between the radiometer and the radome	18
2.5	Reflection coefficient of 5 mil thick Lexan as a function of frequency .	19
2.6	Comparison of tipcurve measured at 22.12 GHz with (red circles) and without (black squares) radome	20
2.7	Comparison of tipcurve measured at 22.67 GHz with (red circles) and without (black squares) radome	21
2.8	Comparison of tipcurve measured at 23.25 GHz with (red circles) and without (black squares) radome	21
2.9	Comparison of tipcurve measured at 24.50 GHz with (red circles) and without (black squares) radome	22
2.10	Photo of the CMRH3 multi-chip-module	24
2.11	Photo of the isolator used in CMR-H3	25
2.12	S-parameter measurements of the isolator used in CMR-H3	26

2.13	Block Diagram of the third Compact Microwave Radiometer for Humidity Profiling (CMR-H3)	27
2.14	Sensitivity of CMR-H at 22.12 GHz	29
2.15	Sensitivity of CMR-H at 22.67 GHz	30
2.16	Sensitivity of CMR-H at 23.25 GHz	31
2.17	Sensitivity of CMR-H at 24.50 GHz	32
3.1	Weighting function at the four CMR-H frequencies	37
3.2	Comparison of water vapor density profiles measured by radiosonde with those retrieved from microwave brightness temperatures measured by CMR-H and Radiometrics WVP-1500 radiometers.	42
3.3	(a) Illustration of scanning angles in a 2-D plane and (b) The size of overlapping pixels.	45
3.4	The number of eigenvalues of the Jacobian matrix vs. the number of elevation angles.	48
4.1	WRF model output of temperature	55
4.2	WRF model output of water vapor mixing ratio	56
4.3	Semi-variograms of water vapor density in WRF output at (a) 3 km and (b) 5 km above ground level at 3:00 UTC	59
4.4	Time series of water vapor density correlation distance inferred from the semi-variograms in Figure 4 at (a) 3 km and (b) 5 km above ground level (AGL).	60
4.5	Equilateral triangular topology for a three-node scanning radiometer network with a 10-km nearest-neighbor distance.	63

4.6	(a) WRF model output of the water vapor density at 3.4 km above ground level (AGL) over northwest Indiana at 3:00 UTC. (b) Percentage error of the water vapor density retrieved from synthetic brightness temperature measurements also at 3.4 km AGL with WRF model output at 2:00 UTC used as the <i>a priori</i>	64
4.7	(a) WRF model output of the water vapor density at 3.4 km above ground level (AGL) over northwest Indiana at 3:00 UTC. (b) Water vapor density in g/m^3 retrieved from synthetic brightness temperature measurements also at 3.4 km AGL with WRF model output at 2:00 UTC used as the <i>a priori</i>	64
4.8	Histogram of water vapor density retrieval errors in Figure 4.6 for 3.4 km AGL.	65
4.9	(a) WRF model output of the water vapor density at 3.4 km above ground level (AGL) over northwest Indiana at 3:00 UTC. (b) Percentage error of the water vapor density retrieved from synthetic brightness temperature measurements also at 3.4 km AGL with WRF model output at 2:30 UTC used as the <i>a priori</i>	66
4.10	(a) WRF model output of the water vapor density at 3.4 km above ground level (AGL) over northwest Indiana at 3:00 UTC. (b) Percentage error of the water vapor density retrieved from synthetic brightness temperature measurements also at 3.4 km AGL with WRF model output at 2:00 UTC at one corner of the triangle used as the <i>a priori</i> . . .	67

4.11 (a) WRF model output of the water vapor density at 3.4 km above ground level (AGL) over northwest Indiana at 3:00 UTC. (b) Percentage error of the water vapor density retrieved from synthetic brightness temperature measurements also at 3.4 km AGL with WRF model output at 2:00 UTC at the median point of the triangle used as the <i>a priori</i> .	68
4.12 Optimal hexagonal topology for a scanning six radiometer network with a 10 km between adjacent nodes	69
4.13 (a) WRF model output of the water vapor density at 2.2 km above ground level (AGL) over northwest Indiana at 3:00 UTC. (b) Percentage error of the water vapor density retrieved from synthetic brightness temperature measurements also at 2.2 km AGL with WRF model output at 2:00 UTC used as the <i>a priori</i>	70
4.14 (a) WRF model output of the water vapor density at 3.4 km above ground level (AGL) over northwest Indiana at 3:00 UTC. (b) Percentage error of the water vapor density retrieved from synthetic brightness temperature measurements also at 3.4 km AGL with WRF model output at 2:00 UTC used as the <i>a priori</i>	70
4.15 Histogram of water vapor density retrieval errors in Figure 4.14 for 3.4 km AGL.	71
5.1 Comparison of RAOB and CMR-H retrieved water vapor density profile on October 9, 2007.	73
5.2 Trajectory of the RAOB launched on Oct 9, 2007	74
5.3 2-D water vapor image retrieved in the region between two CMR-H radiometers at 6-km spacing.	74

5.4	Map of the demonstration network of three CMR-H radiometers deployed at the ARM-SGP site near Billings, OK, USA. The three azimuth angles scanned by each radiometer are shown as yellow dashed line segments. CMR-H2 was deployed at the ARM-SGP Central Facility.	77
5.5	Image of water vapor density near the ARM-SGP Central Facility in g/m ³ retrieved from brightness temperature measurements at 2 km AGL at 17:30 UTC on August 31, 2008.	78
5.6	Image of water vapor density near the ARM-SGP Central Facility in g/m ³ retrieved from brightness temperature measurements at 3 km AGL at 17:30 UTC on August 31, 2008.	79
5.7	Image of water vapor density near the ARM-SGP Central Facility in g/m ³ retrieved from brightness temperature measurements at 4 km AGL at 17:30 UTC on August 31, 2008.	80
5.8	Time Series of water vapor densities retrieved at 2 km AGL from 16:30 UTC to 17:30 UTC on August 31, 2008.	81
5.9	Map of the demonstration network of three CMR-H radiometers deployed at the Rome, Italy. The three azimuth angles scanned by each radiometer are shown as red, blue and green dashed line segments.	83
5.10	Photo of CMR-H2 mounted on the roof of the Dept. of Electronics Engineering at the University of La-Sapienza in Rome, Italy.	84
5.11	Thermal stability of CMR-H2 over 20,000 s.	85
5.12	Thermal stability of CMR-H3 over 20,000 s.	85
A.1	Temperature Controller Window.	95
A.2	CMR-H server and biasing control window.	96

A.3 Positioner Controller Window	97
A.4 Calibration load logger window	98

List of Tables

1.1	Remote Sensing Measurements of Water Vapor	5
2.1	Radiometer Specifications	12
5.1	Radiometer deployment locations in Oklahoma	76

Chapter 1

Introduction

1.1 Scientific Background

Water vapor is both the most abundant and most variable greenhouse gas in the atmosphere. It affects the Earth radiation budget, energy transfer, cloud formation, and precipitation distribution. In terms of radiation transfer, water vapor absorbs both downwelling solar and upwelling longwave radiation. In terms of energy transfer, the latent heat of vaporization is a principal mechanism for the transport of energy from the equatorial regions to higher latitudes. The energy released when vapor condenses to form clouds is a substantial driver of the dynamics of the atmosphere. This latent heat release modifies the vertical stability of the atmosphere, influencing weather systems and their associated precipitation patterns. Improving and extending the available techniques of water vapor measurement has been identified as a key research area by the U.S. Weather Research Program [1]. Convection in the absence of external forcing is directly related to the convergence of moisture in the troposphere. This convergence of moisture aids in the removal of convective inhibition (CIN) in a

strict parcel lifting theory of convection. Xin and Reuter [2] simulated a convective storm in the absence of vertical wind shear using an axisymmetric model. The result of this simulation was to reveal that rainfall is controlled by the moisture convergence below clouds. They also showed that the timing and quantity of rainfall varied with the depth of the convergence zone, given a fixed vertical mass flux. Shallow convergence zones injected more moisture above the level of free convection and subsequently increased the rainfall within the simulation. In another study of convection in the absence of larger scale forcing, [3] determined that once convection was well developed, the strength of the convection (defined as the maximum vertical velocity (w_{max})) was 2.5 times more sensitive to variations in moisture than temperature in the convective boundary layer.

Sensitivity studies [4, 5] indicate that a lack of accurate observational moisture measurements throughout the troposphere limits the forecast of severe storms over time scales as short as 30 minutes. It was also reported that the variation in water vapor above the convective boundary layer directly affected the entrainment and vertical velocity characteristics of the storm.

Water vapor in the troposphere is highly variable, both temporally and spatially. The vertical profile of water vapor is typically measured using radiosondes. However, radiosondes are launched operationally from U.S. National Weather Service locations separated by 60 km to a few hundred kilometers. Radiosondes are not reusable, restricting their launch to twice daily, 0 and 12 UTC, at most stations.

Improving quantitative precipitation forecasting is an important and scientifically challenging objective [6]. Improvements are needed in forecasting of the location and amount of precipitation, as well as in understanding the underlying processes and mechanisms of convective initiation [7]. Water vapor measurements with high spatial

and temporal resolution are needed for direct assimilation into numerical weather prediction (NWP) models.

Despite their importance to quantitative precipitation forecasting, current observational technologies for measuring water vapor are inadequate, partly because tropospheric water vapor content can vary by three orders of magnitude. For example, large humidity biases in radiosonde data that often exceed 5% throughout the troposphere have been recently identified and partially corrected [8, 9]. The capacitive polymer hygrometer introduced dry bias errors of 6.8% in RS80 radiosonde data. A humidity sensor boom cover introduced by Vaisala in late 2000 reduced this error to 3.9% [10]. Residual dry bias errors in the current RS92 radiosondes are still larger during the day than at night by 5%-7% [11]. These dry bias errors have a significant impact on long-term climate trends. When not sufficiently corrected, such biases can change the quantitative and qualitative interpretation of the spatial and temporal variations in CAPE (Convective Available Potential Energy) and CIN (Convective Inhibition) [10].

Currently, water vapor density profiles are obtained in-situ using hygrometers on radiosondes and remotely using lidars [12, 13], GPS ground [14, 15] networks and satellite radio occultation [16, 17], as well as a small number of space-borne microwave radiometers [18, 19]. In-situ radiosonde measurements have excellent vertical resolution but are severely limited in temporal and spatial coverage. In addition, each radiosonde takes 45-60 minutes to ascend from the ground to the tropopause. Differential-absorption lidars measure water vapor with comparable resolution to that of radiosondes during only clear-sky conditions from a very limited number of sites [20]. Tomographic inversion applied to ground-based measurements of GPS slant path delay is expected to yield 0.5-1 km vertical resolution at 30-minute intervals

[14, 15, 21]. In contrast, microwave radiometers can provide nearly continuous measurements of weighted, path-integrated water vapor and liquid water in the troposphere. Ground-based microwave radiometers perform such measurements with high temporal resolution and in both clear and cloudy weather conditions. Currently, water vapor profiling by commercial radiometers is limited to zenith-pointing observation [22, 23]. A network of scanning radiometers is needed to retrieve the 3-D water vapor field with improved spatial and temporal resolution. Radiometer measurements of the same volume from multiple perspectives, i.e. different sensor nodes, need to be combined to retrieve the 3-D water vapor field as a function of time. The principal technological challenge posed by the state of the art is the lack of availability of microwave radiometers with small mass and volume at low cost. Microwave radiometers for atmospheric profiling are commercially available at roughly \$200 K each, making a significant network of this kind prohibitive. For example, UCAR's extensive International Water Vapor Project (IHOP 2002) included experiments aboard six aircraft, seven radars, five lidars and many radiosondes, but only two radiometers [24]. The second challenge is to combine the measurements from multiple radiometers to retrieve the 3-D field of water vapor in the atmosphere. Meeting these challenges will improve temporal and spatial sampling of important thermodynamic variables affecting short- and medium-scale weather prediction in the troposphere. A follow-on need created by this new technology is appropriate variational assimilation to initialize and test numerical weather prediction models with these newly available higher-resolution data.

Table 1.1 provides characteristics of currently available water vapor measurements. COSMIC (Constellation Observing System for Meteorology, Ionosphere and Climate) moisture products using the GPS radio occultation technique have a vertical resolu-

Table 1.1: Remote Sensing Measurements of Water Vapor

Remote Sensor	Horizontal Resolution (km)	Vertical Resolution (km)	Temporal Resolution (hr)	Frequency Band
GPS ground network	50	0.5-1 (expected)	0.5	L-band
Radiosondes	~ 70 km spacing	0.1-0.5	12	In-situ
COSMIC	200	0.1-0.5	0.5	L-band
AMSU-B	20	2	12	G-band
Network of CMR-Hs	0.5-1	0.5-1	15 min	K-band

tion on the order of 100-500 m. However, the horizontal resolution of the retrieved moisture profiles ranges from 200-600 km. The prediction of convective initiation requires the knowledge of water vapor content on meso- γ scales (2-5 km) [25, 26, 27]. Measurements using a network of multi-frequency microwave radiometers have the potential to provide improved vertical, horizontal and temporal resolution of these measurements. The need for deployment of a substantial number of radiometers motivated a compact design with low mass, cost and power consumption [28]. Microwave radiometers for remote sensing are typically fabricated using waveguide and connectorized components. However, these components have large mass and volume, tending to make microwave sensors heavy and bulky, and generally difficult to reproduce. We are addressing the challenges posed by the state-of-the-art technology by utilizing commercially-available monolithic microwave and millimeter-wave Integrated Circuits (MMIC's). The major advantages of MMIC-based radiometers for remote sensing are:

- (1) Lower mass and volume than conventional waveguide- and coaxial-connector based systems,

- (2) Lower power consumption to achieve the necessary internal temperature regulation,
- (3) Highly repeatable performance from unit to unit, and
- (4) Low-cost fabrication in quantity.

The design and fabrication of MMIC-based radiometers was accomplished by the integration of MMICs into multi-chip modules and the synthesis of the required components and subsystems to realize a field-ready system. To meet these goals, we have designed innovative packaging and system integration to meet the specific requirements of passive microwave remote sensing. This new technology made a scanning network of three compact and low cost microwave radiometers realizable. This dissertation demonstrates the implementation of tomographic inversion and spatial interpolation techniques to retrieve the 3-D structure of the water vapor in the troposphere by combining the radiometer measurements of the same volume from multiple perspectives, i.e. different sensor nodes [29].

1.2 Summary of Chapters

This dissertation will discuss the retrieval of 3-D water vapor field from the brightness temperature measurements of the network of compact microwave radiometers for humidity profiling.

Chapter I will describe the importance of measurements of the 3-D water vapor field to improve the forecasting of quantitative precipitation forecasting. It will also discuss the current measurement techniques and the limited number of water vapor observations available with fine spatial and temporal resolution. The main scientific motivation for using a network of compact microwave radiometers will be outlined.

Chapter II will discuss the Compact Microwave Radiometer for Humidity (CMR-H) profiling and its features that make it highly suitable for network deployment. The new 8-by-16 box-horn array antenna will be described. A discussion of the effect of finite beamwidth and side-lobes on the radiometer measurement will be presented.

Chapter III will describe the radiative transfer theory and establish a forward model to express the brightness temperature measured by a radiometer in terms of the atmospheric state variables. A variety of inversion techniques can be used to retrieve the state variable from the brightness temperature measurement. These inversion methods will be described followed by the justification for the use of algebraic tomographic reconstruction techniques to retrieve the 3-D water vapor from the scanning measurements performed for a variety of azimuth and elevation angles.

Chapter IV will focus on the Observation System Simulation Experiment (OSSE). The Weather Research and Forecasting (WRF) model that was used to simulate the thermodynamic variables (grid resolution of 500 m) will be described in detail. The 3-D water vapor fields retrieved using the synthetic brightness temperatures for each radiometer node will be compared with the WRF model output for several altitudes above ground level.

Chapter V will describe the scanning measurements performed by two as well as three radiometers. This includes the description of 2-D water vapor images retrieved from scanning measurements of two CMR-H's as well as three station scanning network measurements performed in Atmospheric Radiation Measurement Southern Great Plains site in Billings, OK during Summer'08.

Chapter VI will provide a summary and discuss the suggestions for future work.

1.3 Contributions of this Dissertation

The contributions of this dissertation are as follows :

- Three low mass, low cost and low power consumption compact microwave radiometers for humidity profiling were developed to enable field deployment and retrieval of the 3-D water vapor field. The MMIC-based RF (radio frequency) multi-chip-modules, designed and packaged by Flavio Iturbide-Sanchez [30], were then integrated with the custom fabricated intermediate frequency (IF) section power divider, IF filters and square law detectors. The multi-chip-module in the third radiometer was upgraded to include an isolator and the IF amplifiers in the same module. A detailed discussion of the upgrades is presented in section 2.2. A compact data acquisition system and temperature control system was married to the RF-IF section giving rise to a compact, low mass, low volume microwave radiometer.
- A new technique to measure the 3-D tropospheric water vapor field is developed. Inversion of brightness temperatures measured by upward-looking, ground-based microwave radiometers allows the estimation of vertical profiles with high temporal resolution in both clear and cloudy conditions. This new technique makes use of measurements from a network of scanning CMR-Hs. Radiometer measurements of the same volume from multiple perspectives (a variety of azimuth and elevation angles), i.e. different sensor nodes, will be combined using tomographic inversion to retrieve the 3-D water vapor field as a function of time. The retrieval accuracy of the technique is estimated by performing an Observation System Simulation Experiment.

- The first field measurements were performed to retrieve the 3-D water vapor field in the triangular domain scanned by the three radiometers. A three radiometer network was deployed in Southern Great Plains region of the Central United States during Summer 2008. The measurements collected from a network of radiometer stations are combined to derive the three dimensional distribution of water vapor with horizontal scales of less than 2 km and vertical scales of 0.5 -1 km using tomographic inversion techniques.

Chapter 2

Compact Microwave Radiometer for Humidity Profiling (CMR-H)

This chapter describes the upgrades made to the multi-chip-module (MCM) implemented in the third compact microwave radiometer for humidity profiling (CMR-H), designed at the Microwave Systems Laboratory at the Colorado State University. The MCM used in CMR-H1 and CMR-H2 were designed by Flavio Iturbide-Sanchez and is described in great detail in his Ph.D. dissertation [30]. A new antenna with a narrower beamwidth is also described. This 8-by-16 box-horn array antenna replaced the 4-by-8 array antenna in order to facilitate a reconstruction of the 3-D water vapor field with fine resolution (0.5-1 km) from the measured brightness temperature measurements.

Three Compact Microwave Radiometers for Humidity Profiling (CMR-H) were designed, fabricated and tested in the Microwave Systems Laboratory at Colorado State University. CMR-H uses a filter bank configuration and measures four channels (22.12, 22.67, 23.25 and 24.50 GHz) near the 22 GHz water vapor absorption line.

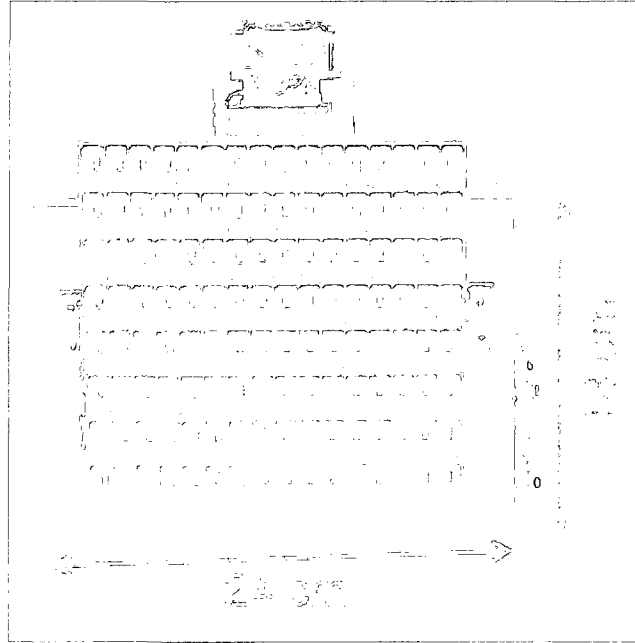


Figure 2.1: Photo of the Compact Microwave Radiometer for Humidity Profiling (CMR-H)

CMR-H was implemented using Monolithic Microwave Integrated Circuit (MMIC) components in order to achieve low mass, low cost and low power consumption. These features make it highly suitable for network deployment. A 8-by-16 box horn array antenna was used to reduce the mass and volume, while maintaining comparable performance to scalar horn antennas. Figure 2.1 is a photo of CMR-H with a 8-by-16 box horn antenna. Table 2.1 shows the CMR-H specifications. Appendix A describes the field deployment of the CMR-H mounted atop a pan-tilt positioner and the control software for the temperature control and calibration target.

Table 2.1: Radiometer Specifications

Parameter	CSU CMR-H
Frequency Channels (GHz)	22.12, 22.67, 23.25 and 24.5
Sensitivity (K) @ 1 s integration time	0.2 - 0.3
3-dB Antenna Beamwidth (°)	3.0 - 4.0
Internal Calibration	noise diode and reference load
External Calibration	tipping curve and Microwave absorber

2.1 8-by-16 Box Horn Array

The 4-by-8 box horn array with a 7-8° beamwidth was replaced by a 8-by-16 box horn array with a 3-4° degree beamwidth. Figure 2.2 shows the antenna pattern of the 8-by-16 box horn array at 22.12 GHz. To perform tomographic reconstruction of the 3-D water field with fine spatial resolution, a radiometer antenna is used to satisfy the following requirements:

- High Main Beam Efficiency
- Narrow Beamwidth
- Low Ohmic losses

2.1.1 Beam Efficiency

The main beam efficiency is the ratio of the temperature measured by the main beam to the total antenna temperature. Similarly, the side lobe efficiency is the ratio of the

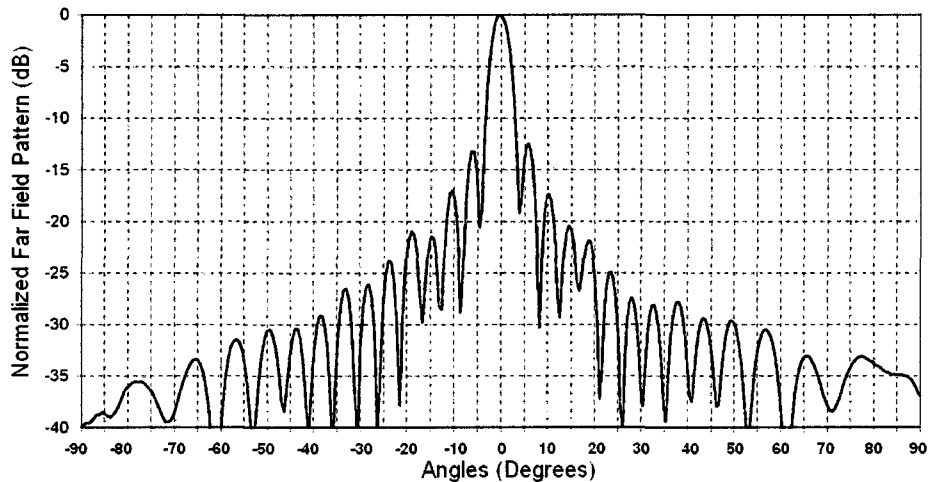


Figure 2.2: E-plane antenna pattern of the 8-by-16 box-horn array at 22.12 GHz

temperature measured by the side lobes to the antenna temperature. Antennas with high main-beam efficiency are desired when designing microwave radiometers. In the case of an ideal antenna the main beam efficiency and the efficiency of the side lobes is equal to one and zero, respectively. Under this condition, the desired brightness temperature of the main beam area, can be obtained directly from the radiometer measurement, because $T_A = T_{B_{MB}}$, where T_A is the antenna temperature and $T_{B_{MB}}$ is the average brightness temperature within the main beam. The desired quantity is $T_{B_{MB}}$ but the direct radiometer antenna measurement yields T_A , which includes contributions from side lobes, as presented in 2.1.

$$T_A = T_{B_{MB}}\epsilon_{MB} + T_{b_{SL}}\epsilon_{SL} + T_{b_{CP}} \quad (2.1)$$

Where $T_{b_{SL}}$ is the brightness temperature collected from side lobes, ϵ_{MB} is the main beam efficiency, ϵ_{SL} is the side lobe efficiency and $T_{b_{CP}}$ represents the contribution of the crosspolar component. The largest errors are due to side lobes close to

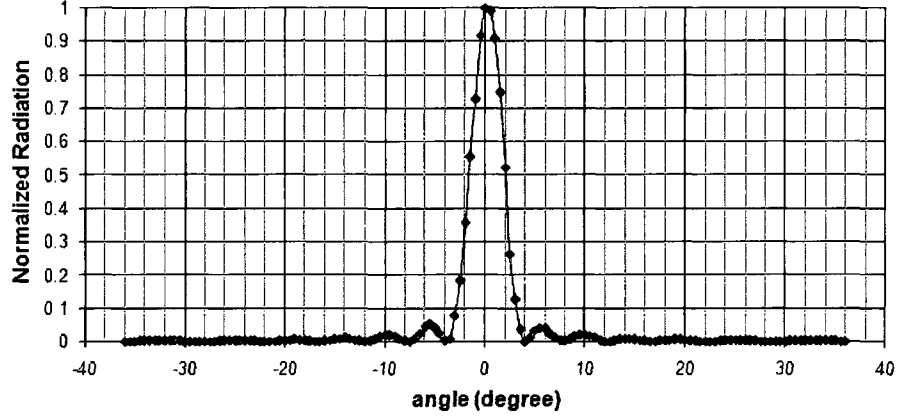


Figure 2.3: Normalized radiation pattern of the 8 by 16 box horn array

the main beam. Box-horn array and scalar horn antenna have acceptable main beam efficiency as compared to the lens antenna. However, the box-horn array antenna presents high side lobe levels. Those contributions have to be considered, especially when measuring targets with low brightness temperatures. The normalized radiation pattern is shown in figure 2.3. The effect of the sidelobes is calculated as

$$\begin{aligned}
 T_{sky}(\theta) = & T_A(\theta)RI_{mainbeam} + T_A(\theta - 6)RI_{Sidelobe1left} + T_A(\theta + 6)RI_{Sidelobe1right} \\
 & + T_A(\theta - 10)RI_{Sidelobe2left} + T_A(\theta + 10)RI_{Sidelobe2right} + T_A(\theta - 24)RI_{backlobeleft} \\
 & + T_A(\theta + 24)RI_{backloberight})/RI_{total}
 \end{aligned} \tag{2.2}$$

where RI is the radiation intensity in W.

2.1.2 Spatial Resolution

Spatial resolution can be defined as the footprint size, or the diameter of the antenna's main beam projected in some plane in the space. The spatial resolution determines

how small a scale the scene spatial variation can be resolved. However, high main beam efficiency antenna is required in order to reproduce the scene brightness variation. High spatial resolution can be achieved with narrow beamwidth, which implies large aperture antenna.

2.1.3 Losses

Ohmic and scattering losses are the two different type of losses identified in an antenna. Ohmic loss results from antenna surface resistivity, waveguide feed losses, filter losses, for example. Scattering losses result from redistribution of energy from the main lobe into other regions of the side and back lobes. The ohmic loss degrades the radiometer temperature sensitivity by increasing the effective system noise temperature as expressed in (2.3)

$$T_{sys} = T_A + (L - 1)T_P + T_{REC}L \quad (2.3)$$

Where L represents the sum of the total ohmic losses of the antenna and the input transmission line combined into one element, T_P is the physical temperature of the lossy element and T_{REC} is the equivalent noise temperature of the receiver.

From (2.3) observe that ohmic loss L increases the effective receiver noise temperature and produces a noise temperature component $(L - 1)T_P$ due to self emission. In addition, for radiometer systems with large values of T_{REC} , the loss L has an important effect in the increment of the latter factor of 2.3. This factor is the dominant term in degrading the sensitivity of the radiometer. Consequently, ohmic loss deteriorates the calibration accuracy of a radiometer due to the self emission term because both the physical temperature of the lossy element and the magnitude of the loss

contain some uncertainties. Although ohmic losses degrade the antenna gain, it does not affect the spatial resolution, as long as it is not direction dependent.

Non-ohmic losses are related to the redistribution of energy and could affect the beamwidth, main beam efficiency, and the temperature sensitivity. For example, the scattering loss reduces the energy received by the antenna and degrades the radiometer sensitivity in the same factor. This is the case of the reflections caused by impedance mismatch, which deteriorates the sensitivity of the radiometer.

In the case of the box horn array antenna the losses in the feed network and the relatively low impedance mismatch are examples of ohmic and scattering losses, respectively. The uncertainty in the radiometer sensitivity due to ohmic losses can be reduced by controlling the physical temperature of the antenna. In the case of the lens antenna, scattering losses are responsible for the low value of main beam efficiency in this antenna. The poor main beam efficiency of this antenna contributes to degradation in the sensitivity of the radiometer.

2.1.4 Effect of Radome Reflectivity on Antenna Performance

A radome is used to cover the box horn array antenna in order to avoid the exposure of the waveguide slots while operating in the field. Moisture and other particulates can enter the system and destroy circuit boards and also cause changes to the path length in the power combining network causing a phase error in the power combined output of the antenna. A 5 mil thick Lexan is used to protect the 8-by-16 box horn array antenna. The presence of the radome causes an error in the measured brightness temperature caused by the reflectivity of lexan. An approximate expression was derived to calculate this error when viewing a microwave absorber at ambient

temperature. This analysis is similar to that used for estimating the error in measured brightness temperature due to reflection from calibration targets [31]. We have to take into account the equivalent noise temperature of the first LNA which is affected by all the mismatches between the antenna and the LNA. We consider two mismatch planes between the Lexan and the first LNA as shown in figure 2.4. Planes 1 and 2 are for the Lexan and the antenna, respectively. p_{eh1} and p_{eh2} are the mismatch power due to the system noise temperature as shown in (2.9) and (2.10). M_1 and M_2 are the mismatch factors. The reflection coefficient of the antenna, Γ_{ant} is 0.25 calculated from the return loss (~ 12 dB). The reflection coefficient of Lexan is

$$\Gamma_{Lexan} = \frac{\frac{Z_L + jZ_0 \tan \frac{2\pi f 10^9 \text{width}_{m1}}{c} Z_0}{Z_0 + jZ_L \tan \frac{2\pi f 10^9 \text{width}_{m1}}{c}} - Z_L}{\frac{Z_L + jZ_0 \tan \frac{2\pi f 10^9 \text{width}_{m1}}{c} Z_0}{Z_0 + jZ_L \tan \frac{2\pi f 10^9 \text{width}_{m1}}{c}} + Z_L} \quad (2.4)$$

where width_{m1} is 5 mil, f varies from 22 to 26 GHz, ϵ_r is equal to 2.93, Z_L in Ω s is the impedance of free space is

$$Z_L = \sqrt{\frac{\mu_0}{\epsilon_0}} = \sqrt{\frac{4\pi \times 10^{-7}}{8.85 \times 10^{-12}}} \quad (2.5)$$

and Z_0 in Ω s is

$$Z_0 = \frac{\mu_0}{\sqrt{\mu_0 \epsilon_0} \sqrt{\epsilon(1 - j0.0106)}} \quad (2.6)$$

The mismatch factors for plane 1 and 2 is

$$M_1 = [1 - |\Gamma_{Lexan}|^2] \frac{[1 - |\Gamma_{ant}|^2]}{[1 - |\Gamma_{Lexan} \Gamma_{ant}|^2]} \quad (2.7)$$

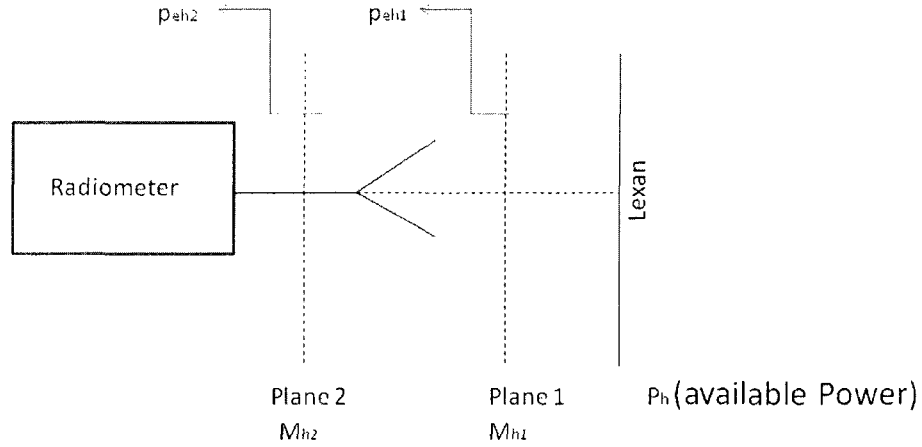


Figure 2.4: Mismatch planes between the radiometer and the radome

$$M_2 = [1 - |\Gamma_{ant}|^2] \frac{[1 - |\Gamma_{rad}|^2]}{[1 - |\Gamma_{rad}\Gamma_{ant}|]^2} \quad (2.8)$$

The powers added to the incident power due to the mismatch factors in Watts are

$$p_{eh1} = K M_{h1} T_{sys} B \quad (2.9)$$

$$p_{eh2} = K M_{h2} T_{sys} B \quad (2.10)$$

where T_{sys} , the system noise temperature is 800 K and K , the Boltzmann's constant is 1.38×10^{-23} and B , the bandwidth is 120 MHz. The power incident on the radome when viewing a microwave absorber (at 300 K) is

$$P_h = K(300)B \quad (2.11)$$

The power, in Watts, including the effect of the mismatches is

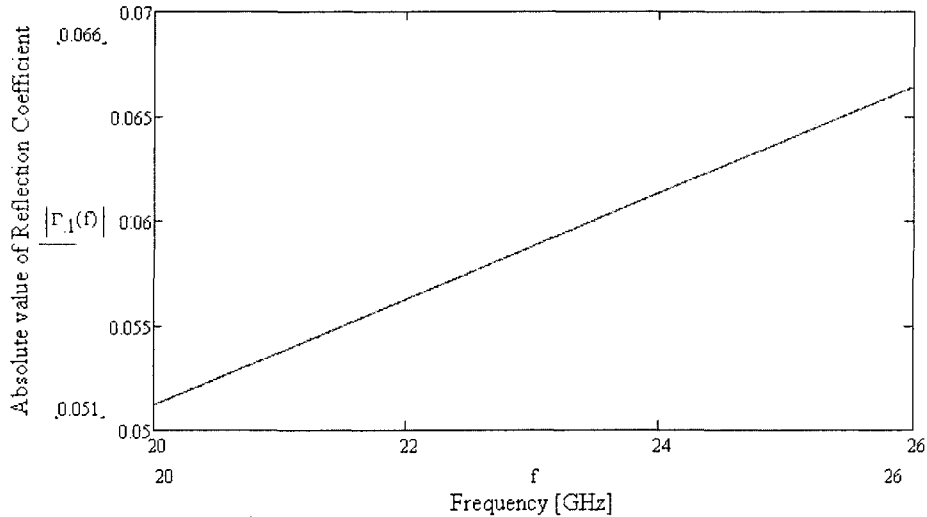


Figure 2.5: Reflection coefficient of 5 mil thick Lexan as a function of frequency

$$p_{eh1} = (M_{h1}P_h + p_{eh2})M_{h2} + p_{eh2} \quad (2.12)$$

The error in the measured temperature due to mismatches is

$$\Delta T = \frac{p_{eh1} - P_h}{KB} \quad (2.13)$$

which is calculated as $6.67 \mu\text{K}$ at 23 GHz. Rohacell HF31 is used in addition to reduce the thermal effects of the sun. This material has a reflection coefficient of 4×10^{-3} and results in an error of $5 \mu\text{K}$. The total error caused by the combination of the radome material is only $11 \mu\text{K}$. A tipcurve was performed to test the effect of the radome at the four CMR-H frequencies. A measurement was performed with the radome and without the radome. The figures 2.6, 2.7, 2.8 and 2.9 show the comparison of the tipcurves measured with and without radome at 22.12, 22.67, 23.25 and 24.50 GHz, respectively. The differences in the brightness temperatures measured with and

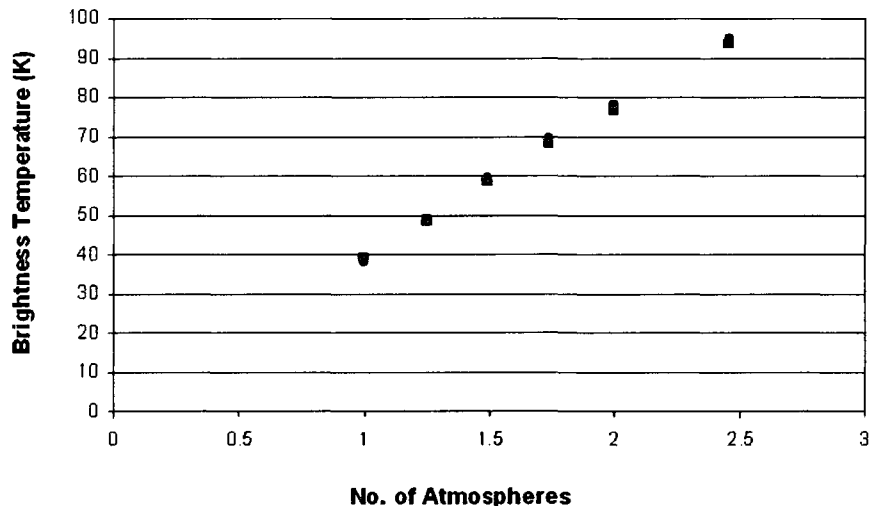


Figure 2.6: Comparison of tipcurve measured at 22.12 GHz with (red circles) and without (black squares) radome

without a radome is less than or equal to 0.3 K at all frequencies.

2.2 CMR-H3 : Design Modifications

The CMR-H3 multi-chip-module was upgraded to improve the performance of the RF-IF sections. The design modifications implemented in CMR-H3 are

1. A Single Pole Double throw (SPDT) switch MA4SW210B-1 is used in the CMR-H3 MCM instead of MA4SW310B-1 Single Pole Three Throw (SP3T) switch used in CMR-H1 and CMR-H2 MCMs. This allows for switching between the antenna and the reference 50 ohm every half Dicke cycle (50 ms). The noise diode switched off in this case acts as the 50 ohm load. The noise diode switched on is also measured every 25 s for internal calibration to minimize the effect of any small scale gain fluctuations in the system. The SPDT switch works exactly in identical manner to the SP3T switch and is controlled by the same driver as the SP3T switch.

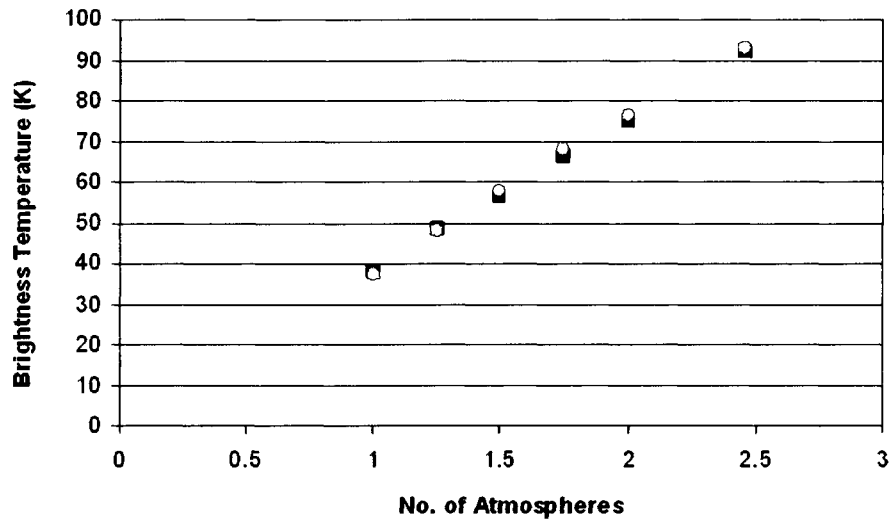


Figure 2.7: Comparison of tipcurve measured at 22.67 GHz with (red circles) and without (black squares) radome

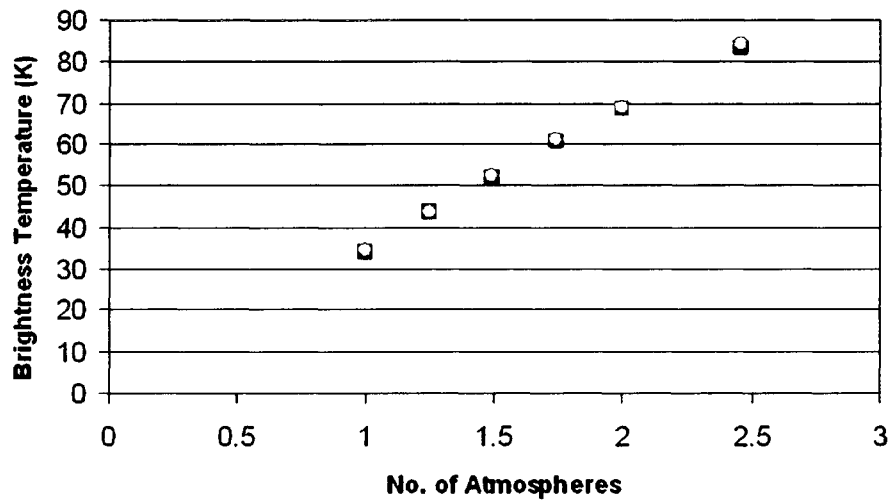


Figure 2.8: Comparison of tipcurve measured at 23.25 GHz with (red circles) and without (black squares) radome

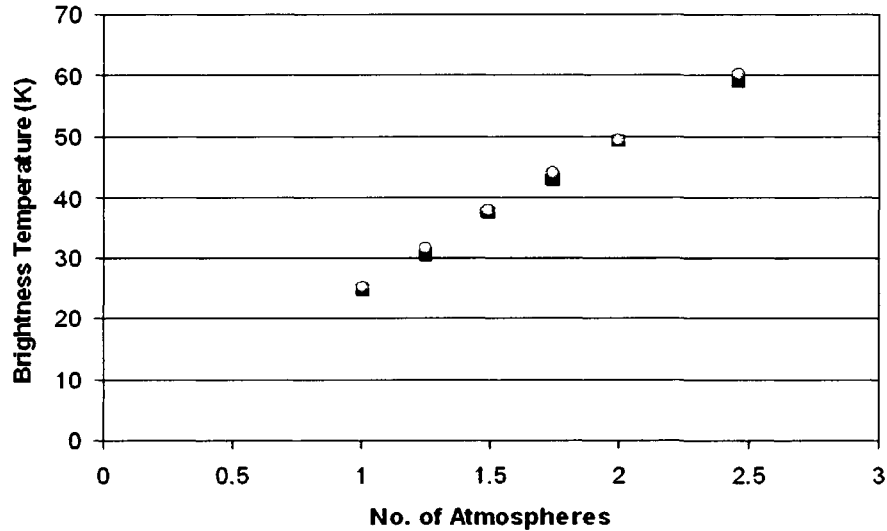


Figure 2.9: Comparison of tipcurve measured at 24.50 GHz with (red circles) and without (black squares) radome

2. The CHA-2069 low noise amplifier was used in CMR-H3 multi-chip-module instead of CHA-2090 used in CMR-H2 and CMR-H1 as shown in figure 2.10. The advantages of the CHA-2069 is that it does not need a gate voltage. The gate is grounded. The drain voltage is software controlled. In LNA's that require a gate voltage, extreme care must be taken that gate is biased before providing the drain voltage. Accidentally, turning on the drain before the gate can damage the LNA. The drain voltage is software controlled and buffered to increase the current providing capacity.

3. An isolator, RADI-22-28-MSS-0.2WR-NM-b, manufactured by Raditek, Inc. is used before the LNA. Figure 2.11 shows a photo of the isolator and figure 2.12 shows the measured insertion loss and the return loss of a single isolator. The 50 ohm used at the port 3 of the isolator is called a Meander load that is used to dissipate power. The isolator is designed to allow a maximum power of 0.2 W. The isolator prevents

source impedance changes from affecting the LNA gain, and prevents reflections from damaging the noise diode. The reflections prevented by the isolator are due mainly to the poor VSWR between the input and output ports of the low noise amplifier (LNA) and the unequal output impedance at the two ports of the SPDT switch. CMR-H1 and CMR-H2 MCMs do not have an isolator. The temperature control of CMR-H1 and CMR-H2 is a very critical part of the operation because changes in temperature can alter the source impedance of the LNA resulting in the reflections to vary and causing error in the measurement.

4. The multi-chip-module was modified to include the RF section as well as the cascade of the four IF amplifiers in one brass housing as shown in figure 2.13. All the gain sensitive components are packaged in the same module so that they can be maintained at the same temperature.

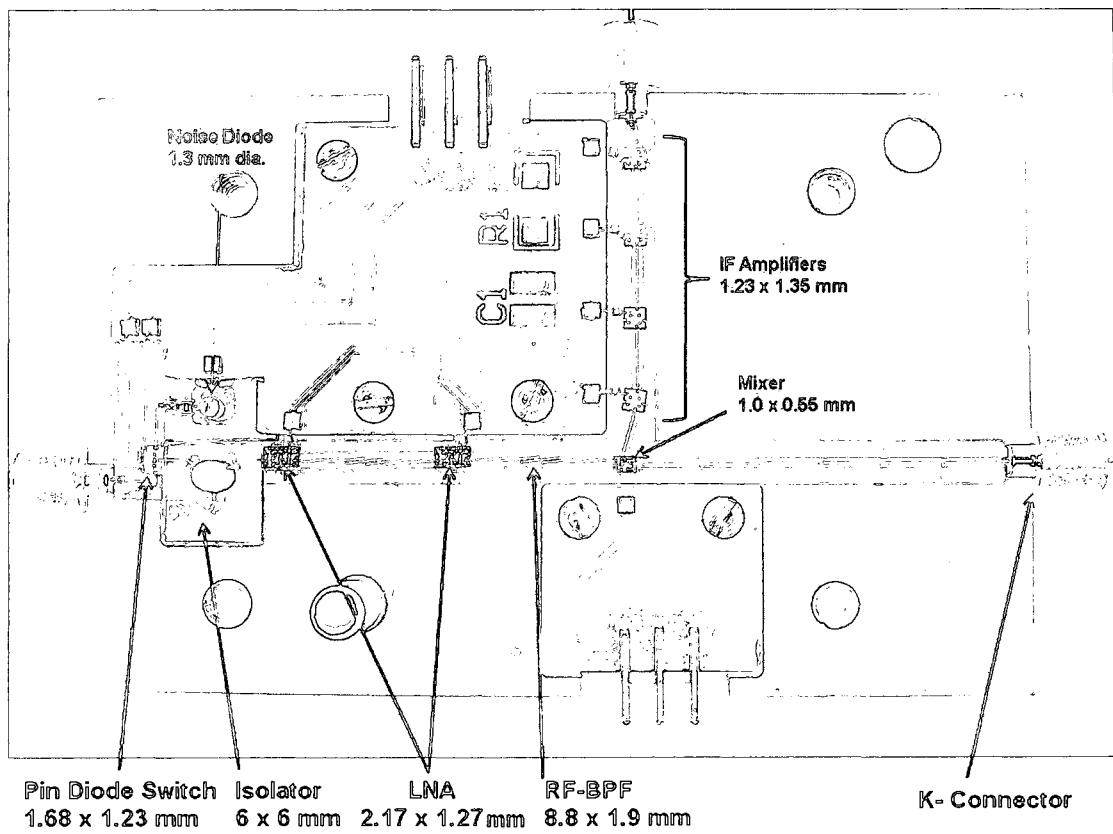


Figure 2.10: Photo of the CMRH3 multi-chip-module

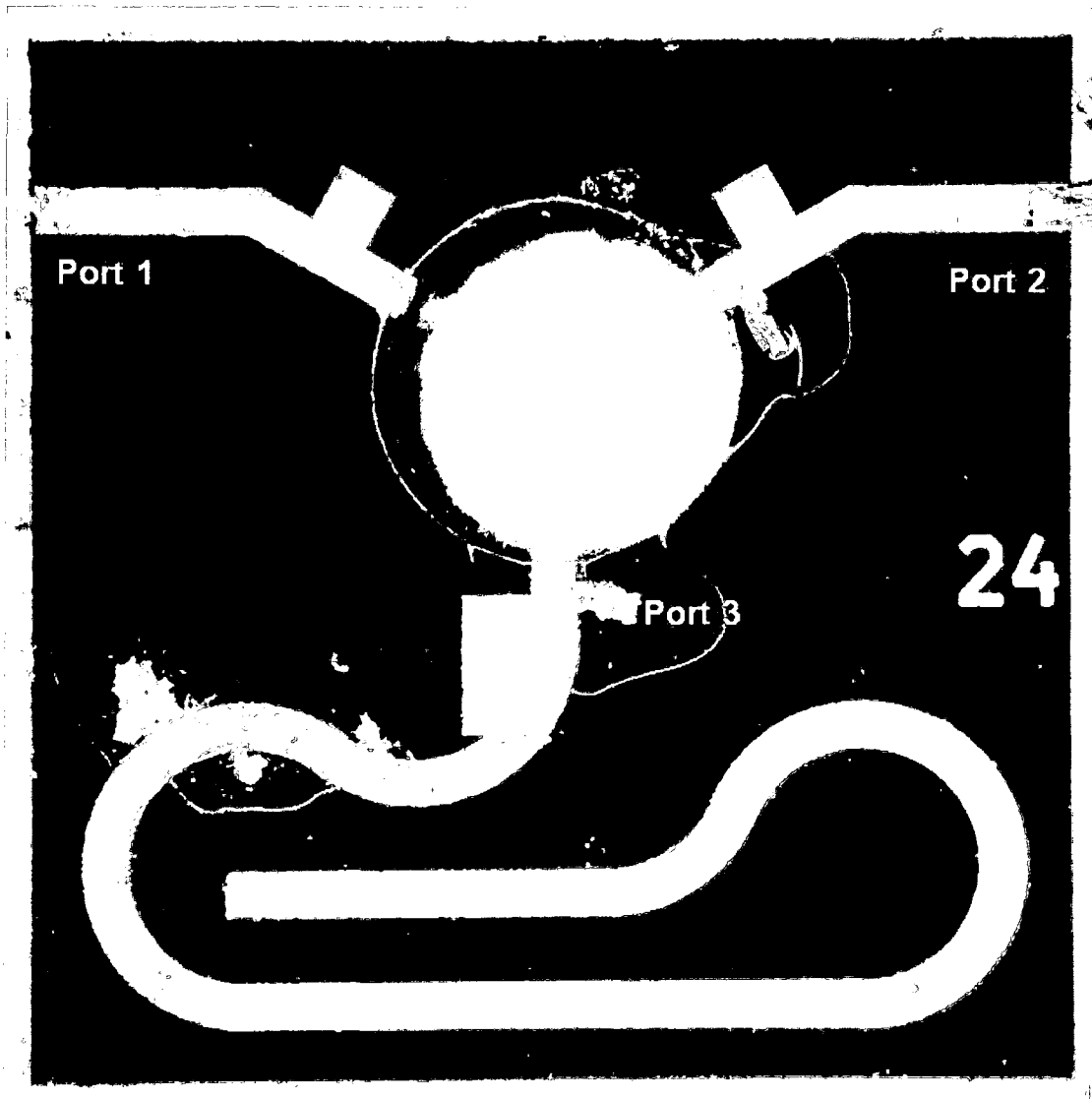


Figure 2.11: Photo of the isolator used in CMR-H3

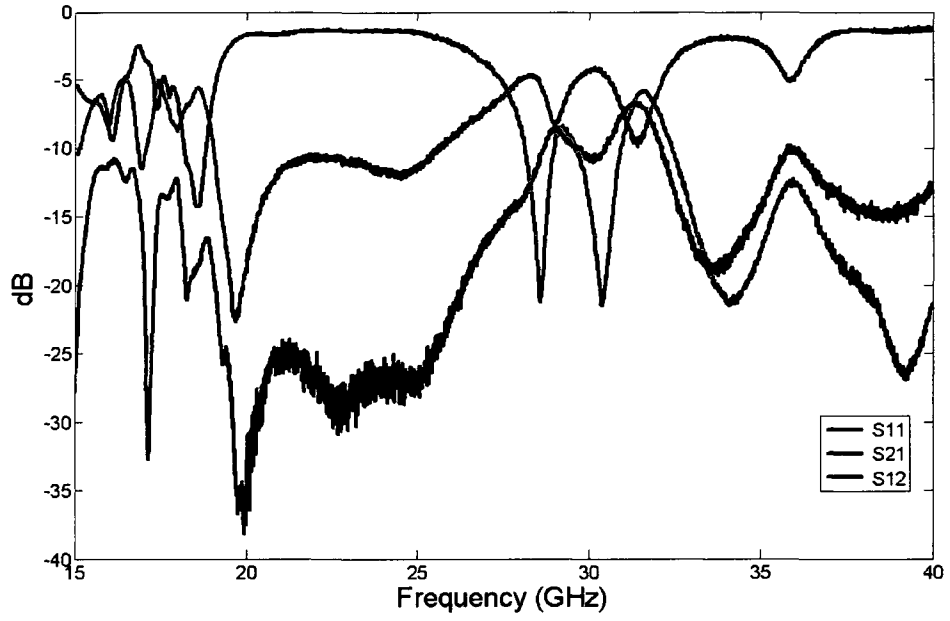


Figure 2.12: S-parameter measurements of the isolator used in CMR-H3

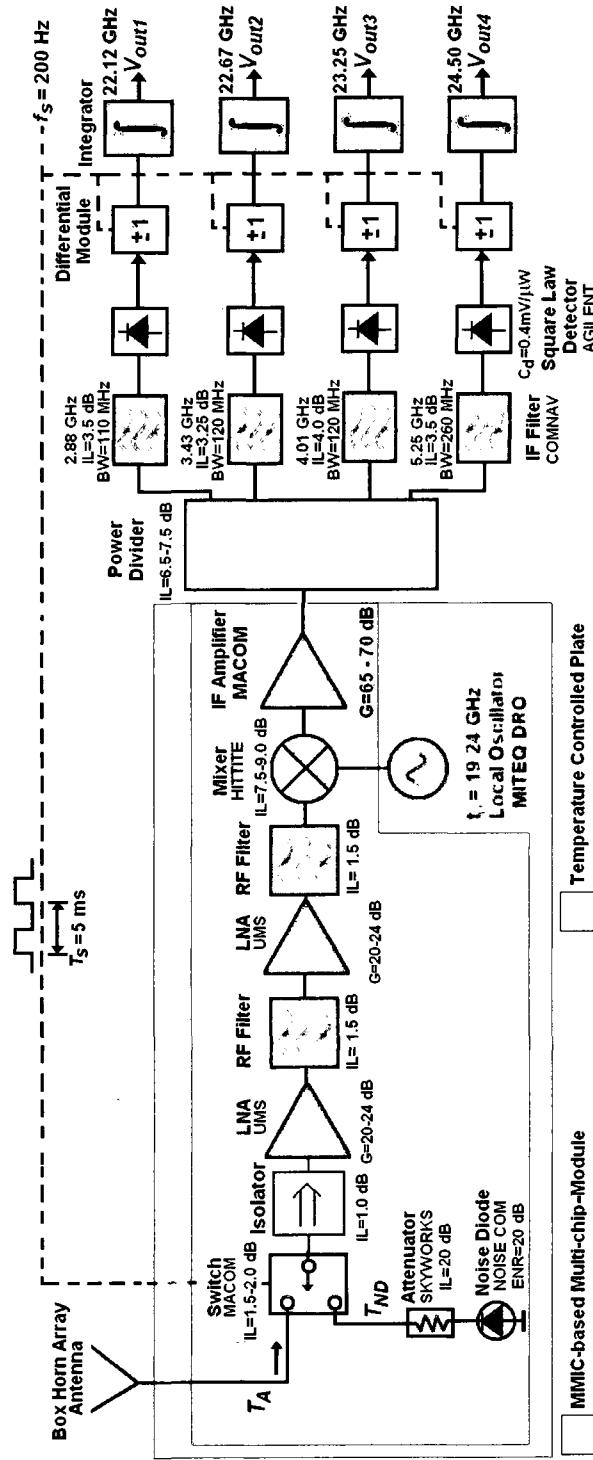


Figure 2.13: Block Diagram of the third Compact Microwave Radiometer for Humidity Profiling (CMR-H3)

2.3 Sensitivity of CMR-H3 Radiometer

A radiometer can be operated as a total power radiometer, a Dicke radiometer or a noise injection radiometer. A total power radiometer provides the best theoretical radiometric resolution among the three radiometer topologies; the theoretical resolution of Dicke-switching and noise injection radiometers is degraded by approximately a factor of two. In practice, a total power radiometer requires frequent calibrations to suppress the offset and gain variations of the receiver. The Dicke topology, on the other hand, cancels the receiver noise variations and greatly reduces gain fluctuations; therefore the calibration interval can be considerably longer. Although the fluctuations of the system gain are reduced using the Dicke switching topology, they are not completely eliminated. Since many RF components exhibit significant gain/loss variations with temperature, effective temperature stabilization was one of CMR-H's design goals to minimize $\Delta G/G$.

Radiometer sensitivity is typically expressed as a “noise-equivalent ΔT ” (NEDT). For a total power radiometer, the NEDT is given by

$$\Delta T = (T_A + T_N) \cdot \sqrt{\frac{1}{B\tau} + \left(\frac{\Delta G}{G}\right)^2} \quad (2.14)$$

where T_N is the receiver's equivalent noise temperature and $\Delta G/G$ is the functional gain fluctuation, which can be caused by gain and loss variations in active and passive devices, respectively. The effects of these fluctuations can be mitigated by performing calibrations at a faster rate. On the other hand, the sensitivity of a Dicke radiometer can be expressed as

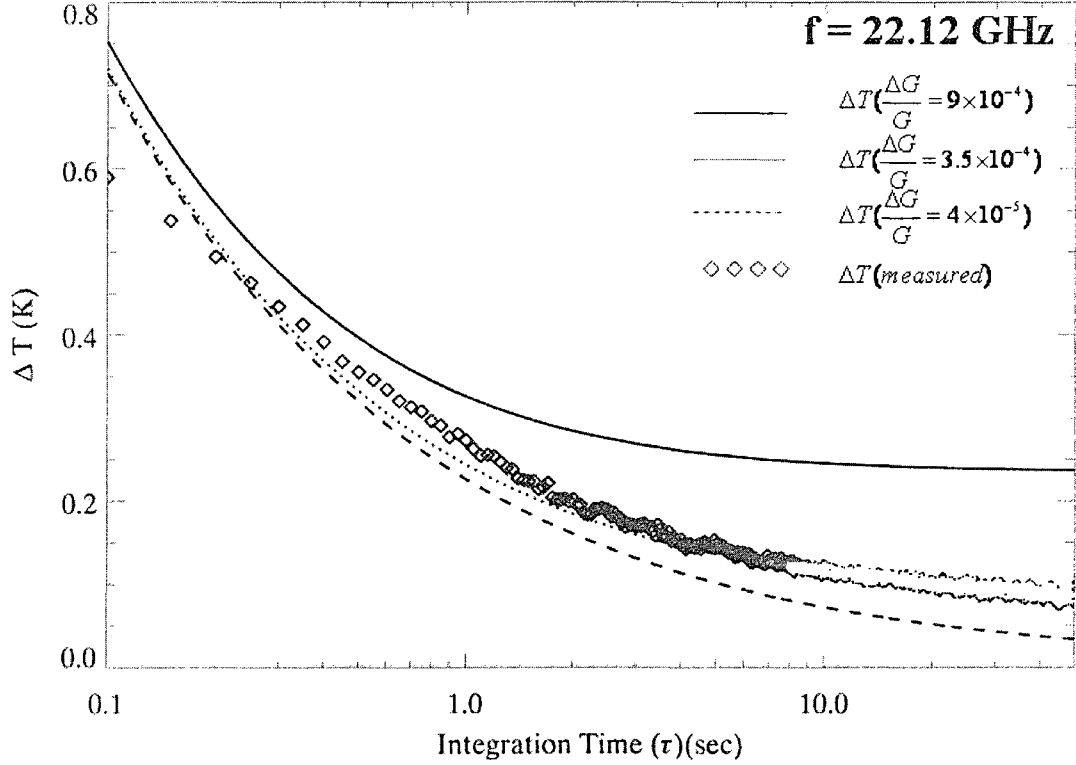


Figure 2.14: Sensitivity of CMR-H at 22.12 GHz

$$\Delta T_{DICKER} = \left[\frac{2(T_A + T_N)^2 + 2(T_{REF} + T_N)^2}{B\tau} + \left(\frac{\Delta G}{G} \right)^2 (T_A - T_{REF})^2 \right]^{\frac{1}{2}} \quad (2.15)$$

where T_A is assumed to be 30 K, B is 120 MHz (the 3 dB bandwidth of the IF filters except for 5.25 GHz, the 3 dB bandwidth is 200 MHz), and T_{ref} is the internal physical temperature, which is typically set near 27°C (300 K).

Figures 2.14, 2.15, 2.16 and 2.17 show the noise equivalent ΔT of the CMR-H3 at 22.12, 22.67, 23.25 and 24.50 GHz, respectively. The measured NEDT compares with the calculated value for a $\Delta G/G$ equal to $\sim 4 \times 10^{-4}$. The NEDT was calculated

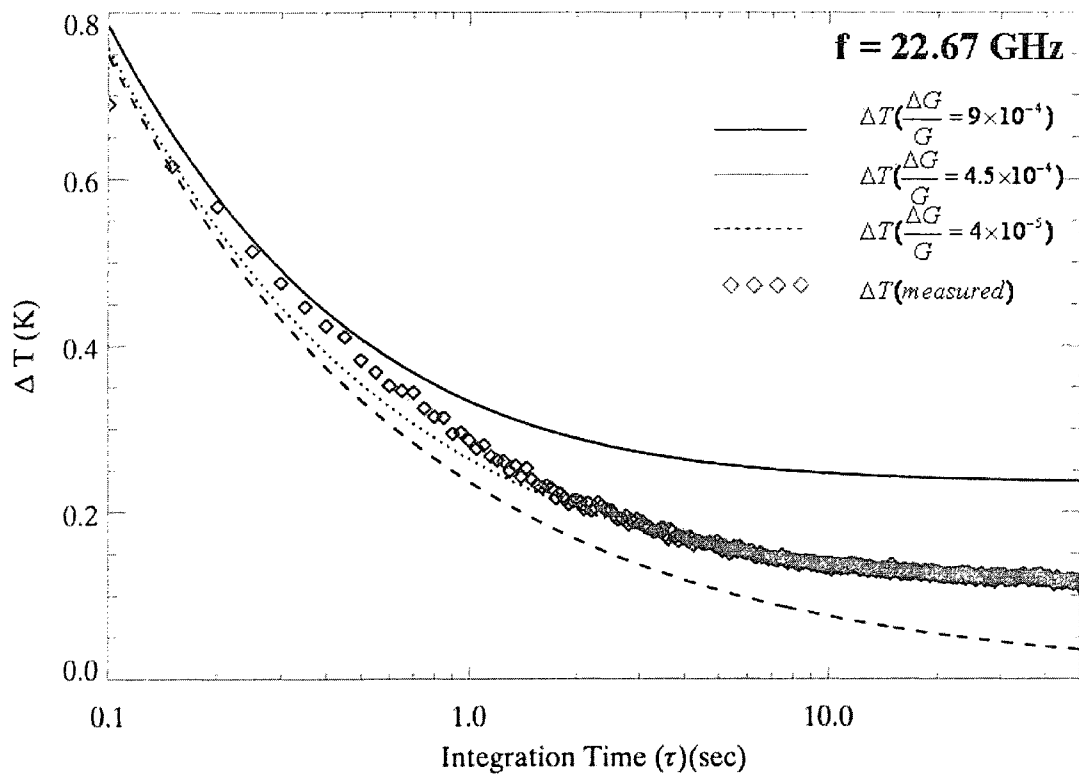


Figure 2.15: Sensitivity of CMR-H at 22.67 GHz

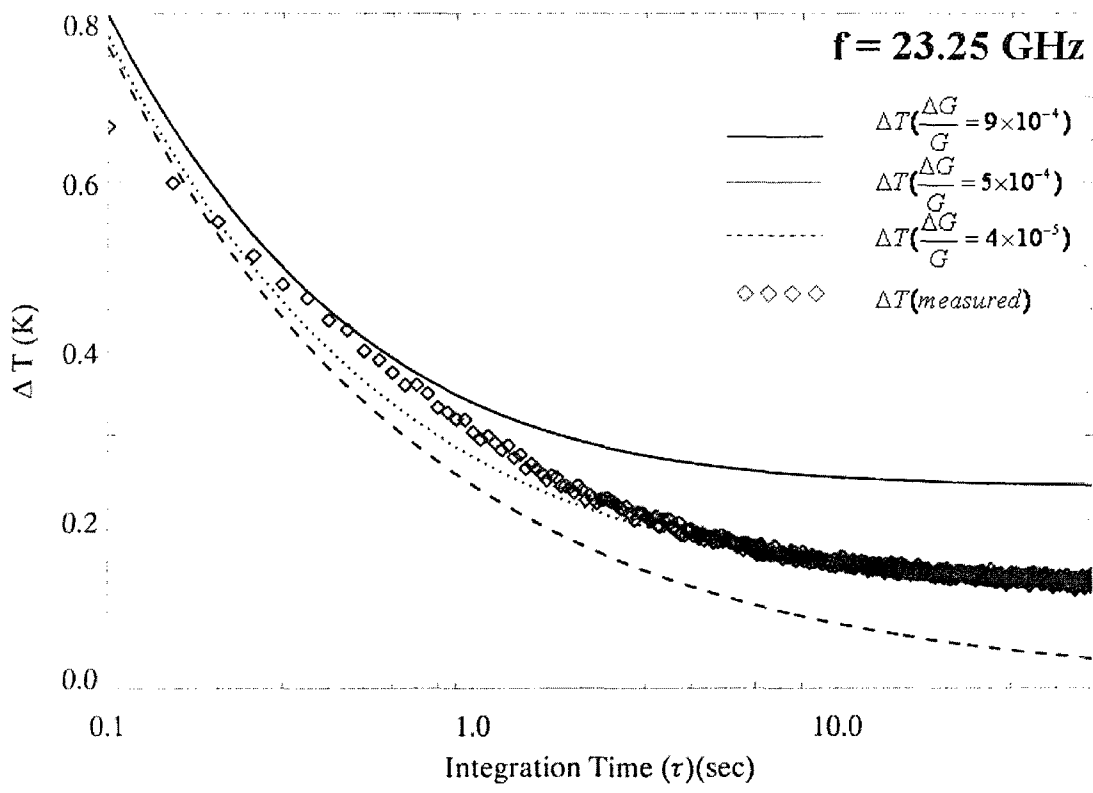


Figure 2.16: Sensitivity of CMR-H at 23.25 GHz

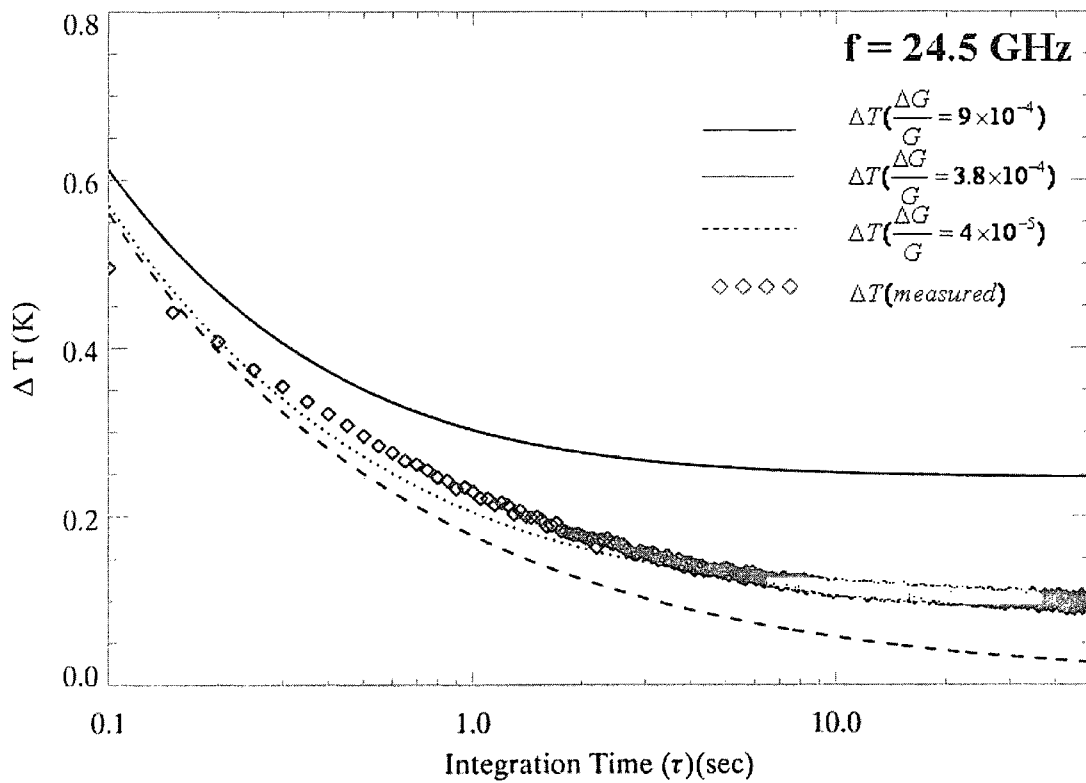


Figure 2.17: Sensitivity of CMR-H at 24.50 GHz

using a long time series of brightness temperature measured in a zenith pointing configuration. The mean values of the brightness temperature are 35, 33.5, 29 and 23 K at 22.12, 22.67, 23.25 and 24.50 GHz.

Chapter 3

3-D Water Vapor Retrieval Using Tomographic Inversion

This Chapter describes the 3-D retrieval of water vapor density using brightness temperatures measured by a scanning network of compact microwave radiometers. To begin with, we describe the 1-D water vapor retrieval technique which is extended to a 3-D retrieval technique. The 3-D water vapor retrieval makes use of the radiative transfer theory, algebraic tomographic reconstruction and the Bayesian optimal estimation coupled with Kalman filtering. Finally, the use of spatial interpolation (kriging) to retrieve the water vapor in unsampled location is demonstrated. Spatial interpolation uses the spatial correlation statistics of water vapor obtained by the analysis of the numerical weather prediction model output.

3.1 Inversion of Single-Radiometer Brightness Temperatures

The CMR-H successfully performed several zenith pointing measurements during March and August, 2006 as well as October, 2007. Vaisala RS-92 radiosondes were launched, using the Digicora III sonde system, at the same location as the CMR-H for measurement comparison. The relative humidity (RH) accuracy of RS-92 radiosondes is approximately 5% in the lower troposphere and 10% in the middle and upper troposphere [32]. The 1-D water vapor retrieval method is discussed before we describe the 3-D technique.

Retrieval of the water vapor profile from the measured brightness temperatures is performed as follows. A forward model provides a mapping between a measurement space, in this case the brightness temperatures measured by the radiometer, into a state space, here the tropospheric water vapor density. For this process, the forward model is generated from the radiative transfer equation, which can be expressed as

$$T_B(f) = \int_a^b W(f, z)g(z), dz \quad (3.1)$$

In the case of atmospheric brightness temperature measurements from the ground, the integral limits are $a = 0$ and $b = H$, corresponding to the surface and top of the atmosphere, respectively. The weighting function $W(f, z)$ expresses the fractional contribution of the atmospheric emission at altitude z to the brightness temperature at the frequency f . The function $g(z)$ is the distribution function of an atmospheric parameter. In this case, $g(z) = \rho_v(z)$, the water vapor density as a function of altitude.

Modeling the atmosphere as a set of layers with uniform thickness Δz , and expressing 3.1 in discrete form, microwave emission from the altitudes between z and $z + \Delta z$ contributes $W(f, z)g(z)\Delta z$ to the brightness temperature T_B at the frequency f . As a consequence, the total measured brightness temperature at this radiometer frequency will be given by 3.1. A weighting function for a specific atmospheric parameter represents the change in the measured brightness temperature due to a unit change in that parameter as a function of altitude. The weighting functions are specific to the radiometer channel frequency f as shown in 3.1. The weighting function for the water vapor density $\rho_v(z)$ at height z at a given frequency f is defined as [33]:

$$W(f, z) = \lim_{\delta\rho_v, \delta z \rightarrow 0} \frac{\delta T_B}{\delta\rho_v(z)\delta(z)} \quad (3.2)$$

From 3.2, the weighting function for the water vapor is derived as [34]

$$W_{\rho_v}(f, z) = \frac{\delta\kappa_a(z)}{\delta\rho_v(z)} [T(z) - T'_B(f, z)] e^{-\tau(0, z, f)} \quad (3.3)$$

where $\kappa_a(z)$ is the water vapor absorption coefficient at altitude z , $\rho_v(z)$ is the water vapor density at altitude z , T'_B is the brightness temperature corrected to account for the effect of non-zero antenna beamwidth, and $T(z)$ is the air temperature at altitude z . The brightness temperature $T_B(\theta, \phi)$ measured by a radiometer at a specified frequency elevation angle θ and azimuth angle ϕ is a weighted average of incoming background temperatures $T_B(\eta, \xi)$ over all directions η, ξ is given as [35]

$$T_B(\theta, \phi) = \frac{\int_0^{2\pi} \int_0^\pi P(\theta, \phi; \eta, \xi) T_b(\eta, \xi) \sin(\eta) d\eta d\xi}{\int_0^{2\pi} \int_0^\pi P(\theta, \phi; \eta, \xi) \sin(\eta) d\eta d\xi} \quad (3.4)$$

$P(\theta, \phi; \eta, \xi)$ is the power pattern of the radiometer antenna. $T_B(\theta, \phi)$, the bright-

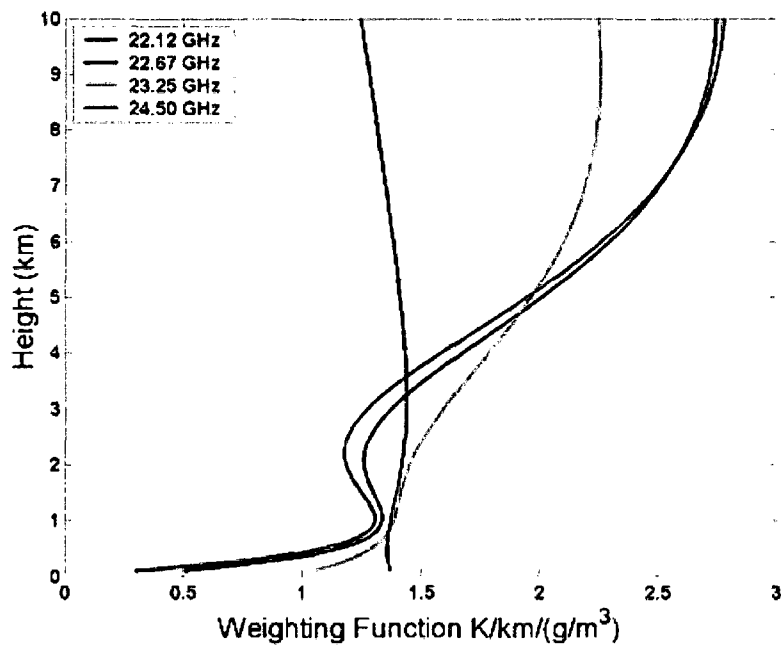


Figure 3.1: Weighting function at the four CMR-H frequencies

ness temperature measured by the radiometer, exceeds the brightness temperature T_B^c that would be measured by an infinitesimally narrow-beam antenna aimed at the boresight direction of the radiometer antenna. The difference $T_B(\theta, \phi) - T_B^c$ is a function of the antenna beamwidth, as well as the amount and distribution of atmospheric water vapor. Assuming the radiometer antenna pattern to be Gaussian, this difference δT_B is

$$\delta T_B(\theta) = \frac{\theta_{1/2}^2}{16 \ln 2} (T_{mr}(\theta) - T_{CMB}) e^{(-\tau(\theta))} [2 + (2 - \tau(\theta)) \tan^{-2}(\theta)] \tau(\theta) \quad (3.5)$$

where $\theta_{1/2}$ is the half-power (3 dB) beamwidth in radians, T_{CMB} is the cosmic microwave background radiation (a constant 2.73 K and T_{mr} is the mean radiating temperature, expressed as

$$T_{mr}(\theta) = \frac{\int_0^H \kappa(z) T(z) (1 - \int_0^{z-z'} \kappa(z') dz')}{1 - e^{-\int_0^H \kappa(z) dz}} \quad (3.6)$$

and $\tau(\theta)$ is the slant path opacity at elevation angle θ as

$$\tau(\theta) = \int_0^H \kappa(z) dz \quad (3.7)$$

After removing the contribution due to non-zero beamwidth, the corrected brightness temperature T_B' is

$$T_B' = T_B - \delta T_B \quad (3.8)$$

For a zenith-pointing measurement, the discrete form of the weighting function W is an $m \times n$ matrix, where m is the number of measured frequency channels and n

is the number of altitudes at which the water vapor density is to be retrieved. Since the inversion of the measurements to retrieve geophysical quantities requires finding the inverse of W , the solution is under-constrained if the number of measurements available (m) is smaller than the number of spatial samples (n) of the quantity to be retrieved, which is nearly always the case for microwave radiometry. This problem can be overcome to a certain extent by restricting the class of admissible solutions to a set of physically realizable solutions. In this regard, the Bayesian Optimal Estimation technique [23, 36] was chosen to retrieve a water vapor density profile using the brightness temperatures measured at the four frequencies of the CMR-H. Bayes' theorem provides a formalism to invert the forward model and calculate an *a posteriori* probability density function (pdf) by updating the prior pdf with a measurement pdf. The water vapor density is retrieved as

$$\rho_v = \rho_{v,a} + S_{\rho_{v,a}} W^T (W S_{\rho_{v,a}} W^T + S_{T_B})^{-1} (T'_B - W \rho_{v,a}) \quad (3.9)$$

where ρ_v is the water vapor density profile, $\rho_{v,a}$ is the *a-priori* profile, in this case the 0 UTC radiosonde observation (RAOB) performed at the DenverStapleton weather station, $S_{\rho_{v,a}}$ is the error covariance matrix of the *a-priori* water vapor profile, S_{T_B} is the error covariance matrix for the measured brightness temperatures, and W is the weighting function matrix. The retrieval is performed by selecting a water vapor profile that minimizes a cost function in the form of [23]

$$J(\rho_v) = [T'_B - W \rho_v]^T S_{T'_B}^{-1} [T'_B - W \rho_v] + [\rho_v - \rho_{v,a}]^T S_{\rho_{v,a}}^{-1} [\rho_v - \rho_{v,a}] \quad (3.10)$$

where the first term in the summation considers the effect of the measurement

error and the second term is related to the effect of the error in the *a-priori* profile. To minimize the cost function numerically the Gauss-Newton method was used to solve for the water vapor density iteratively as

$$\rho_{v_{i+1}} = \rho_{v,a} + S_{\rho_{v,a}} W_i^T (W_i S_{\rho_{v,a}} W_i^T + S_{T_B})^{-1} [T'_B - W_i \rho_{v_i} + W_i (\rho_{v_i} - \rho_{v,a})] \quad (3.11)$$

where $\rho_{v_{i+1}}$ and ρ_{v_i} are the water vapor profiles before and after iteration i , and W_i is the weighting function matrix for iteration i .

The errors in the *a-priori* water vapor density and measured brightness temperatures are modeled as multi-dimensional zero-mean normal distributions with covariance matrices S_{ρ_v} and S_{T_B} , respectively. The covariance of the observation vector T'_B (with dimension m) is an $m \times m$ matrix. The covariance of the *a priori* water vapor density $\rho_{v,a}$ (with dimension n) is an $n \times n$ matrix. The main diagonal of each covariance matrix contains a set of variances of each variable; the off-diagonal elements contain cross-covariances between each pair of variables. In Bayesian optimal estimation, the *a priori* error covariance matrix provides information about the accuracy of the expected solution of the retrieved state vector, in this case water vapor density. The error covariance matrix of the *a priori* water vapor density $S_{\rho_{v,a}}$ was constructed based on a first-order Markov process, as in

$$S_{\rho_v}(i, j) = \sigma_a^2 e^{-|i-j|\frac{\delta z}{h}} \quad (3.12)$$

where the σ_a are the variances of the *a priori* water vapor densities assumed as $1 \text{ gm}/\text{m}^3$, h is the length scale, empirically estimated as 6 km, and δz is the altitude spacing. The main diagonal elements of the error covariance matrix of the measured

brightness temperatures, S_{TB} , describe the uncertainty in the measurements, assumed to be $\sigma_{TB}=0.5K^2$. This value was obtained by calculating the standard deviation of a long time-series (~ 3000 s) of sky brightness temperatures measured by CMR-H. Figure 3.2 shows good agreement between profiles measured by the RS-92 radiosonde and that retrieved from the brightness temperatures measured by both the CMR-H and the WVP-1500.

In the next section, the 1D retrieval method explained in this subsection is extended to a 3-D tomographic inversion technique for retrieval of the 3-D water vapor field from brightness temperatures measured by a three station network of CMR-Hs.

3.2 Algebraic Tomographic Reconstruction to Retrieve the 3-D Water Vapor Field

Retrieval of the 3-D water vapor field from brightness temperature measurements using a network of ground-based radiometers is analytically similar to the fanbeam projection technique commonly used in medical imaging [37]. However, the requirements for performing fanbeam projection with sufficient accuracy are to measure a large number (~ 1000) of projections and to measure projections that are uniformly distributed over 180° or 360° . It is not practical to satisfy both of these requirements using a ground-based network of radiometers. However, problems of this type may be more amenable to the use of algebraic reconstruction tomographic (ART) techniques. The ART approach to tomographic imaging involves setting up algebraic equations to solve for the unknown targets in terms of the measured projection data. This section describes the formulation of the forward model for the measured brightness

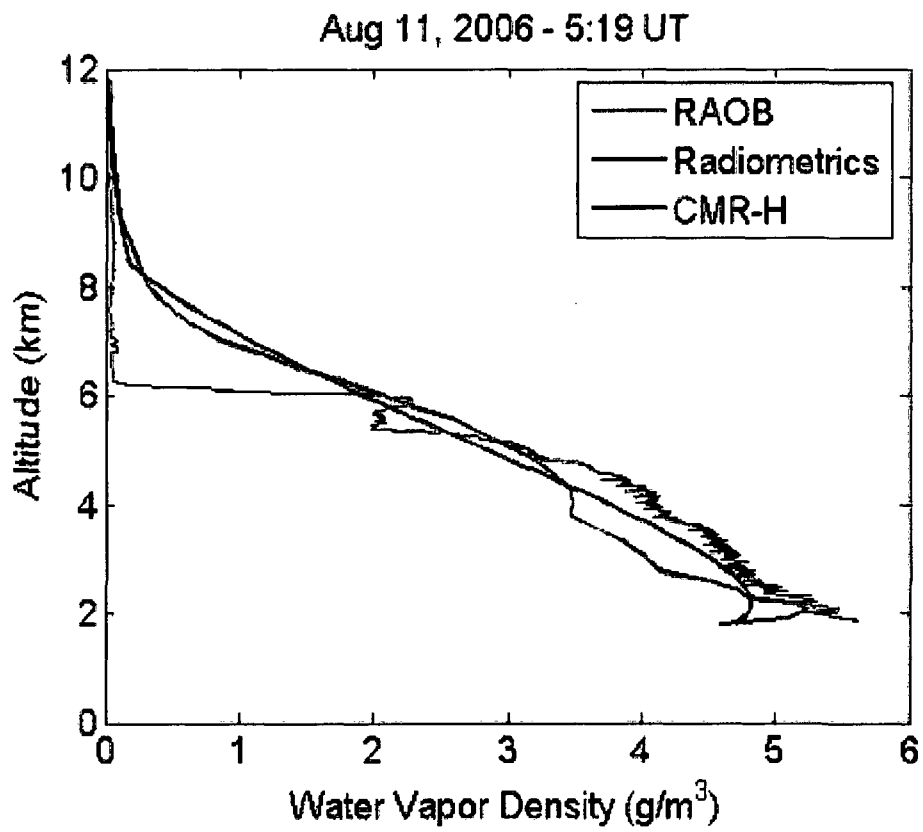


Figure 3.2: Comparison of water vapor density profiles measured by radiosonde with those retrieved from microwave brightness temperatures measured by CMR-H and Radiometrics WVP-1500 radiometers.

temperatures, the inversion of the brightness temperatures to obtain the water vapor absorption coefficients, algebraic reconstruction tomography (ART) of the water vapor absorption coefficients and retrieval of the water vapor using its absorption line shape. Finally, kriging is used to estimate the water vapor at unsampled locations. Kriging, in turn, uses the spatial correlation distances of water vapor density discussed in 3.2.3.

3.2.1 Forward Model

The forward radiative transfer model uses known water vapor densities, either measured or from WRF model outputs to calculate the expected radiometer brightness temperatures [36, 38] as

$$T_B(z) = T_{CMB}e^{-\tau(0,z)} + \int_0^z k_{abs}(z')T(z')e^{-\tau(z',z)} dz' \quad (3.13)$$

where T_B is the brightness temperature in K, z is the height of the tropopause in km, k_{abs} is the absorption coefficient at a particular altitude in Np/km, τ is the optical depth as defined in 3.1 and T_{CMB} is the cosmic microwave background radiation (a constant 2.73 K, since galactic radiation is negligible for our purposes above ~ 3 GHz). If the scanned domain is divided into M grid cells, the forward model in a discrete form can be expressed as

$$T_{Bi} = T_{CMB}e^{\sum_{j=1}^M k_{abs_j} \Delta r_{ij}} + \sum_{j=1}^M k_{abs_j} T_j e^{-\tau_{ij} \Delta r_{ij}} \quad (3.14)$$

where T_{Bi} is the integrated brightness temperature measured by a radiometer pointing in the direction θ_i , the i^{th} elevation angle; k_{abs_j} is the absorption coefficient

in the j^{th} grid cell; T_j is the air temperature in the j^{th} grid cell; Δr_{ij} is the length of ray intersecting with the j^{th} grid cell for the i^{th} elevation angle; and the opacity τ_{ij} is given as

$$\tau_{ij} = \sum_{m=1}^{j-1} k_{abs_j} \Delta r_{im} \quad (3.15)$$

We linearize this forward model by replacing the exponential term in 3.14 with the first two terms of its Taylor series and temporarily ignoring the effect of the cosmic background radiation to obtain

$$T_{Bi} = \sum_{j=1}^M k_{abs_j} T_j \Delta r_{ij} \left(1 - \sum_{l=1}^{j-1} k_{abs_j} \Delta r_{il}\right) \quad (3.16)$$

Having formulated the forward model, a reference profile of the pressure, temperature and water vapor density for a typical atmosphere for the latitude, longitude and season is used to calculate the brightness temperatures expected to be measured by microwave radiometers for a standard reference atmosphere, called T_{Brefi} , for a set of measured elevation angles. Figure 3.3(a) shows the scanning angles for two CMR-H's placed 10 km apart and 3.3(b) shows the overlapping pixels between the two radiometers. For example, the mid-latitude summer reference atmospheric profile is used for the OSSE described in Chapter 4. The absorption coefficient in each grid cell was calculated at the CMR-H frequencies using state-of-the-art absorption models [39, 40]. Defining variations in the absorption coefficients in each grid cell from their reference values as

$$\Delta K = K_{abs} - K_{absref} \quad (3.17)$$

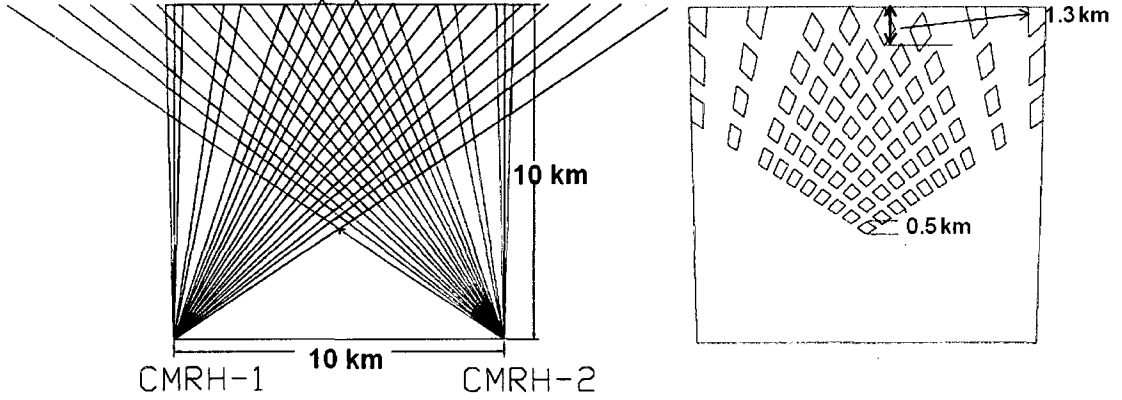


Figure 3.3: (a) Illustration of scanning angles in a 2-D plane and (b) The size of overlapping pixels.

and defining variations in the calculated brightness temperatures at each elevation angle θ_i from their reference values as

$$\Delta T_B = T_B - T_{Bref} \quad (3.18)$$

In addition, the differencing operation in obtaining ΔT_B cancels any effect of the non-zero antenna beamwidth and sidelobes. These two vectors are then related by a Jacobian matrix G as

$$\Delta T_B = G \cdot \Delta K \quad (3.19)$$

Therefore, the elements of the Jacobian matrix G are g_{ij} , the partial derivatives of the change in the brightness temperature at the i^{th} elevation angle with respect to the change in absorption coefficient in the j^{th} grid cell, as

$$g_{ij} = \frac{\partial(\Delta T_{Bi})}{\partial(\Delta k_j)} \quad (3.20)$$

The variations in the retrieved absorption coefficients, ΔK , as a function of measured variations in brightness temperatures, ΔT_B , are determined as

$$\Delta K = G^{-1} \Delta T_B \quad (3.21)$$

In the next section, we will describe the method used to calculate the inverse of the Jacobian matrix to compute the absorption coefficients from the brightness temperature measurements.

3.2.2 Inversion: Optimal Estimation and Kalman Filtering

Solving by computing the inverse G is an ill-posed problem, so no unique solution for ΔK exists. Regularization techniques are needed to solve such ill-posed problems. Singular Value Decomposition (SVD) was the first method tried to solve the inverse problem. Using SVD, we can write the inverse equation as

$$\Delta T_B = U \cdot \Lambda \cdot V' \cdot \Delta K \quad (3.22)$$

where U is the eigenvector of brightness temperature vector with dimension P , V is the eigenvector of the absorption coefficient vector with dimension P and Λ is the diagonal eigenvalues matrix and p is the number of non-null eigenvalues. SVD analysis decomposes a $M \times N$ matrix when U is an $M \times M$ matrix, V is an $N \times N$ matrix and Λ is a diagonal matrix with $p = \min(M, N)$ non-null eigenvalues which are the diagonal elements of the matrix. Least squares inversion simplifies to

$$\Delta K = \sum_{i=1}^p \frac{u_i \cdot \Delta T}{\lambda_i} \quad (3.23)$$

SVD analysis results in a limited number of eigenvalues for the set of scanning angle measurements performed by the radiometer network. The number of non-zero eigenvalues of G was calculated to find a set of elevation angles with minimum redundancy. The number of eigenvalues is equal to the number of independent ray intersections with unique grid cells. Figure 3.4 shows the number of eigenvalues as a function of the number of elevation angles measured by a scanning radiometer. In a physical sense, the number of rays intersecting a bin in the grid directly influences the number of non-null eigenvalues obtained from the singular value decomposition of the Jacobian matrix. There can be two undesirable situations with the rays intersecting a bin i.e. it can either have poor ray coverage or can be intersected by a number of rays that give rise to linearly dependent equations which are not useful to retrieve the model space variable of that particular bin. A meaningful retrieval corresponds to a truncated reconstruction grid size with coarse spatial resolution on the order of 2-4 km.

The Bayesian optimal estimation is a constrained inversion technique that uses an *a-priori* profile to obtain a fine resolution retrieval of the 3-D water vapor field. Using this technique, ΔK is retrieved as

$$\Delta K = \Delta K_{apriori} + S_{\Delta K_{apriori}}^{-1} G^T (G S_{\Delta K_{apriori}} G^T + S_{\Delta T_B})^{-1} [\Delta T_B - G \Delta K_{apriori}] \quad (3.24)$$

where $S_{\Delta K_{apriori}}$ is the error covariance matrix of the *a priori* absorption coefficients and $S_{\Delta T_{B_i}}$ is the error covariance matrix of the measured brightness temperatures. Given ΔT_{B_i} , with error statistics, $S_{\Delta T_{B_i}}$ and *a priori* geophysical state vector, $\Delta K_{apriori}$, with covariance matrix, $S_{\Delta K_{apriori}}$, and a forward model to calculate the

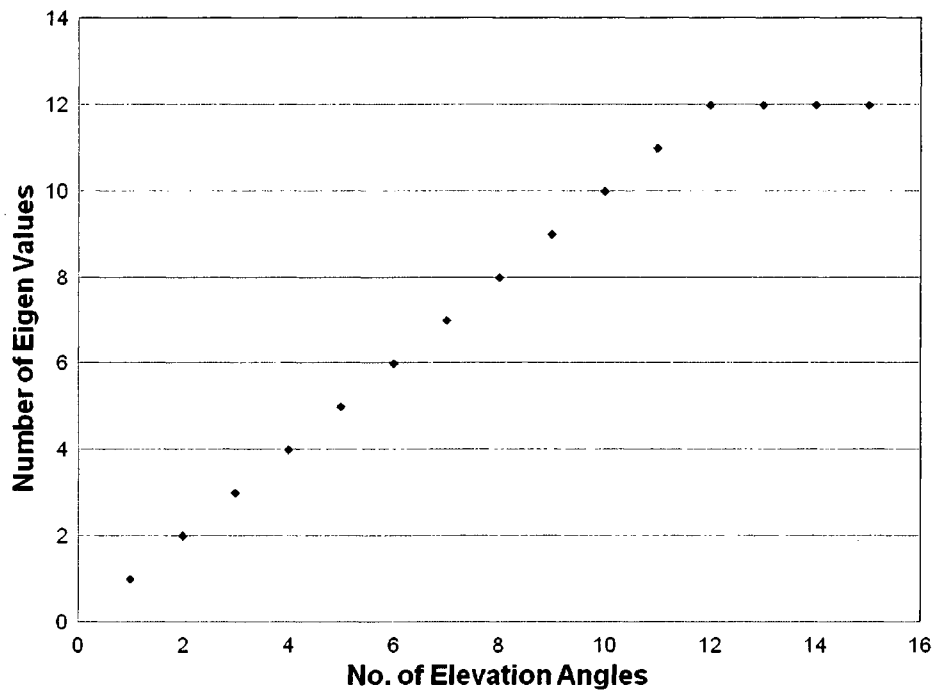


Figure 3.4: The number of eigenvalues of the Jacobian matrix vs. the number of elevation angles.

measured ΔT_{B_i} in terms of the state vector, the change in the absorption coefficients, ΔK , is retrieved by minimizing the cost function (modifying 3.10 for the 3-D retrieval[23])

$$J(\Delta K) = [T_B - G\Delta K_{apriori}]S_{T_B}^{-1}[T_B - G\Delta K_{apriori}] + [\Delta K - \Delta K_{apriori}]S_{\Delta K}^{-1}[\Delta K - \Delta K_{apriori}] \quad (3.25)$$

The Kalman filter technique is used to estimate the water vapor density in each grid cell by performing retrievals in time sequence and ensuring that the retrieved water vapor densities vary smoothly as a function of time. For this method, the previous measurement provides prior information about the water vapor density at the current time. The sequential evolution of the *a priori* measurement is modeled by using a Kalman filter model evolution parameter M_t , given as

$$\Delta K_{apriori}(t) = M_t(\Delta K_{apriori}(t-1)) \quad (3.26)$$

$$M_t = \frac{\delta M_t \Delta K_{apriori}(t-1)}{\delta \Delta K_{apriori}(t)} \quad (3.27)$$

M_t operates sequentially in t . At time $t-1$ an estimate of $\Delta K_{apriori}(t-1)$ has been made, with an error covariance $S_{\Delta K_{apriori}(t-1)}$. The stochastic prediction equation 3.26 is used to construct a prior estimate $\Delta K_{apriori}(t)$ and its covariance $S_{\Delta K_{apriori}(t)}$ at time t . This is combined with the optimal estimation equations ?? to provide an updated estimate of the water vapor density. The Jacobian G has elements as shown in 3.20. The retrieved absorption coefficients in each WRF model grid cell (0.5 km x 0.5 km typical horizontal resolution) at the four operating frequencies of CMR-H

are then used to compute the water vapor density in the grid cell by performing a non-linear curve fit to the Van-Vleck Weisskopf (VVW) absorption line shape [35], given as

$$\begin{aligned}
k_{abs-j}(f) = & (0.3633 \times 10^3) f^2 \rho_{v-j} \left(\frac{300}{T_j}\right)^{3/2} \gamma \\
& \left[\left(\frac{1}{T_j}\right) \left(\frac{1}{300}\right)^{3/2} e^{-\frac{644}{T_j}} \left[\frac{1}{(22.235 - f^2) + \gamma^2}\right.\right. \\
& \left.\left. + \frac{1}{(22.235 + f^2) + \gamma^2}\right] + 6.6061 \times 10^{-9}\right]
\end{aligned} \tag{3.28}$$

where the linewidth parameter γ in GHz is

$$\gamma = 2.85 \left(\frac{P_j}{1013}\right) \left(\frac{300}{T_j}\right)^0.626 [1 + 0.018 \frac{\rho_{v-j} T_j}{P_j}] \tag{3.29}$$

P_j is the pressure, T_j is the temperature and ρ_{v-j} is the water vapor density in the j^{th} grid cell. A non-linear polynomial curve fit was implemented to calculate the water vapor density ρ_{v-j} in each grid cell. The WRF model outputs for pressure and temperature in each grid cell were used in the VVW equation to obtain the curve fits. The water vapor densities in unsampled locations were estimated using spatial interpolation techniques. In the next section, we will explain the technique of kriging used to spatially interpolate the water vapor densities in the unsampled pixels.

3.2.3 Kriging

Kriging [41, 42] provides a solution to the problem of estimation at unsampled pixels based on a continuous model of stochastic spatial variation. The water vapor densities in these pixels are calculated using

$$\rho(x_0) = \sum_{j=1}^N \lambda_j \rho(x_j) \quad (3.30)$$

where $\rho(x_0)$ is the water vapor density at x_0 and $\rho(x_i)$ are the water vapor densities at locations $i=1$ to N and the weights λ_i are given as

$$\sum_{j=1}^N \lambda_j = 1 \quad (3.31)$$

λ_i is calculated as

$$\sum_{j=1}^N \lambda_j \Gamma(x_i, x_j) + \psi(x_0) = \Gamma(x_j, x_0) \quad (3.32)$$

where $\Gamma(x_i, x_j)$ is variogram between x_i and x_j , $\psi(x_0)$ is the Lagrange multiplier and $\Gamma(x_i, x_0)$ is the variogram between x_i and x_0 . The Lagrange multiplier was estimated such that it minimizes the mean square error of the variance of the estimated value.

In summary, the retrieval process consists of using the brightness temperatures measured by the three radiometers to retrieve the water vapor densities in each observed grid cell. These water vapor densities are then used along with correlation distances of water vapor for each altitude to calculate water vapor densities at unsampled locations to yield the 3-D water vapor field. The next section describes the measurement configuration and the demonstration of the 3-D retrieval technique via an OSSE using outputs from a fine-resolution weather research and forecasting (WRF) numerical weather prediction model.

In the next chapter, we demonstrate the 3-D retrieval technique by performing an OSSE. We use the output of the numerical weather prediction output to calculate the

brightness temperatures that are expected to be measured by the radiometers. The 3-D water vapor field is then retrieved by using the algebraic tomographic reconstruction explained in the section above.

Chapter 4

Observation System Simulation

Experiment (OSSE)

An Observation System Simulation Experiment (OSSE) was performed in order to evaluate the capabilities of a network of scanning microwave radiometers to retrieve the 3-D distribution of water vapor in the troposphere. In addition, the results of this OSSE were used to determine the optimal azimuthal scanning strategy for retrieval of the 3-D structure of water vapor with typical spatial and temporal resolutions required to forecast a convective event. To accomplish this, the 3-D water vapor output from a fine-resolution WRF numerical weather prediction model was compared with retrievals from synthetic brightness temperatures, i.e. those that would have been measured under the same weather conditions by a remote sensor network of three CMR-Hs.

4.1 Weather Research and Forecasting Model

The Weather Research and Forecasting (WRF) model is a numerical weather prediction (NWP) and atmospheric simulation system designed for both research and operational applications. WRF is supported as a common tool for the university/research and operational communities to promote closer ties between them and to address the needs of both. The WRF project has developed a next-generation mesoscale forecast model and assimilation system to advance both the understanding and the prediction of mesoscale precipitation systems. The WRF system, includes the WRF model itself, preprocessors for producing initial and lateral boundary conditions for idealized, real-data, and one-way nested forecasts, postprocessors for analysis and visualization, and a three-dimensional variational data assimilation (3DVAR) program. The development of WRF has been a multi-agency effort to build a next-generation mesoscale forecast model and data assimilation system to advance the understanding and prediction of mesoscale weather and accelerate the transfer of research advances into operations. The WRF effort has been a collaborative one among the National Center for Atmospheric Research's (NCAR) Mesoscale and Microscale Meteorology (MMM) Division, the National Oceanic and Atmospheric Administration's (NOAA) National Centers for Environmental Prediction (NCEP) and Earth System Research Laboratory (ESRL), the Department of Defense's Air Force Weather Agency (AFWA) and Naval Research Laboratory (NRL), the Center for Analysis and Prediction of Storms (CAPS) at the University of Oklahoma, and the Federal Aviation Administration (FAA), with the participation of university scientists. The WRF model is suitable for a broad range of applications on scales ranging from meters to thousands of kilometers. Such applications include research and operational numerical weather prediction

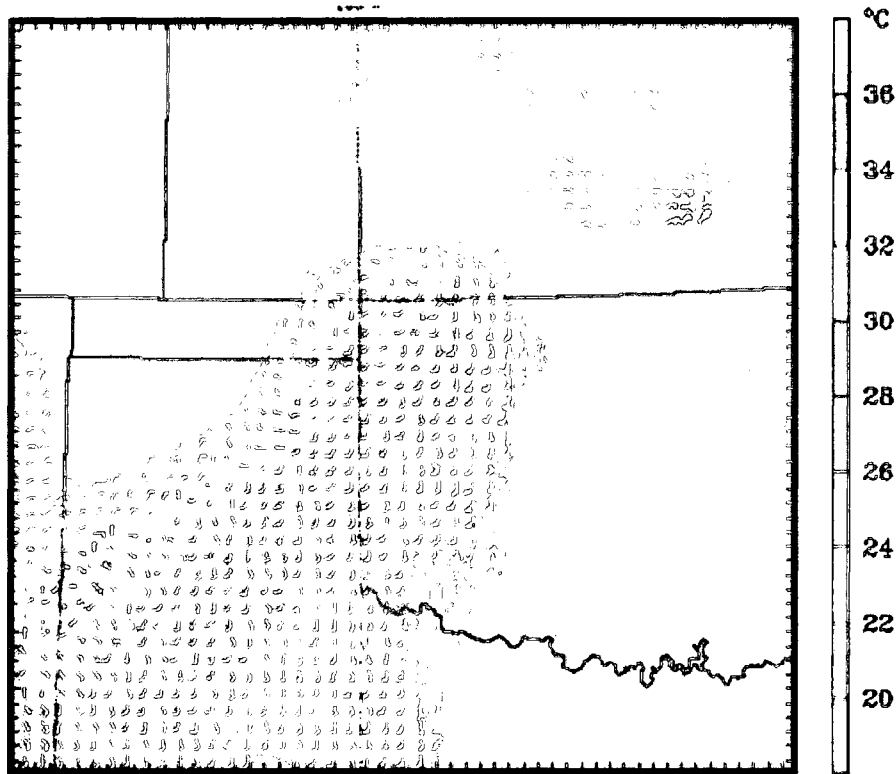


Figure 4.1: WRF model output of temperature

(NWP), data assimilation and parameterized-physics research.

The OSSE was performed using the WRF model output for a cold front and deep convection in Northwest Indiana (40.7° N, 86° W) from 2:00 UTC to 3:00 UTC. For this OSSE, the *a priori* water vapor field was the WRF model output at 2:00 UTC. Assuming the weather conditions of the WRF model output at 3:00 UTC, the forward radiative transfer model described in chapter 3 was used to calculate synthetic brightness temperatures at the CMR-H frequencies as a function of azimuth and elevation angles [36, 38]. Figures 4.1 and 4.2 show model fields of temperature and water vapor mixing ratio at 2:30 UTC. The WRF model output contains 83 variables to describe the various aspects of the atmosphere. The output is generated in a network common

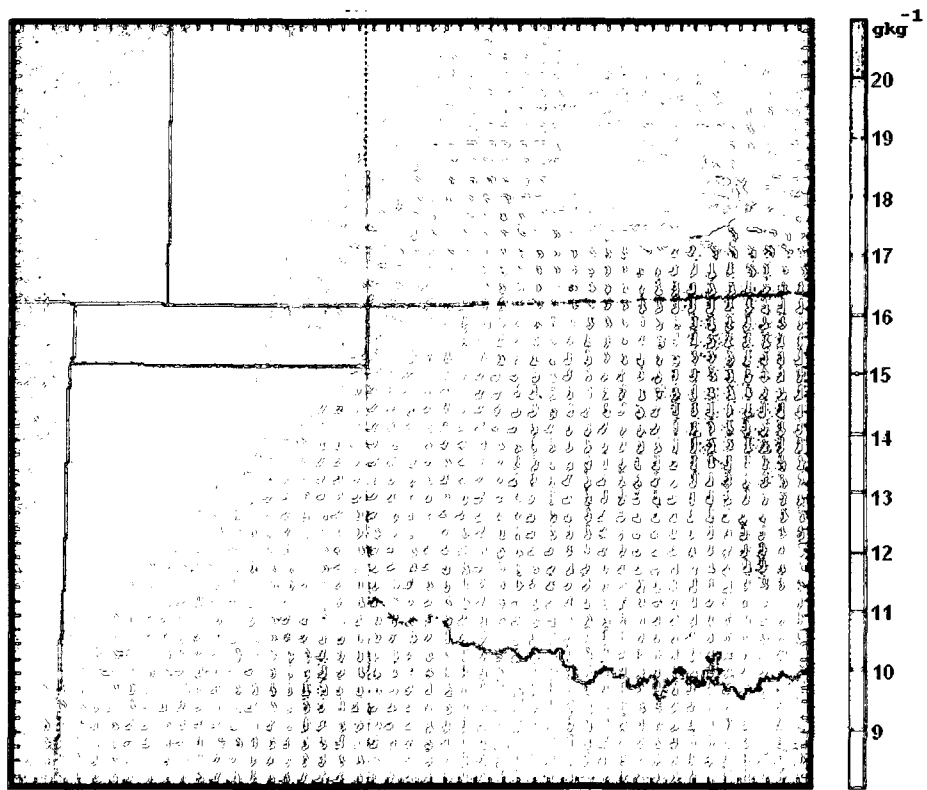


Figure 4.2: WRF model output of water vapor mixing ratio

data format (netcdf). The variables of interest are the perturbation potential(PH) in m^2/s^2 , base state geopotential (PHB) in m^2/s^2 , perturbation potential temperature (T) in K, perturbation pressure (P) in Pa, base state pressure (PB) in Pa, water vapor mixing ratio (QVAPOR) in kg/kg. We use (4.1)-(4.4) to calculate the 3-D fields of pressure, temperature and water vapor densities and the altitude in each grid. The air temperature in K is

$$T_{air} = T\left(\frac{P}{100}\right)^k \quad (4.1)$$

where T is the perturbation potential temperature in K, P is the perturbation pressure in KPa and k is 0.286. The pressure is

$$P_{air} = 0.01(P + P_B) \quad (4.2)$$

where P_B and P are in Pa and P_{air} is in mB. The altitude above ground level is

$$z = \frac{PHB + PH}{g} \quad (4.3)$$

where g is the standard value of acceleration due to gravity between sea level and height z. Finally, the water vapor density is

$$\rho = \frac{QVAPOR \times P}{(QVAPOR + 0.622)(461.5T \times 10^{-5})} \quad (4.4)$$

where P is in mB, QVAPOR is in kg/kg, T in K and ρ is in g/m^3 .

4.2 Spatial Scales of Variation of Water Vapor Densities

Knowledge of the spatial scales of water vapor variability at a variety of altitudes is important to infer the required spatial resolution of water vapor measurements to determine where and when atmospheric conditions are likely to lead to convection based on rapidly evolving moisture gradients. The mesoscale and sub-mesoscale variability of water vapor plays an important role in the understanding of cloud formation and nonlinear processes such as radiative transfer. Measurements using NASA's Millimeter-wave Imaging Radiometer during the TOGA COARE Experiment were used to obtain the mesoscale variations of water vapor. An autocorrelation analysis showed that mid-to-upper tropospheric water vapor content varies on sub-meso γ scales (less than 2-5 km) [25].

The spatial scales of water vapor variability in the troposphere were calculated using outputs of a fine-resolution Weather Research and Forecasting (WRF) model with 500-m resolution. The spatial correlation statistics of geophysical variables are typically analyzed using spatial autocorrelation functions [41, 42]. A geostatistic used to describe the spatial correlation in the data is the semi-variogram, defined as

$$\Gamma = \frac{1}{2m_d} \sum_{j=1}^{m_d} [\rho_v(x_i - y_i) - \rho_v(x_j, y_j)]^2 \quad (4.5)$$

where m_d is the number of pairs of points in the dataset, in this case the WRF model output, at a distance d from each other.

Semi-variograms for water vapor densities were calculated from the WRF model output using 4.5. As shown in Figure 4.3, the semi-variogram increases as the distance

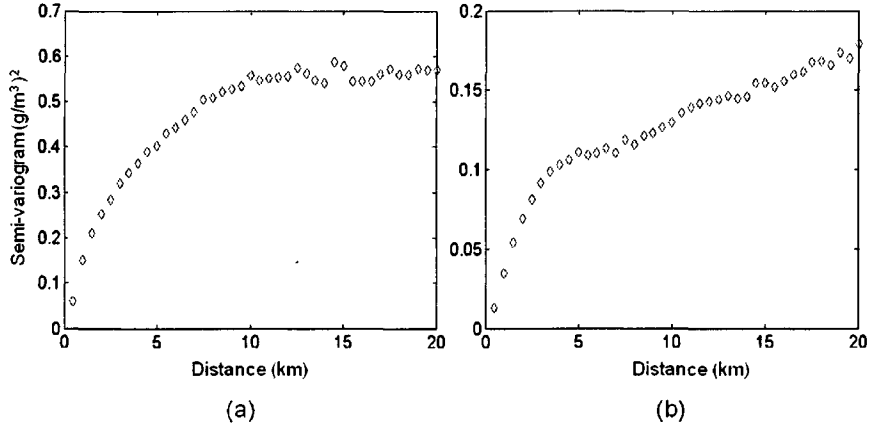


Figure 4.3: Semi-variograms of water vapor density in WRF output at (a) 3 km and (b) 5 km above ground level at 3:00 UTC

d increases from zero. The slope of the semi-variogram is steep and changes until, at a particular distance, it transitions to a minimum, relatively constant value for the remainder of the semi-variogram. The correlation distance is defined as the distance at which this transition occurs. A few functions have been used to find a best fit to the semi-variogram curve [42]. An exponential model 4.6 was fit to the semi-variograms for the WRF model water vapor density outputs at a variety of altitudes to estimate the correlation distances.

$$\Gamma(d) = c_0 + c(1 - e^{-d/a}) \quad (4.6)$$

where c_0 is the variance at zero distance, c is the sill variance when the distance is maximum and a is the correlation length. The semi-variogram plots for 3 km and 5.1 km above ground level (AGL) at 3:00 UTC are shown in figure 4.3. Figure 4.4 shows the correlation distances as a function of time at the two different altitudes. The correlation distances and the variogram values for the WRF model output were

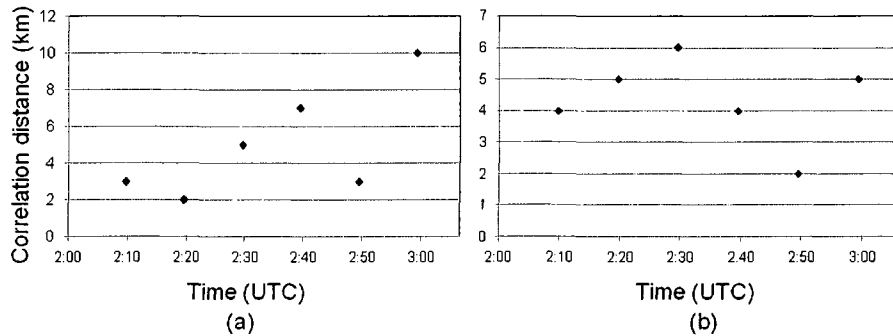


Figure 4.4: Time series of water vapor density correlation distance inferred from the semi-variograms in Figure 4 at (a) 3 km and (b) 5 km above ground level (AGL).

used to calculate the parameters for spatial interpolation as explained in 3.2.3.

Figure 4.4 shows the correlation distances as a function of time at the same two altitudes. The correlation distances and the semi-variogram values for the WRF model output were used to calculate the parameters for spatial interpolation, as described in 3.2.3. 3.2.2 describes tomographic reconstruction of the 3-D water vapor field from brightness temperature measurements performed by multiple radiometers in a remote sensor network.

4.3 OSSE: Three Radiometer Network

4.3.1 Measurement Configuration

To retrieve the 3-D water vapor field with fine spatial and temporal resolution, we propose a coordinated remote sensor network with a Compact Microwave Radiometer for Humidity Profiling (CMR-H) at each network node. Each CMR-H, mounted atop a precise elevation-over-azimuth positioner, is capable of scanning at a rate of $7^\circ/\text{sec}$ in elevation and $25^\circ/\text{sec}$ in azimuth. A network of three CMR-H's in an equilat-

oral triangular configuration with approximately 10 km spacing measures brightness temperatures from which the 3-D water vapor field can be retrieved with a horizontal resolution on sub-meso γ scales of 1-2 km, a vertical resolution of 0.2-0.5 km and a temporal resolution of 10-15 min, assuming each radiometer scans the entire hemisphere above and centered on its location.

The elevation-angle scanning pattern was chosen based on an eigenvalue analysis that excludes any angles resulting in redundant grid cell intersections that provide no additional information on the water vapor density. The result is that each radiometer node will scan at 30° spacing in both azimuth (10 angles over 360°) and elevation, from zenith to 30° above the horizon (6 elevation angles). In the case of the triangular network, each node performs multiple scans of the domain in less than 600 s, the shortest decorrelation time of the atmospheric downwelling emission on the spatial scales of these TB measurements. This decorrelation time is $1/e$ times the maximum autocorrelation of a long (~ 3000 s) time series of brightness temperatures measured during REFRACTT'06 for an unstable atmosphere in the presence of rapidly evolving moisture gradients. It provides a maximum duration during which any given radiometer node must complete a scan of its hemispherical coverage volume. If all radiometer nodes in the network complete their volumetric scans within this time period, measurements from all radiometer nodes can be considered to be simultaneous for the purpose of water vapor retrieval.

Figure 4.5 shows the optimal topology of a network with three CMR-Hs at the vertices of an equilateral triangle with 10-km nearest neighbor spacing. The red segments represent the azimuth angles viewed by each radiometer using the proposed azimuthal scanning pattern, which was determined using the OSSE described in the next subsection. Retrievals at each azimuth angle are combined to obtain the retrieved

3-D water vapor field.

4.3.2 OSSE Results

Figure 4.6(a) shows the WRF model output of the water vapor density at 3.4 km AGL at 3:00 UTC. Taking this WRF model output as “truth”, the percentage error of the retrieved water vapor density at 3:00 UTC is shown in Figure 4.6(b). The OSSE results show that the 3-D water vapor density field can be retrieved with an accuracy of better than 15-20% at all altitudes. A histogram of the retrieval errors is shown in Figure 4.8, demonstrating that the errors in retrieval of water vapor density are roughly uniformly distributed from 5-20%. The OSSE retrieval accuracy can be considered to “worst case” in the sense that the *a priori* field is one or two hours prior to the retrieval; whereas, in a real measurement, one can update the *a priori* estimates every 10 minutes due to availability of brightness temperature measurements. The *a priori* used for this retrieval was the WRF model output at 2:00 UTC. Water vapor densities at the unsampled locations were estimated by using the kriging spatial interpolation technique. The kriging algorithm was based on the spatial characteristics of water vapor densities, including semi-variogram and correlation lengths, calculated using the high-resolution WRF model explained in 3.2.3. Figures 4.7(a) and (b) show the model output of the water vapor densities and those retrieved by the 3-D retrieval technique at 3.4 km, respectively.

4.4 Retrieval Sensitivity

The sensitivity of retrieval to the time of *a priori*, location of the *a priori* and number of radiometers in the network was tested by running the OSSE for a variety of

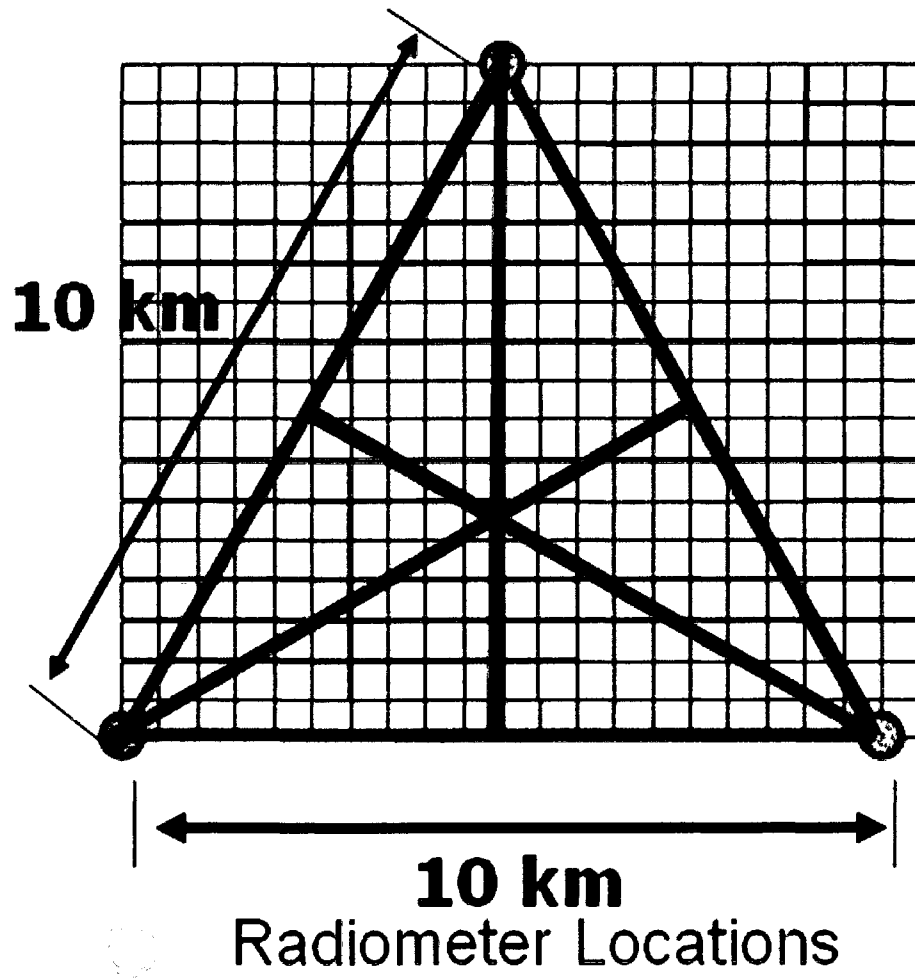


Figure 4.5: Equilateral triangular topology for a three-node scanning radiometer network with a 10-km nearest-neighbor distance.

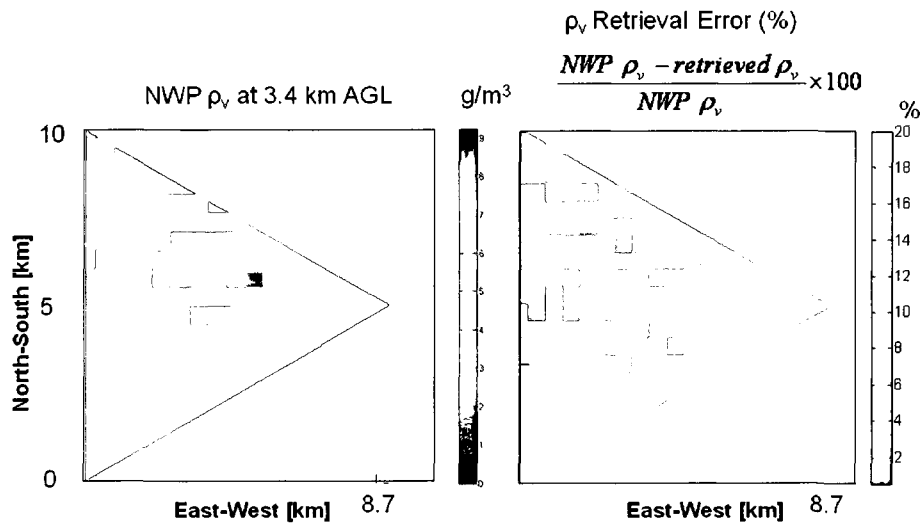


Figure 4.6: (a) WRF model output of the water vapor density at 3.4 km above ground level (AGL) over northwest Indiana at 3:00 UTC. (b) Percentage error of the water vapor density retrieved from synthetic brightness temperature measurements also at 3.4 km AGL with WRF model output at 2:00 UTC used as the *a priori*.

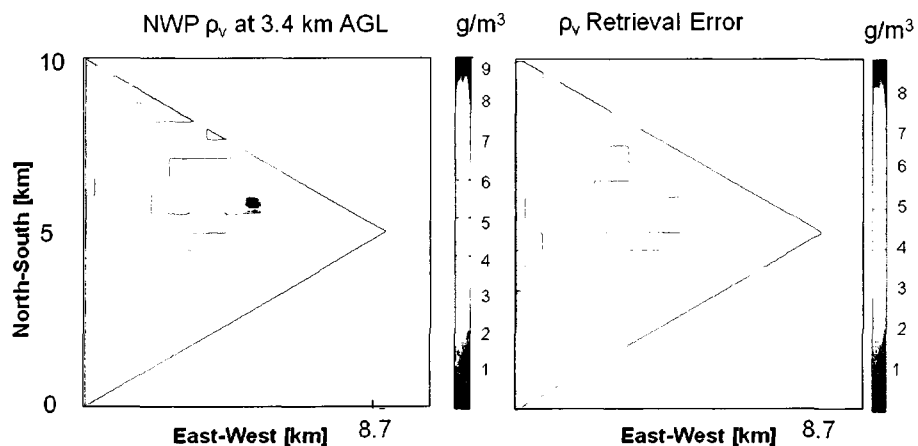


Figure 4.7: (a) WRF model output of the water vapor density at 3.4 km above ground level (AGL) over northwest Indiana at 3:00 UTC. (b) Water vapor density in g/m^3 retrieved from synthetic brightness temperature measurements also at 3.4 km AGL with WRF model output at 2:00 UTC used as the *a priori*.

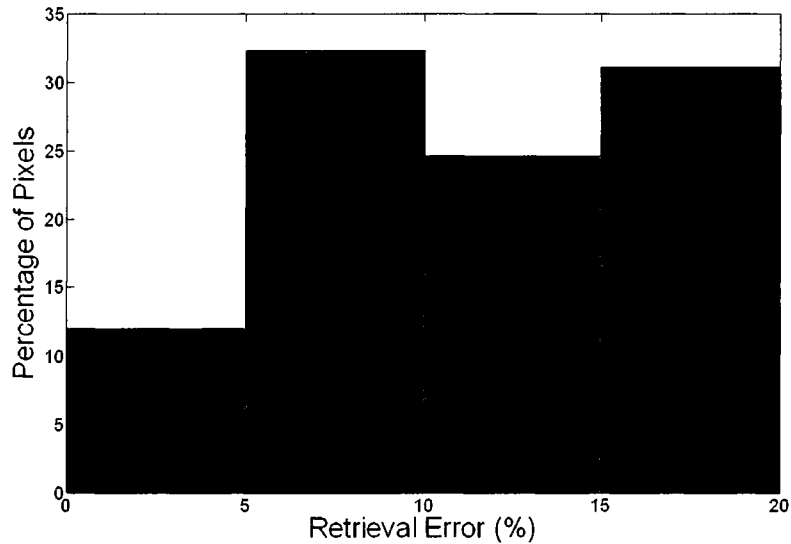


Figure 4.8: Histogram of water vapor density retrieval errors in Figure 4.6 for 3.4 km AGL.

scenarios.

4.4.1 Retrieval Sensitivity to the Time of the *A-priori* Profile

The effect of the time of *a priori* on the retrieval accuracy was investigated by running the OSSE using the 3-D water vapor model output at 2:30 UTC as the *a priori* for the optimal estimation inversion. Figure 4.9 shows the percentage retrieval errors for the 3-D water vapor field retrieved at 3:00 UTC using an 3-D WRF model output at 2:30 UTC, as the *a-priori* profile. The maximum percentage errors for retrieved water vapor densities at 3.4 km is $\sim 15\%$. The retrieval error using the *a-priori* profile from 2:30 UTC was lower than that with *a-priori* profile at 2:00 UTC.

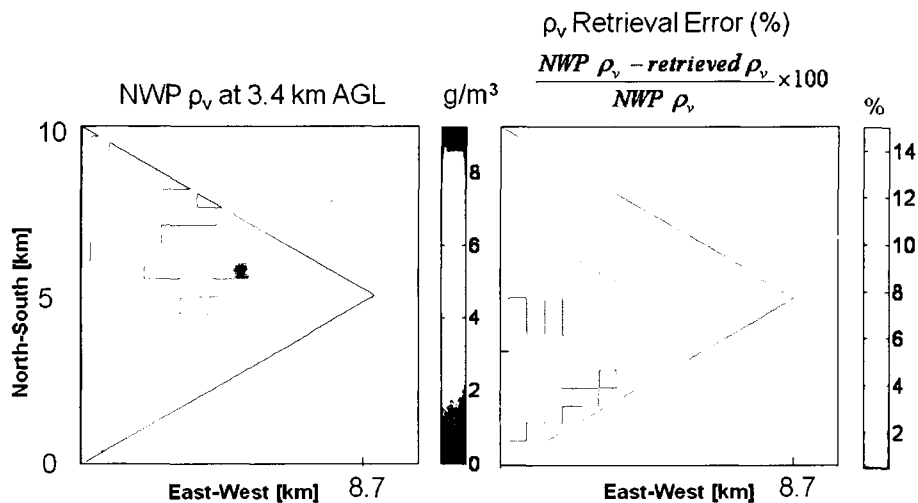


Figure 4.9: (a) WRF model output of the water vapor density at 3.4 km above ground level (AGL) over northwest Indiana at 3:00 UTC. (b) Percentage error of the water vapor density retrieved from synthetic brightness temperature measurements also at 3.4 km AGL with WRF model output at 2:30 UTC used as the *a priori*.

4.4.2 Retrieval Sensitivity to the Location of *A-priori* Profile

For the retrieval in Figure 4.6, the *a priori* water vapor density was the output of the fine-resolution WRF model one hour prior to the retrieval. In order to test the sensitivity of the retrieval algorithm to the quality of the *a priori*, a profile at a single location was instead used to provide a horizontally homogeneous *a priori* water vapor density. This case is analogous to using a radiosonde profile at a single location to provide a homogeneous *a priori* water vapor at each level of the 3-D retrieval. The OSSE was performed using two *a-priori* profiles from (1) one vertex of the triangle formed by the radiometer network, and (2) the median point of the same triangle. Figures 4.10 and 4.11 show the percentage retrieval errors for the 3-D water vapor field retrieved at 3:00 UTC using a vertical profile at one vertex of the triangle at 2:00 UTC and a vertical profile at the median of the triangle at 2:00 UTC, respectively, as

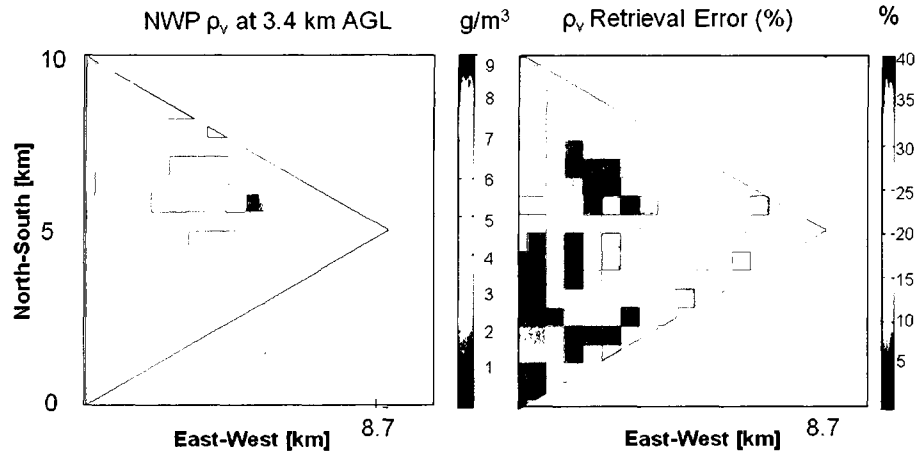


Figure 4.10: (a) WRF model output of the water vapor density at 3.4 km above ground level (AGL) over northwest Indiana at 3:00 UTC. (b) Percentage error of the water vapor density retrieved from synthetic brightness temperature measurements also at 3.4 km AGL with WRF model output at 2:00 UTC at one corner of the triangle used as the *a priori*.

the *a-priori* profile. As expected, the quality of the retrieval depends on that of the *a priori*. The maximum errors for these retrievals were about 35% for the triangle vertex profile and about 22% for the triangle median point profile. It should be noted that in both cases in the majority of pixels, the errors are still below 15-20%. As is intuitively evident, the retrieval error with using the *a-priori* profile from the middle of the triangle was lower than that with the *a-priori* profile at one of the vertices.

4.4.3 Retrieval Sensitivity to the Number of Radiometers in the Network

In order to test the sensitivity of the retrieval algorithm to the number of radiometers in the network, an OSSE was performed for a radiometer network with six radiometers. In this hexagonal configuration, we use an optimally-packed topology for a

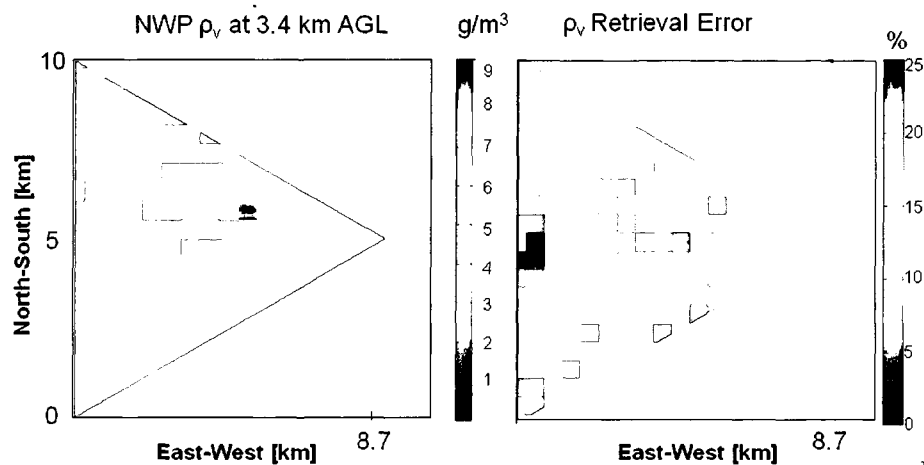


Figure 4.11: (a) WRF model output of the water vapor density at 3.4 km above ground level (AGL) over northwest Indiana at 3:00 UTC. (b) Percentage error of the water vapor density retrieved from synthetic brightness temperature measurements also at 3.4 km AGL with WRF model output at 2:00 UTC at the median point of the triangle used as the *a priori*.

CMR-H radiometer network with six radiometers as shown in figure 4.12, assuming 10 km between each pair of nearest-neighbor nodes. The proposed volumetric scan for the CMR-H radiometer network is to scan every 36° in azimuth (4 angles) and a set of 10 elevation angles from zenith to 30° above the horizon.

Figures 4.13 and 4.14 show the true water vapor density model output on the left and percentage retrieval errors of water vapor density images on the right at 2.2 km and 3.4 km, respectively. The maximum percentage errors for a hexagonal topology is 12% and less than percentage errors that we observe for a three radiometer network. A histogram of the retrieval errors is shown in Figure 4.15, demonstrating that the errors in retrieval of water vapor density for a hexagonal network are mostly from 0-10%. This demonstrates the improvement in the retrieval accuracy when we increase the number of sensors from three to six.

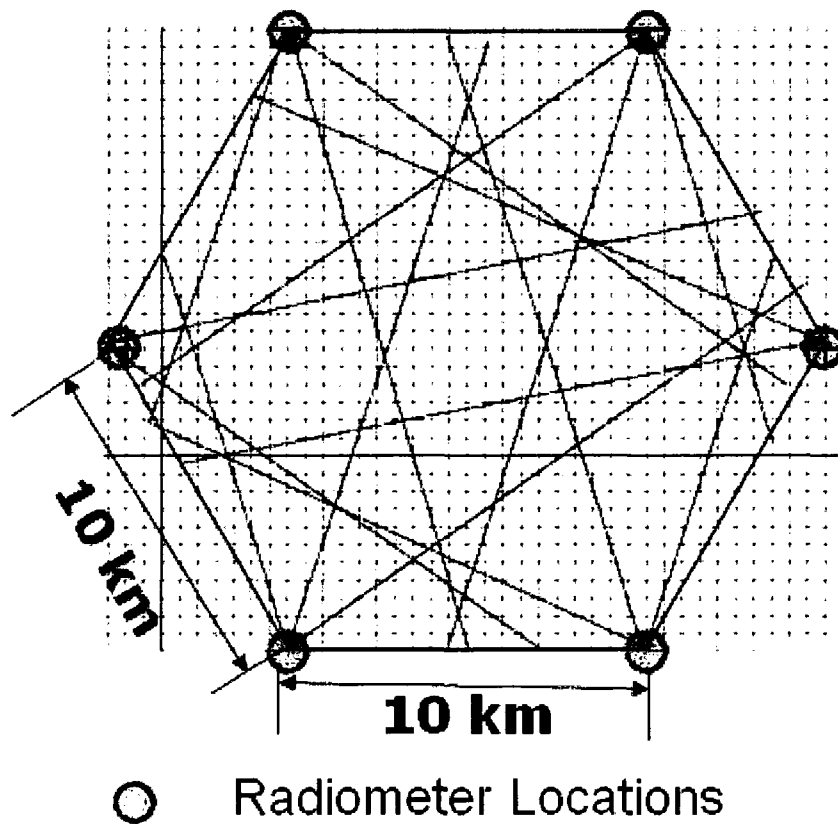


Figure 4.12: Optimal hexagonal topology for a scanning six radiometer network with a 10 km between adjacent nodes

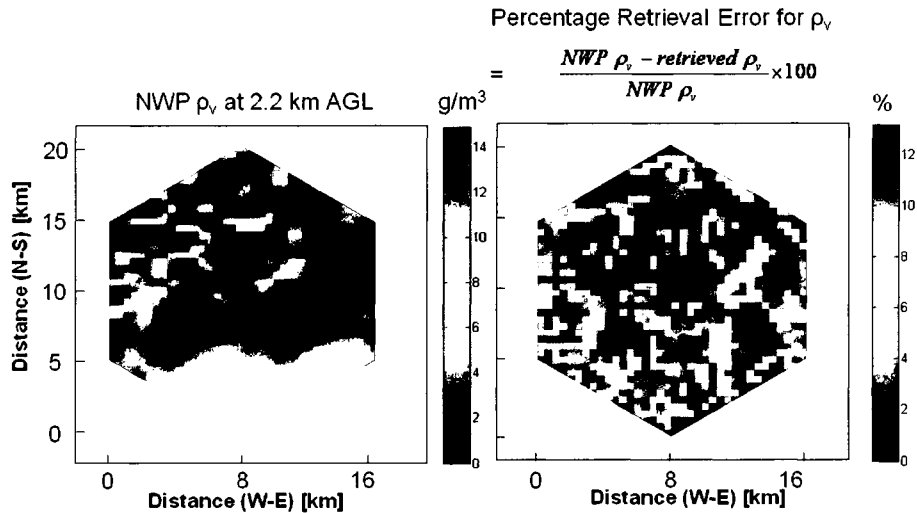


Figure 4.13: (a) WRF model output of the water vapor density at 2.2 km above ground level (AGL) over northwest Indiana at 3:00 UTC. (b) Percentage error of the water vapor density retrieved from synthetic brightness temperature measurements also at 2.2 km AGL with WRF model output at 2:00 UTC used as the *a priori*.

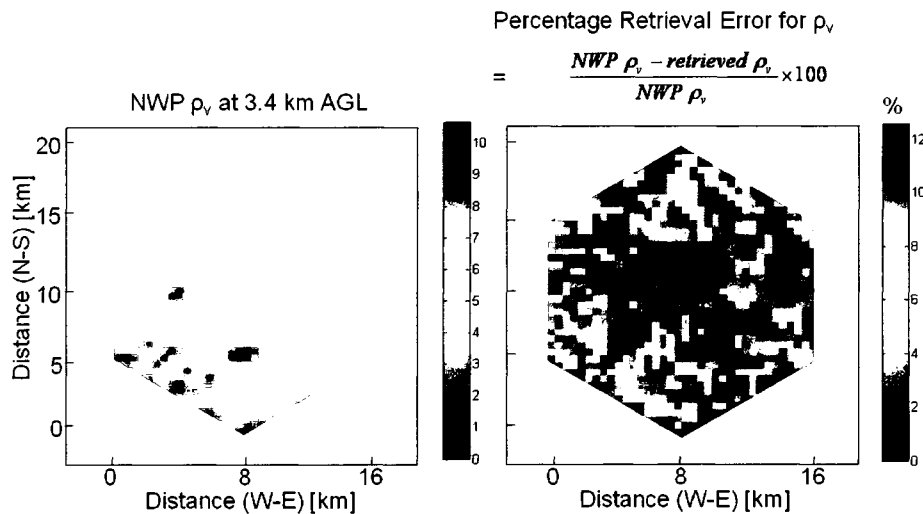


Figure 4.14: (a) WRF model output of the water vapor density at 3.4 km above ground level (AGL) over northwest Indiana at 3:00 UTC. (b) Percentage error of the water vapor density retrieved from synthetic brightness temperature measurements also at 3.4 km AGL with WRF model output at 2:00 UTC used as the *a priori*.

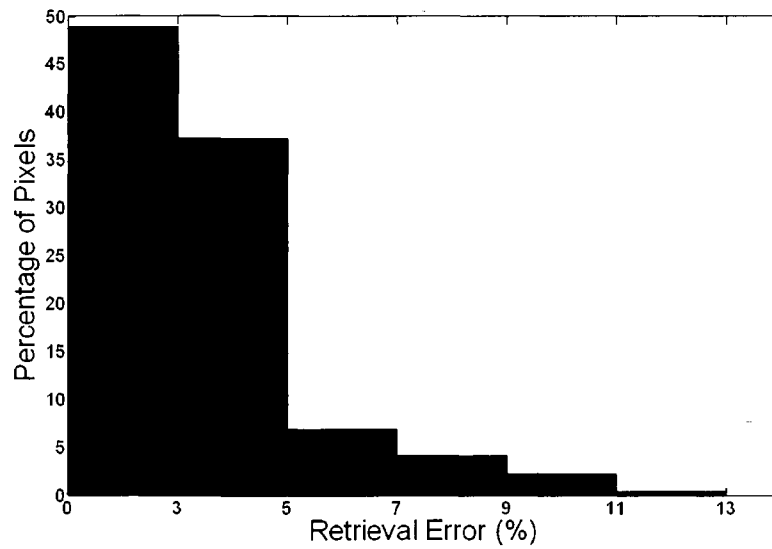


Figure 4.15: Histogram of water vapor density retrieval errors in Figure 4.14 for 3.4 km AGL.

Chapter 5

2-D and 3-D Field Measurements

Three compact microwave radiometers were successfully fabricated and deployed in two field campaigns. Before the fabrication of the third radiometer, a 2-D water vapor measurement was also performed using the two compact microwave radiometers. Brightness temperatures measured by the three radiometers were combined to produce a 3-D water vapor field with spatial resolution of 500 m and temporal resolution of 10 minutes. In this chapter, we will discuss each of these field campaigns and will present 3-D water vapor fields retrieved from the measurements in Oklahoma.

5.1 2-D Water Vapor Measurement

Two field experiments were performed as a first demonstration of the capability of algebraic reconstruction tomography to retrieve the 2-D and 3-D water vapor fields from radiometer network observations with multiple radiometers measuring overlapping atmospheric volumes. In the first field experiment using multiple CMR-Hs to perform scanning measurements, two CMR-H radiometers were deployed at 6-km

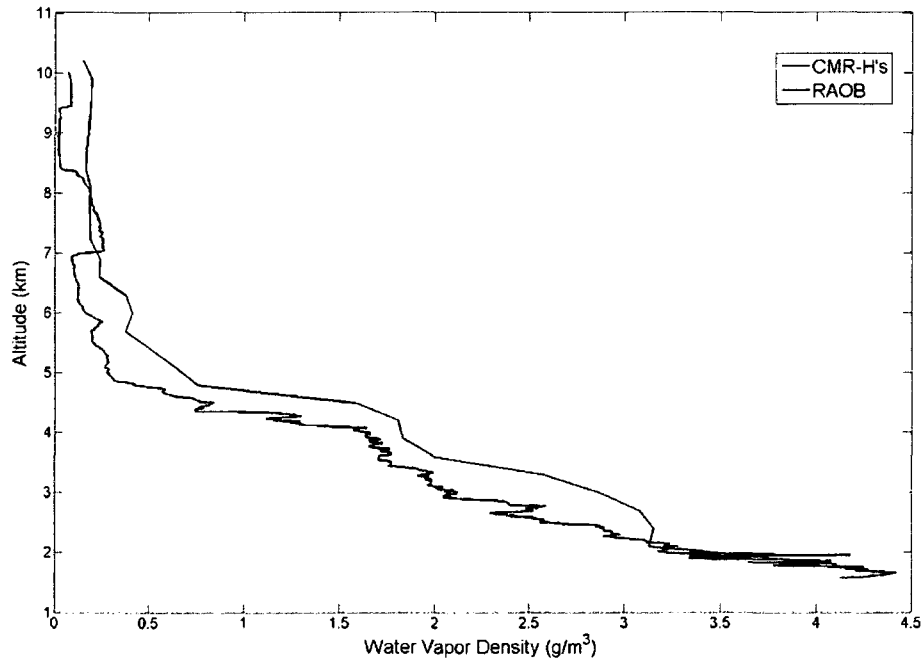


Figure 5.1: Comparison of RAOB and CMR-H retrieved water vapor density profile on October 9, 2007.

spacing near Fort Collins, CO, on October 9, 2007. A radiosonde was launched at 6:00 UTC from the CMR-H1 location. Figure 5.1 shows a comparison of the water vapor profile measured by the radiosonde and that retrieved from the brightness temperatures measured by the CMR-H1 radiometer. At 8:00 UTC, CMR-H1 and CMR-H2 performed 2-D scanning measurements in the vertical plane containing the two radiometers. The water profile retrieved by the RAOB launched two hours earlier was used as the *a-priori* water vapor profile to retrieve the 2-D water vapor image using the overlapping scans of the two CMR-Hs. A time series of 2-D water vapor images was retrieved in the region between the two radiometers, one example of which is shown in Figure 5.3, with a pixel size of 500 x 500 m. Figure 5.2 is the trajectory of the radiosonde.

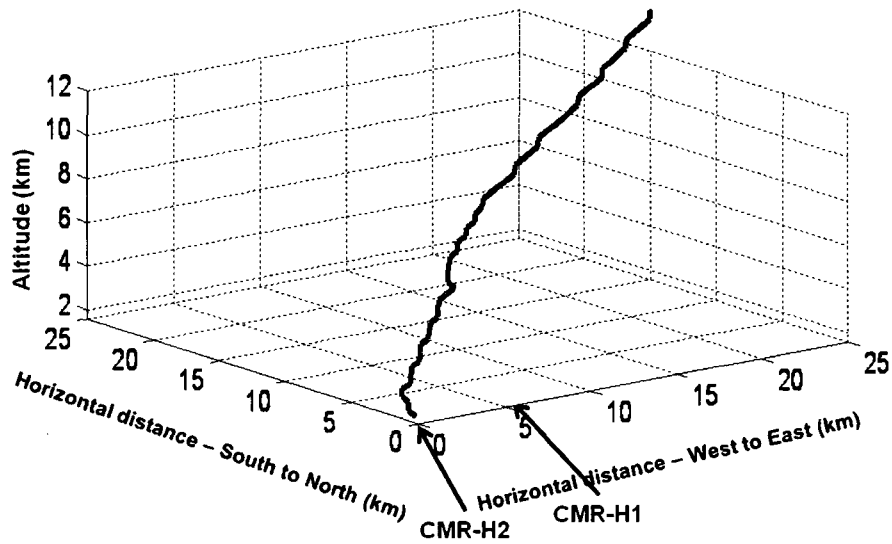


Figure 5.2: Trajectory of the RAOB launched on Oct 9, 2007

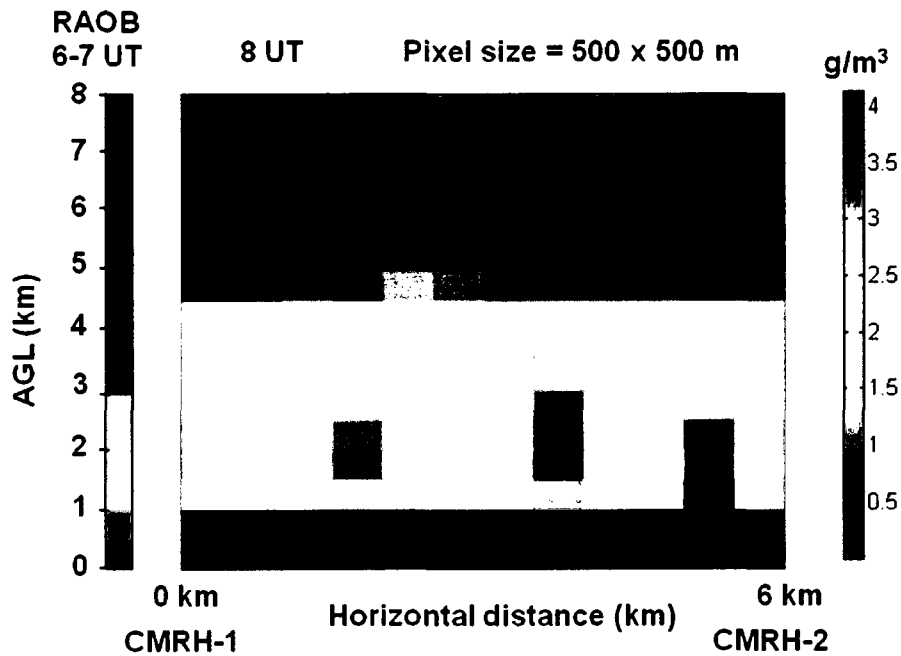


Figure 5.3: 2-D water vapor image retrieved in the region between two CMR-H radiometers at 6-km spacing.

The 2-D measurements confirmed that the water vapor densities with fine resolution (500 m) on a continuous basis using a scanning network of radiometers.

5.2 3-D Water Vapor Measurement

5.2.1 3-D Measurements in Oklahoma

The second field experiment consisted of measurements using three ground-based microwave radiometers deployed in a roughly equilateral triangle at the Atmospheric Radiation Measurement (ARM) Southern Great Plains (SGP) site in Billings, OK, USA from August 25-31, 2008. The locations of the three radiometers are shown in Figure 5.4, in which the CMR-H2 site is located at the ARM-SGP Central Facility. Table 5.1 provides the latitudes and longitudes of the three radiometer locations at the ARM-SGP site. A scanning strategy was chosen as described in 4.3.1 in which each radiometer scans three angles in azimuth (roughly 30° apart) and 10 angles in elevation from zenith to 30° above the horizon. The azimuthal angles for the three-radiometer network are shown as yellow dotted line segments in Figure 5.4. The measured brightness temperatures from each of the three radiometers in the demonstration network were used to retrieve the 3-D water vapor field using algebraic tomographic reconstruction, as described in chapter 3.

Images of retrieved water vapor density at 17:30 UTC on August 31, 2008 at 2, 3 and 4 km AGL are shown in Figs. 5.5, 5.6 and 5.7, respectively. The pixel size in each of these images is 500 x 500 m. The dynamic ranges or horizontal variability of water vapor in each of these images are 12%, 13% and 15%, respectively. The water vapor profile measured by the radiosonde launched at 11:27 UTC was used as

Table 5.1: Radiometer deployment locations in Oklahoma

Radiometer	Latitude	Longitude	Altitude
CMR-H1	36.6513°	97.5670°	305.1 m
CMR-H2	36.6054°	97.4857°	325.2 m
CMR-H3	36.5782°	97.5836°	334.2 m

the horizontally homogeneous *a priori* for the first retrieval at 16:00 UTC, similar to the cases described in 4.4.2. The *a priori* for retrieval of water vapor densities at subsequent times uses Kalman filtering and is updated sequentially from the previous retrieval. These retrieved images clearly demonstrate the capability of a remote sensor network of three CMR-H radiometers to measure the vertical and horizontal variations of water vapor density. Figure 5.8 is a time series of water vapor images at 2 km AGL retrieved every ten minutes from 16:30 UTC to 17:30 UTC. The black ellipse encloses a water vapor structure that moves in the north east direction across the sampled triangular domain. The green ellipses encloses the retrieved location of the water vapor structure and the blue ellipses shows the location of the structure calculated by using the wind speed (2.4 m/s) and direction (5° North East) at 2 km AGL from the RAOB profile at 17:30 UTC.

5.2.2 3-D Measurements in Rome, Italy

The three radiometer network was deployed at the Mitigation of Electromagnetic Transmission Errors induced by Atmospheric Water Vapor Effects (METAWAVE) experiment in Rome, Italy from Sep. 18 to Oct 3, 2008. The objective of this experiment is to use the 3-D water vapor retrieved by the radiometer network to correct for the errors in the transmission fields of the Advanced Synthetic Aperture Radar (ASAR) aboard the ENVISAT. The retrieved 3-D water vapor will have fine spatial

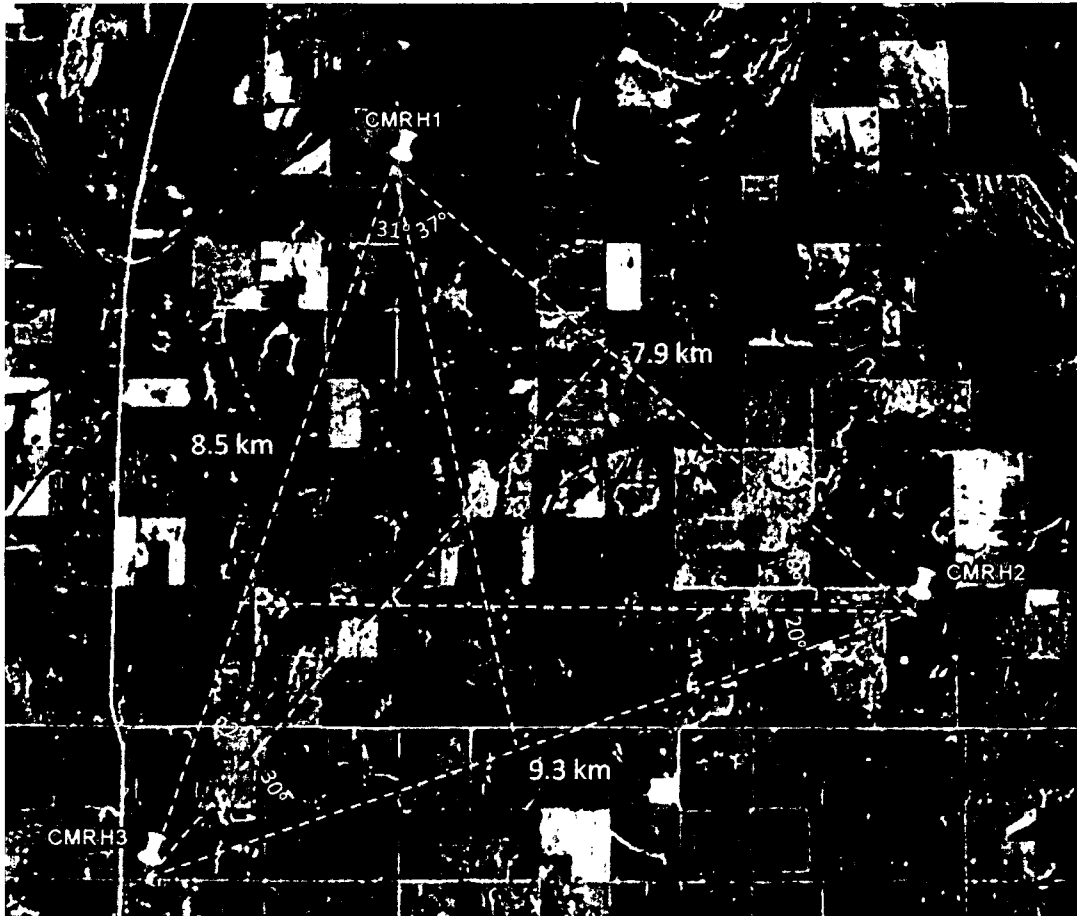


Figure 5.4: Map of the demonstration network of three CMR-H radiometers deployed at the ARM-SGP site near Billings, OK, USA. The three azimuth angles scanned by each radiometer are shown as yellow dashed line segments. CMR-H2 was deployed at the ARM-SGP Central Facility.

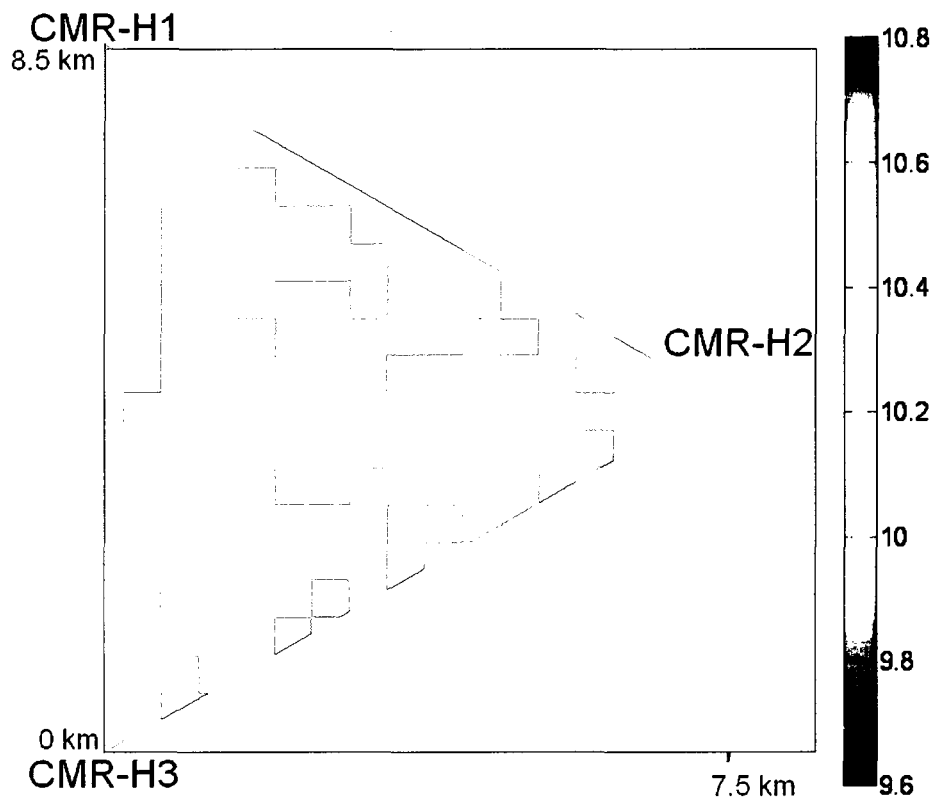


Figure 5.5: Image of water vapor density near the ARM-SGP Central Facility in g/m³ retrieved from brightness temperature measurements at 2 km AGL at 17:30 UTC on August 31, 2008.

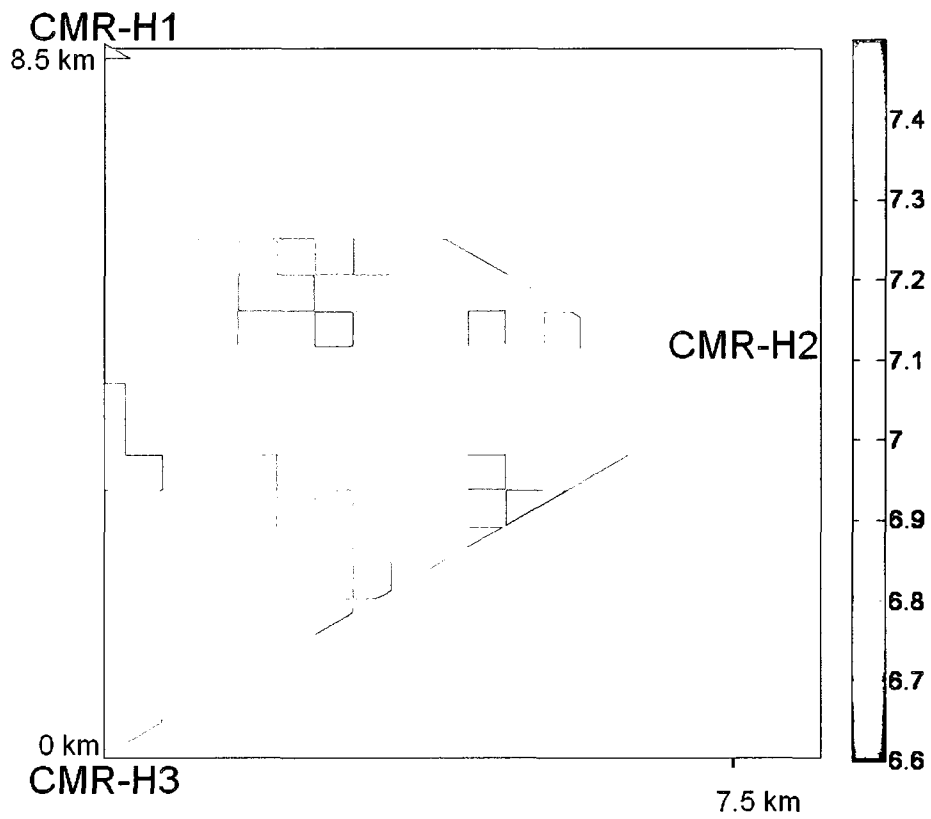


Figure 5.6: Image of water vapor density near the ARM-SGP Central Facility in g/m^3 retrieved from brightness temperature measurements at 3 km AGL at 17:30 UTC on August 31, 2008.

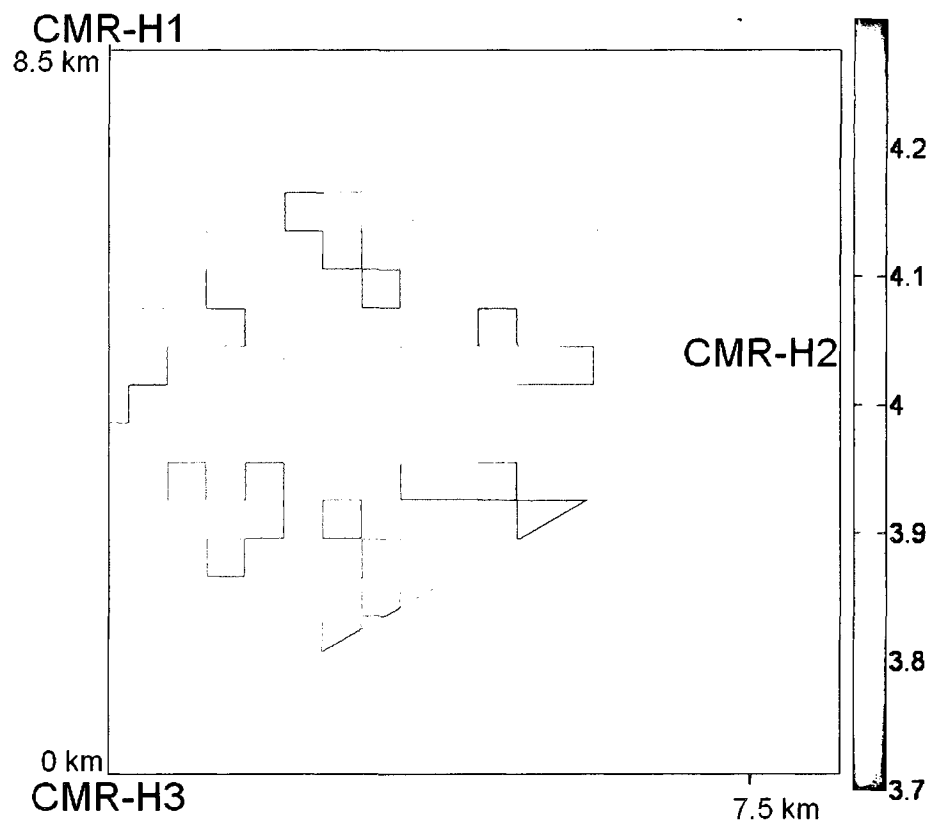


Figure 5.7: Image of water vapor density near the ARM-SGP Central Facility in g/m^3 retrieved from brightness temperature measurements at 4 km AGL at 17:30 UTC on August 31, 2008

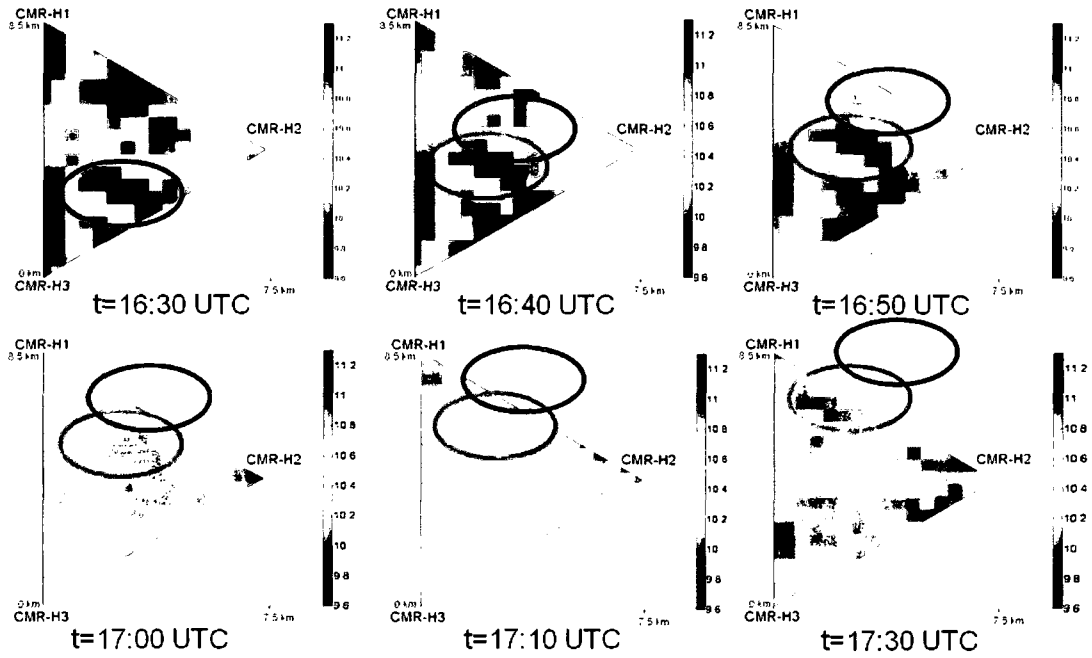


Figure 5.8: Time Series of water vapor densities retrieved at 2 km AGL from 16:30 UTC to 17:30 UTC on August 31, 2008

(~ 500 m) and temporal (~ 10 minutes) resolution. The radiometers were deployed at three locations in Rome, Italy. Figure 5.9 shows the radiometer locations and the azimuth angles scanned by each radiometer. At each azimuth angle the radiometers performed measurements at ten elevation angles. ENVISAT overpasses occurred on Sep 20, 2008 at 20:53 UTC and Oct 3, 2008 at 9:27 UTC. During the first overpass on Sep 20, 2008, the radiometer network performed 3-D measurements from 11:30 UTC to 15:00 UTC and 17:00 UTC to 21:30 UTC. Similarly, during the second overpass on Oct 3, 2008, the radiometer network made measurements from 8:30 to 10:40 UTC and again, from 11:40 to 12:30 UTC. Figure 5.10 shows the radiometer mount on the roof of the Dept. of Electronics Engineering at the University of La-Sapienza. The 3-D retrievals from the measurements performed by the radiometer network from Sep. 23, 2008 until Oct 2, 2008 will be compared with the infrared brightness temperatures measured by the Medium-spectral Resolution, Imaging Spectrometer (MERIS) aboard the ENVISAT as well as measurements by Advanced Microwave Scanning Radiometer (AMSR-E) and Moderate Resolution Imaging Spectroradiometer (MODIS) aboard the AQUA satellite. The measurement analysis to retrieve the 3-D water vapor field is beyond the scope of this *Ph.D.* dissertation.

The thermal stability of the CMR-H2 and CMR-H3 is demonstrated by plotting a long time series ($\sim 20,000$ s) of the temperature on the RF -MCM measured by the Resistance temperature detector attached to the MCM. The temperature stability for both CMR-H2 and CMR-H3 is better than 0.2° . The temperature stability of CMR-H1 was discussed in Flavio's dissertation [30].

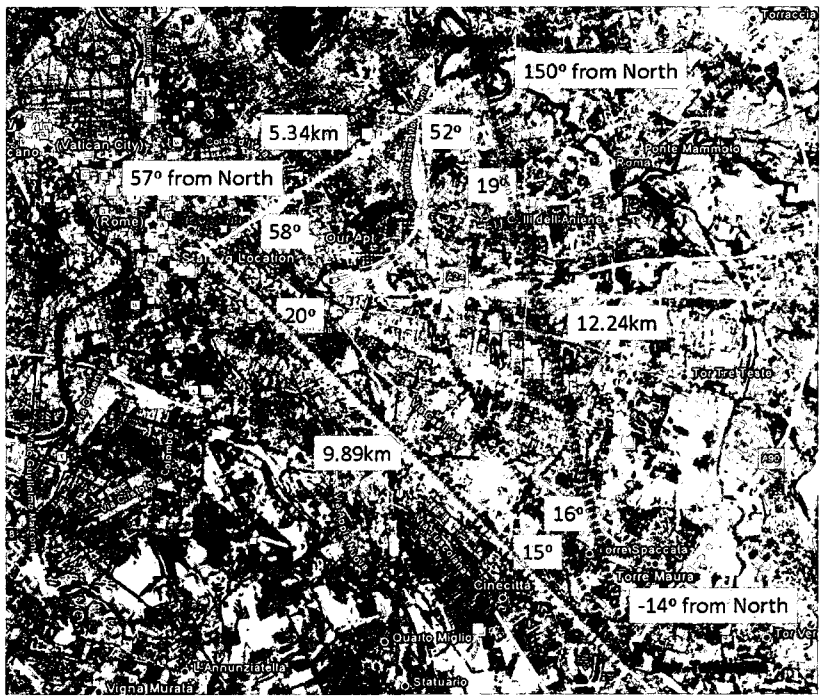


Figure 5.9: Map of the demonstration network of three CMR-H radiometers deployed at the Rome, Italy. The three azimuth angles scanned by each radiometer are shown as red, blue and green dashed line segments.

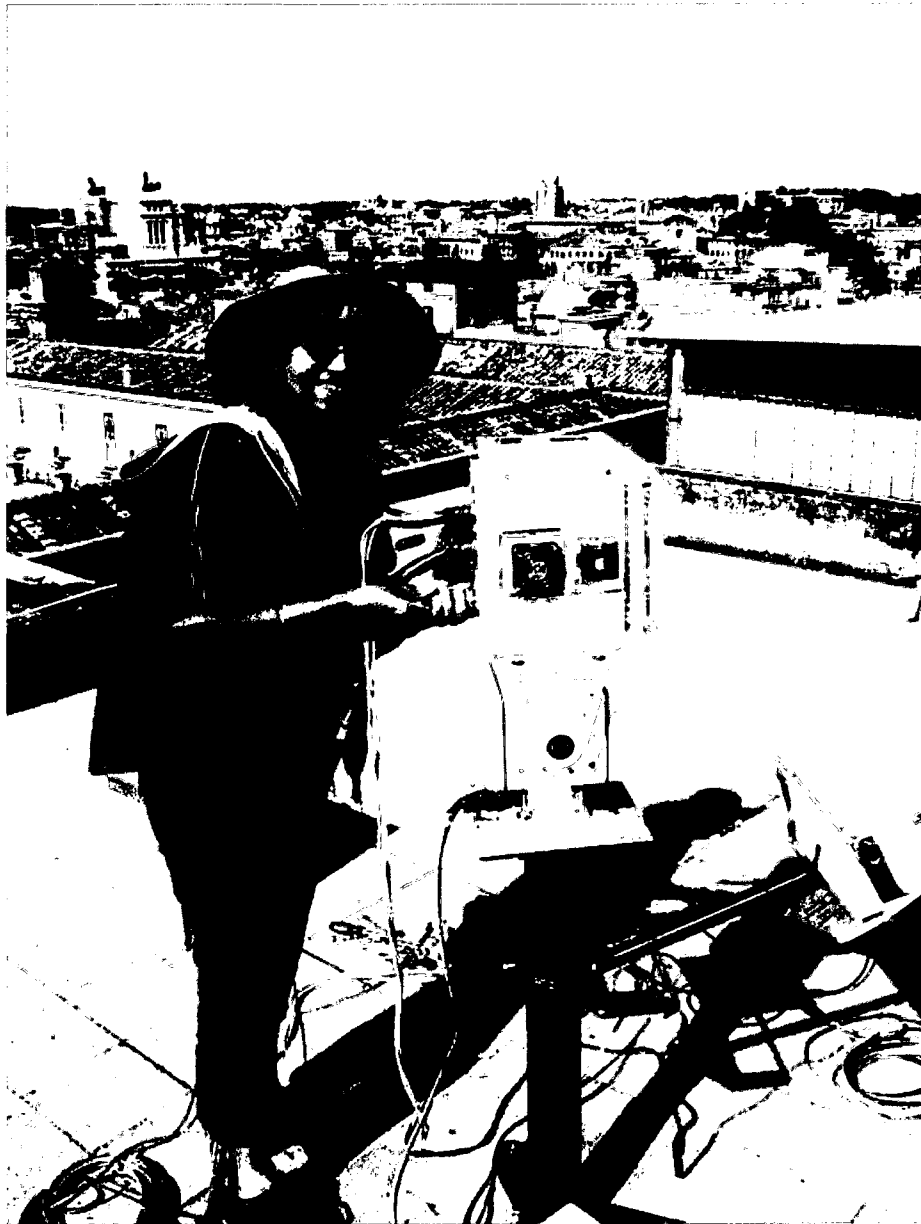


Figure 5.10: Photo of CMR-H2 mounted on the roof of the Dept. of Electronics Engineering at the University of La-Sapienza in Rome, Italy

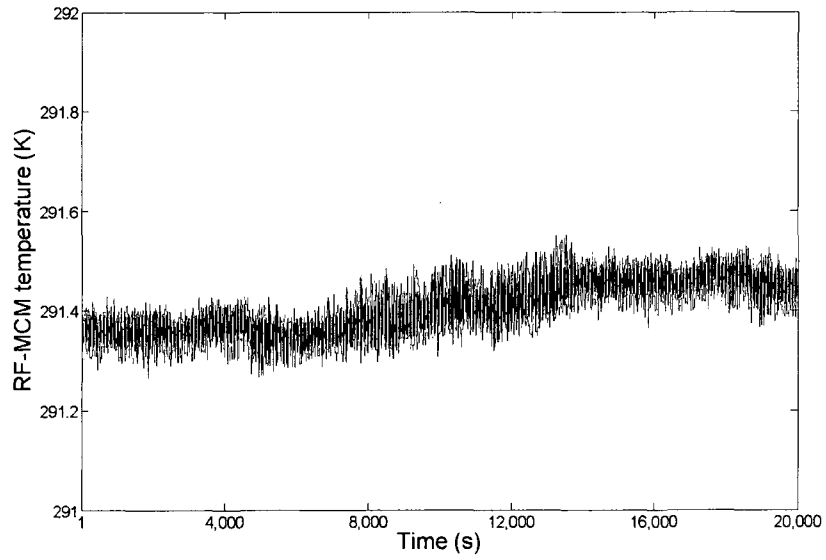


Figure 5.11: Thermal stability of CMR-H2 over 20,000 s

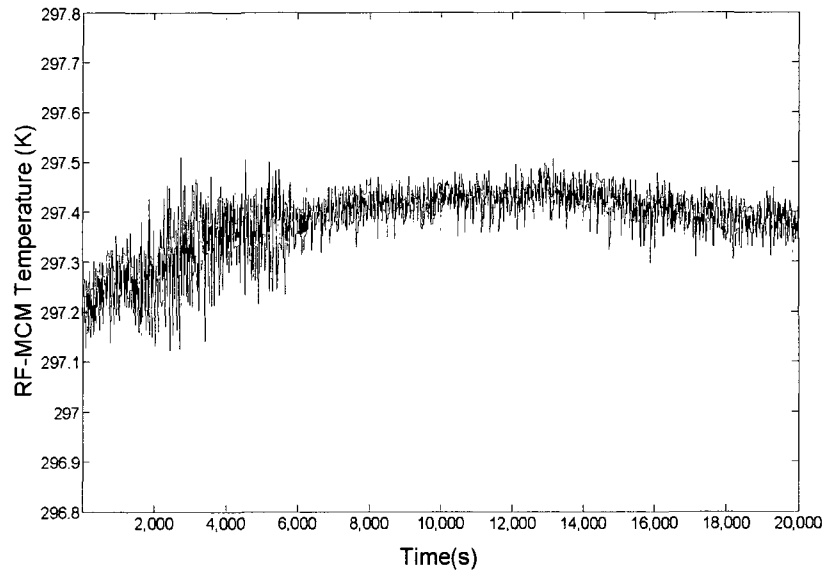


Figure 5.12: Thermal stability of CMR-H3 over 20,000 s

Chapter 6

Summary and Suggestions for Future Work

6.1 Summary

A new technique to measure the 3-D tropospheric water vapor field was developed. This new technique makes use of measurements from a network of scanning CMR-H's. Radiometer measurements of the same volume from multiple perspectives (a variety of azimuth and elevation angles), i.e. different sensor nodes, will be combined using tomographic inversion to retrieve the 3-D water vapor field as a function of time. An OSSE was performed to demonstrate the retrieval of the 3-D water vapor field and compared with WRF model output with a grid resolution of 0.5 km, yielding a retrieval accuracy of the water vapor density in each individual pixel of better than 15-20%. The sensitivity of this retrieval technique to the quality of the *a priori* was tested by using a horizontally homogeneous *a-priori* profile from model output at a vertex and from model output at the median point of the triangular network.

One of the challenging tasks to deploy a radiometer network was to develop a compact, low cost, low mass and rugged radiometer. This motivated the development of the Compact Microwave Radiometer for Humidity Profiling (CMR-H). The CMR-H measures sky brightness temperatures simultaneously at four frequencies, i.e. 22.12, 22.67, 23.25 and 24.50 GHz. Three Compact Microwave Radiometers for Humidity Profiling (CMR-H) were successfully designed, fabricated and tested at the Microwave Systems Laboratory. Each CMR-H is small (24 cm x 18 cm x 16 cm), light-weight (6 kg), robust and consumes little power (maximum of 50 W). The low cost of these microwave radiometers enabled the deployment of scanning microwave radiometers to form a remote sensor network. In such a network, each CMR-H performs a complete volumetric scan, and multiple sensors measure the same atmospheric volume from different perspectives. The brightness temperatures from multiple scanning compact microwave radiometers were combined to retrieve the 3-D water vapor field. The three radiometers were tested and deployed in a variety of ambient conditions with temperatures varying from 0° C to 45° C. The temperature control system was modified and upgraded multiple times to be able to operate the instrument at a variety of conditions. The third radiometer consists of an upgraded multi-chip-module that includes an isolator, includes the IF amplifiers in the same module unlike the first two radiometer modules as described in chapter 2. This design upgrade improves the thermal control the gain sensitive section by including all the active RF components in one single module.

The new retrieval technique combines algebraic tomographic reconstruction, Bayesian optical estimation and Kalman filtering to retrieve the 3-D water vapor field as a function of time. In order to demonstrate the new 3-D retrieval technique and to obtain high spatial and temporal resolution water vapor fields, a ground-based demonstra-

tion network of three radiometers was deployed at the ARM-SGP site in Oklahoma. This network demonstrated the first retrieval of the 3-D water vapor field in the troposphere at fine spatial and temporal resolutions. Currently, the measurements were collected only for a short period of time during the field experiment from August 25-31, 2008. More measurements are needed to demonstrate and validate the remote sensing technique. Field measurements were also performed in Rome, Italy to provide the 3-D water vapor field required for the correction of transmission errors in the Advanced Synthetic Aperture Radar aboard the ENVISAT satellite.

6.2 Suggestions for Future Work

The suggestions for future work can be divided into three main categories

- **Measurements**

1. A variety of meteorological conditions need to be measured using the three radiometer network over the duration of the entire summer in order to be able to sample a variety of atmospheric conditions. Validation of these measurements needs comparison with a fine resolution water vapor output from a Raman Lidar or a high density L-1 GPS receiver network. The Raman Lidar is an active, ground-based laser remote sensing instrument that measures vertical profiles of water-vapor mixing ratio and several cloud- and aerosol-related quantities. Lidar (light detection and ranging) is the optical analog of radar, using pulses of laser radiation to probe the atmosphere [12, 21]. The accuracy of GPS water vapor retrievals ultimately depends on two factors: the accuracy of the measurements, mainly the temperature, needed to estimate the total refractivity

of the neutral atmosphere from the GPS dual frequency carrier phase observables, and the accuracy of the assumptions and/or mathematical models used to perform these functions.

2. The tomographic technique can be tested using different kind of radiometer arrangement topology such as a linear arrangement instead of triangle network of three radiometers. A continuous time series can be measured using a 2-D network of radiometers. This allows monitoring of the diurnal variation of water vapor densities in the volume sampled by the two radiometers.

- **Hardware**

1. It would be extremely beneficial to include a network of radiometers that measures at the frequency channels near the oxygen resonance in the 50 - 60 GHz range. This will allow the measurement of the 3-D temperature fields along with the 3-D humidity fields.

2. Another useful instrument upgrade would be to include the cloud liquid water channel at 31 GHz to measure the liquid water content.

- **Improvements to Retrieval**

1. The retrieval sensitivity test to pressure and temperature can be performed by compute weighting functions for temperature and pressure at these frequency channels.

2. To improve the quality of the 3-D reconstruction, I suggest using the time dependent stochastic inversion approach by formulating it as a space-time interpolation problem. Currently, we use the spatial correlation statistics of model output of water vapor densities to perform kriging in the unsampled pixels.

In the stochastic inversion approach, we calculate the spatial error covariance functions using the spatial statistics of water vapor densities and use it for optimal estimation of the moisture in the unsampled pixels. In other words, we use optimal estimation in space as well as time to compute the water vapor fields. This technique has been implemented in acoustic tomography to reconstruct the temperature and wind velocity fields within the tomographic volume of the horizontal atmospheric layer [43, 44].

- **Assimilation into NWP models**

1. The assimilation of the 3-D water fields into the NWP models is expected to significantly improve the model output. To quantify this improvement, we need to run these models with and without the use of 3-D water fields similar to the analysis performed by Zapotocny et al. [45] to study the effect of radiosonde temperatures, Geostationary Operational Environmental Satellite (GOES) sounder data and GOES infrared cloud-drift winds on the accuracy of the model. Currently, the operational NWP models have a 20 km grid resolution. Assimilating the fine resolution 3-D water vapor fields will need a NWP model with a grid resolution of 500 m which will need an extensive upgrade in the computational resources than is currently available.

Appendix A

Field Operation of CMR-H

The equipment needed for the complete deployment of CMR-H in the field are:

1. CMR-H power supply
2. CMR-H
3. Positioner
4. Positioner power supply
5. Hub
6. Laptop
7. Serial cables
8. USB to serial converters
9. DC Power cables
10. Power Supply AC Cables

The general order of activity during field deployment is

- (1) Equipment Mounting
- (2) Equipment Start up
 - a. Electrical Connections

- b. COM Port Address Acquisition
- c. External Temperature Controller
- d. Virtual Network Computing (VNC) Start up
- e. Radiometer RF Temperature
- f. Radiometer Server Connection
- g. Set Radiometer Voltages
- h. Positioner Server Start up
- i. Calibration target control start up

A.0.1 Hardware connections

The power connections need to be verified before turning on the radiometer power supply. The DC Power cables connecting the power supply to the radiometer are sensitive direction of connection. One needs to make sure that connection on the power supply side is connected to the power supply DC power connector and the DC connector radiometer side is connected to the radiometer. Also, the temperature control cable should be connected to both the radiometer and the CMRH-1 power supply. The temperature controller serial cable is connected from the power supply to the laptop using the USB-to-serial cable. Next, the positioner power supply cable is connected to the positioner, and the positioner serial communication cable to the laptop using another USB-to-serial cable. An Ethernet cable from the radiometer to a hub. The Ethernet cable from the laptop should also be connected to the hub. Long Ethernet distances have been tested and verified to operate using a Linksys Workgroup Switch (model EZXS55W).

A laptop is used to control the external temperature controller, positioner con-

troller and calibration temperature logger. On the laptop, run the external temperature controller software (TC24-25-RS232.exe for CMR-H1 and CMR-H2, TC36-25-RS232.exe for CMRH3) . The controller output should not be turned on at this point.

A.0.2 Temperature control

We need to wait for the external temperature to stabilize naturally, then enter a set point very close to the temperature to which the instrument has stabilized. Once we have this set point, let the temperature controller maintain control of the temperature by turning the output on in Figure A.1. (NOTE: Ambient conditions of wind, sudden air temperature changes and solar radiation may require you to change the set point to prevent overloading of the Peltier elements. Overloaded Peltier elements result in a temperature that cannot be maintained at steady state. Measurement consistency is reduced without a steady temperature.)

A.0.3 Communication with radiometer embedded computer

Now we run the VNC viewer and type the IP address of the CMR-H embedded PC. (Using the keyboard and display connected to the radiometer we can determine the IP address by going to the command prompt, type ipconfig all). If the computer inside the radiometer is booted up, VNC will show the radiometer computer desktop immediately. Once the radiometer computer is online, we can open the RF temperature controller software and enter the address assigned to the controller into the appropriate box on the software display. Again, we need to wait for the temperature to stabilize on its own to fix a set point. Once you think the temperature is stable, fix a set point and turn the output 'on'. (NOTE: A set point between 20 and 30 degrees

C is desirable, but not required. Of more importance is to assign a set point that when a stable temperature has settled, results in an output control value that gives the Peltier controller plenty of headroom to heat or cool.)

When we turn the radiometer server ‘ON’ a window will appear as shown in Figure A.2, the window on the right appears after you click ok on 4 message boxes confirming the voltage levels. CAUTION: The following order is very important to prevent damage to the radiometer RF circuitry. To view the calibrated values we have to click on the radio button labeled “converted” to give measured analog voltages in engineering units. If we click on the DIO and DA voltages button the biasing window on the left appears. First, we set drain voltage for the LNA followed by the gate voltage. For CMR-H3, the software controlled bias voltages are the drain voltage for the LNA and the Voltage controlled oscillator tuning voltage.

A.0.4 Positioner Control

Next, we have to run the positioner control software and the Calibration target control software to have them ready before we start performing measurements. The QPT-50IC positioner is controlled by the PTR-2090 Remote Emulator. When we run the PTR-2090, a window appears as shown in Figure A.3. Make sure that the correct COM port is selected (the port value can be a value up to 8). If yes, click start and the serial communication is established with the positioner. Once the communication is established, the Jog/Limits, Offsets , Tours, Move To etc. get highlighted so that we can use them. Tours have been preset for the positioner software. Tour 1 is for tip curve and Tour 2 is for scanning routine.

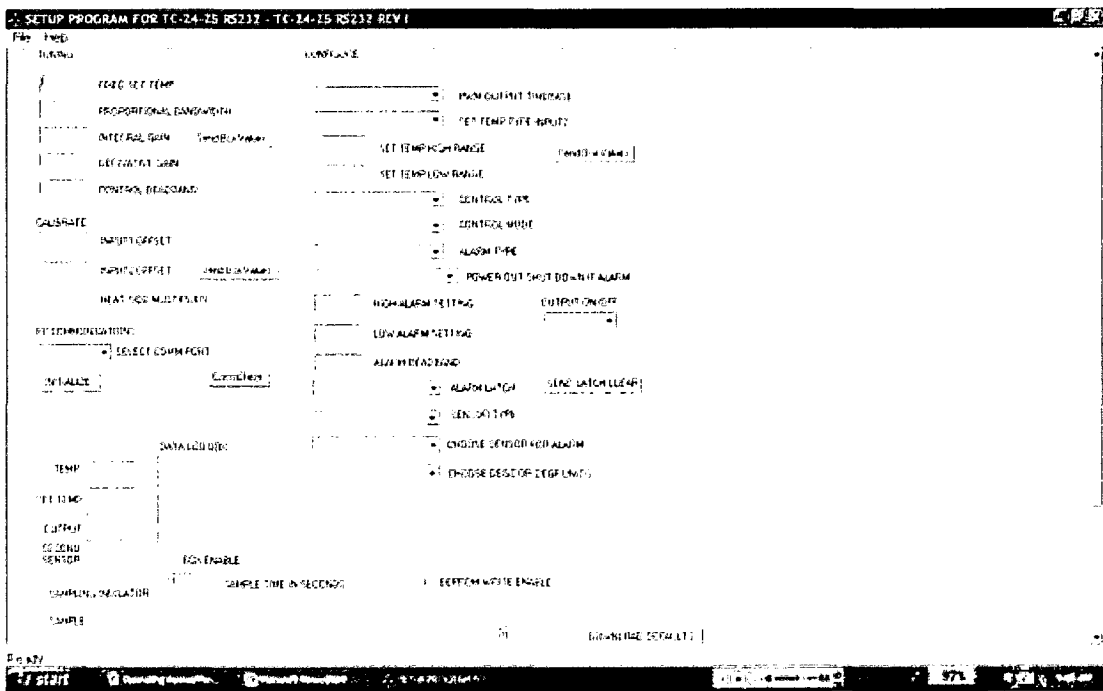


Figure A.1: Temperature Controller Window

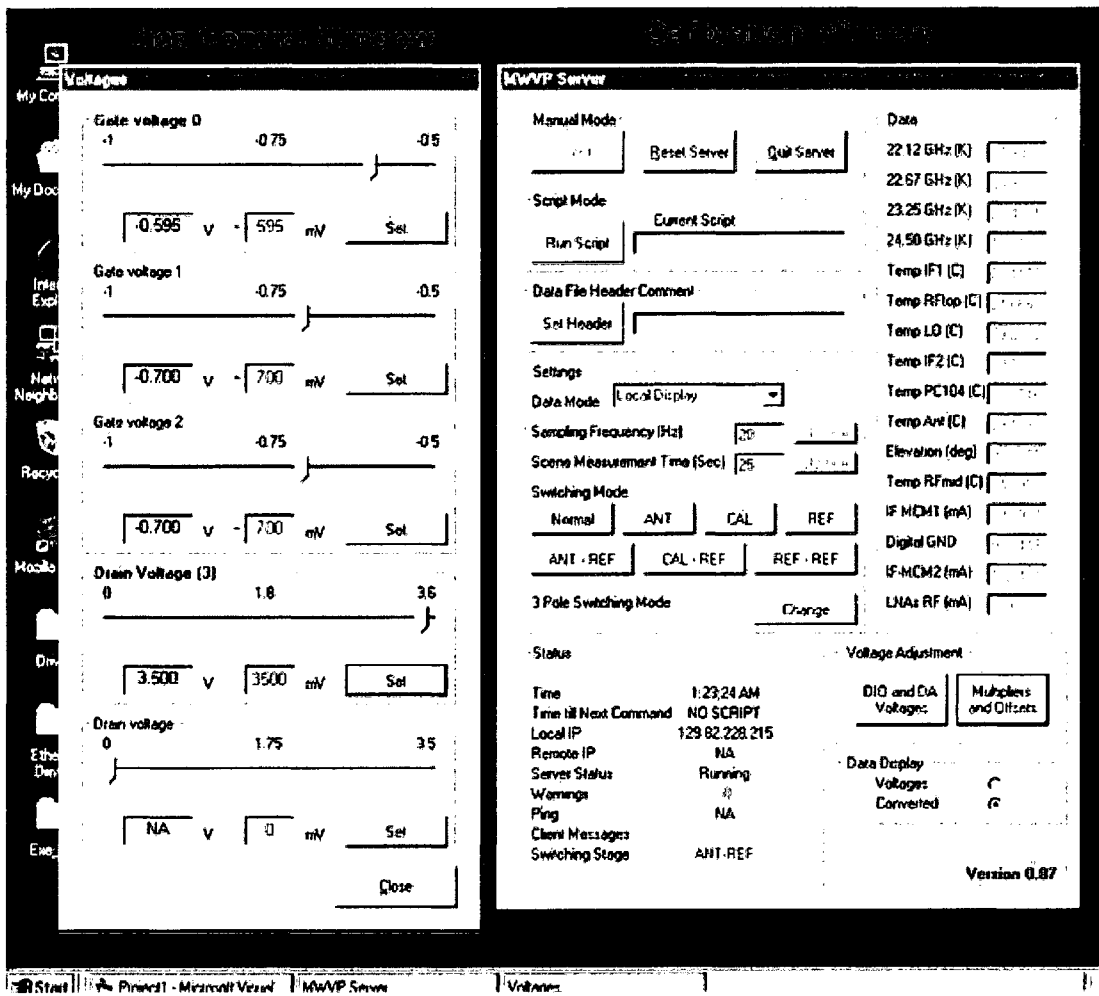


Figure A.2: CMR-H server and biasing control window

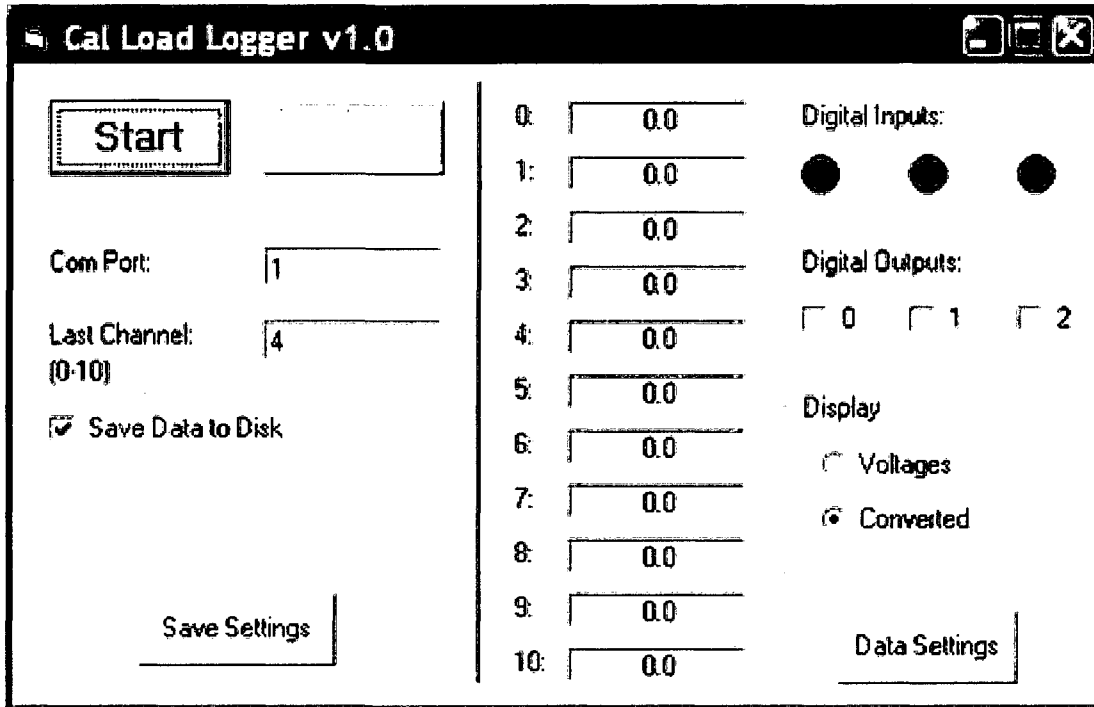


Figure A.4: Calibration load logger window

A.0.5 Calibration target control

Cal target software is located on the desktop and is named “Cal Load Logger”. A window appears as shown in figure A.4. Any COM port number can be used with this software. Always make sure the “Save data to disk” checkbox is checked. If this box is not checked, data from the cal target will not be saved. However, data will be displayed. Hit START when the positioner is moving toward the absorber. When the positioner moves back to the starting position of the tip curve calibration, hit STOP.

Bibliography

- [1] K. A. Emanuel, D. Raymond, A. Betts, L. Bosart, C. Bretherton, K. Droegemeier, B. Farrell, J. M. Fritschad, R. Houze, M. LeMone, D. Lilly, R. Rotunno, M. Shapiro, R. Smith, and A. Thorpe. "Report of the first prospectus development team of the us weather research program to NOAA and the NSF". *Bull. Amer. Meteor. Soc.*, 76(8):1194–1208, Aug. 1995.
- [2] L. Xin and G. W. Reuter. "Numerical simulation of the effects of mesoscale convergence on convective rain showers". *Mon. Wea. Rev.*, 124:2828–2842, 1996.
- [3] N. A. Crook. "Sensitivity of moist convection forced by boundary layer processes to low-level thermodynamic fields". *Mon. Wea. Rev.*, 124:1767–1785, 1996.
- [4] S. K. Park and K. Droegemeier. "Sensitivity analysis of a moist 1d eulerian cold model using automatic differentiation". *Mon. Wea. Rev.*, 127:2180–2196, 1999.
- [5] S. K. Park and K. Droegemeier. "Sensitivity analysis of a 3d convective storm: Implications for variational data assimilation and forecast error". *Mon. Wea. Rev.*, 128:140–159, 2000.

- [6] A. Hense, G. Adrian, C. Kottmeier, C. Simmer, and V. Wulfmeyer. "Quantitative precipitation forecast". *Report For Priority Program of the German Research Foundation*.
- [7] W. F. Dabberdt and T.W. Schlatter. "Research opportunities from emerging atmospheric observing and modeling capabilities ". *Bull. Amer. Meteor. Soc.*, 77(2):305–323, Feb. 1996.
- [8] F. Guichard, D. Parsons, and E. Miller. "Thermodynamic and radiative impact of the correction of sounding humidity bias in the tropics ". *J. Climate*, 13(20):3611–3624, Oct. 2000.
- [9] D. Turner, B. M. Lesht, S. A. Clough, J. C. Liljegren, H. E. Revercomb, and D. C. Tobin. "Dry bias and variability in väisälä RS80-H radiosondes: The ARM experience ". *J. Atmos. Oceanic Technol.*, 20(1):117–132, Jan. 2003.
- [10] T. M. Weckwerth. "The effect of small-scale moisture variability on thunderstorm initiation". *Mon. Wea. Rev.*, 128(12):4017–4030, Dec. 2004.
- [11] J. Wang and L. Zhang. "Systematic errors in global radiosonde precipitable water data from comparisons with ground-based GPS measurements ". *J. Climate*, 21(10):2218–2238, May 2008.
- [12] R. Ferrare, D. Turner, M. Clayton, B. Schmid, J. Redemann, D. Covert, R. Elleman, J. Ogren, E. Andrews, J. E. M. Goldsmith, and H. Jonsson. "Evaluation of daytime measurements of aerosols and water vapor made by an operational raman lidar over the southern great plains ". *J. Geophys. Res.*, 111, Jan. 2006.

- [13] M. Grzeschik, H.-S. Bauer, V. Wulfmeyer, D. Engelbart, I. Mattis U. Wandinger, D. Althausen, R. Engelmann, M. Tesche, and A. Riede. "Four-dimensional variational analysis of water vapor Raman lidar data and their impact on mesoscale forecasts ". *J. Atmos. Oceanic Technol*, 25(8):1437–1453, Aug. 2000.
- [14] A. Flores, G. Ruffini, and A. Ruis. "4D tropospheric tomography using gps slant wet delays ". *Ann. Geophys.*, 18(2):223–234, Feb. 2000.
- [15] A. E. MacDonald, Y. Xie, and R. H. Ware. "Diagnosis of three dimensional water vapor using slant observations from a gps network ". *Mon. Wea. Rev.*, 130(2):386–397, Feb. 2002.
- [16] G. Beyerle, T. Schmidt, J. Wickert, S. Heise, M. Rothacher, G. König-Langlo, and K. B. Lauritsen. "Observations and simulations of receiver-induced refractivity biases in gps radio occultation ". *J. Geophys. Res*, 111, 2006.
- [17] J. Wickert, C. Reigber, G. Beyerle, R. König, C. Marquardt, T. Schmidt, L. Grunwaldt, R. Galas, T. K. Meehan, W. G. Melbourne, and K. Hocke. "Atmosphere sounding by gps radio occultation: First results from champ". *Geophys. Res. Lett*, 28(17):3263–3266, Jan. 2001.
- [18] A. Somieski, B. Buerki, A. Geiger, H.-G. Kahle, E. C. Pavlis, H. Becker-Ross, S. Florek, and M. Okruss. "Tropospheric water vapor from solar spectrometry and comparison with jason microwave radiometer measurements ". *J. Geophys. Res*, 111, 2006.
- [19] P. W. Rosenkranz. "Retrieval of temperature and moisture profiles from AMSU-A and uppercaseAMSU-B measurements ". *IEEE Trans. Geosci. Remote Sens.*, 39(11):2429–2435, Nov. 2001.

- [20] J. L. Machol, T. Ayers, K. T. Schwenz, K. W. Koenig, R. M. Hardesty, C. J. Senff, M. A. Krainak, J. B. Abshire, H. E. Bravo, and S. P. Sandberg. "Preliminary measurements with an automated compact differential absorption lidar for the profiling of water vapor". *Appl. Opt.*, 43(15):3110–3121, May 2004.
- [21] J. Braun. "Remote sensing of atmospheric water vapor with the global positioning system". *Ph. D. dissertation, University of Colorado, Boulder*, 2004.
- [22] D. Cimini, T. J. Hewison, L. Martin, J. Güldner, C. Gaffard, and F. S. Marzano. "Temperature and humidity profile retrievals from ground-based microwave radiometers during TUC". *Meteor. Z.*, 15(5):45–56, Feb. 2006.
- [23] T. J. Hewison. "1D-VAR retrieval of temperature and humidity profiles from a ground-based microwave radiometer". *IEEE Trans. Geosci. Remote Sens.*, 45(7):2163–2168, Jul. 2007.
- [24] T. M. Weckwerth and D. B. Parsons. "A review of convection initiation and motivation for IHOP 2002". *Mon. Wea. Rev.*, 134(1):5–22, Jan. 2006.
- [25] M. N. Deeter and K. F. Evans. "Mesoscale variations of water vapor inferred from millimeter-wave imaging radiometer during TOGA COARE". *J. Appl. Meteor.*, 36(2):183–188, Feb. 1997.
- [26] H. Seko, H. Nakamura, Y. Shoji, and T. Iwabuchi. "The meso- γ scale water vapor distribution associated with a thunderstorm calculated from a dense network of GPS receivers". *J. Meteor. Soc. Japan*, 82:569–586, Mar. 2004.
- [27] D. H. Lenschow and B. B. Stankov. "Length scales in the convective boundary layer". *J. Atmos. Sci.*, 43(12):1198–1209, Jun. 1986.

- [28] F. Iturbide-Sanchez, S. C. Reising, and S. Padmanabhan. "A miniaturized spectrometer radiometer based on mmic technology for tropospheric water vapor profiling". *IEEE Trans. Geosci. Remote Sens.*, 44(7):2181–2193, Jul. 2007.
- [29] S. Padmanabhan, S. C. Reising, F. Iturbide-Sanchez, and J. Vivekanandan. "Retrieval of 3-D water vapor field using a network of scanning compact microwave radiometers". *Proc. IEEE Geosci. Remote Sens. Symp, Barcelona, Spain*, pages 251–254, Jul. 2007.
- [30] F. Iturbide-Sanchez. "Design, fabrication and deployment of a miniaturized spectrometer radiometer based on MMIC technology for tropospheric water vapor profiling". *Ph. D. dissertation, University of Massachusetts, Amherst*, 2007.
- [31] J. Randa, D. K. Walker, A. E. Cox, and R. L. Billinger. "Errors resulting from the reflectivity of calibration targets". *IEEE Trans. Geosci. Remote Sens.*, 43(1):50–58, Jan. 2005.
- [32] L. M. Miloshevich, H. Vömel, D. N. Whiteman, B. M. Lesht, F. J. Schmidlin, and F. Russo. "Absolute accuracy of water vapor measurements from six operational radiosonde types launched during AWEX-G and implications for AIRS validation". *J. Geophys. Res.*, Apr. 2006.
- [33] J. A. Schroeder and E. R. Westwater. "Guide to microwave weighting function calculations". *U.S. Dept. of Commerce, National Oceanic and Atmospheric Administration, Environmental Research Laboratories, Wave Propagation Laboratory*, Jul. 1992.
- [34] M. A. Janssen. *Introduction to Passive Remote Sensing*. New York: Wiley-Interscience, 1993.

- [35] F. T. Ulaby, R. K. Moore, and A. K. Fung. *Microwave Remote Sensing; Active and Passive*. London, UK: Addison-Wesley, 1981.
- [36] C. D. Rodgers. *Inverse Methods for Atmospheric Sounding: Theory and Practice*. World Science Publishing, 2000.
- [37] A. C. Kak and M. Slaney. *Principles of Computerized Tomographic Imaging*. New York: IEEE Press, 1988.
- [38] A. V. Bosisio and G. Drufuca. "Retrieval of two-dimensional absorption coefficient structure from a scanning radiometer at 23.8 ghz". *Radio Sci.*, 38(3), 2003.
- [39] P. W. Rosenkranz. "Water vapor microwave continuum absorption: A comparison of measurements and models". *Radio Sci.*, 34(4):1025, Jul. 1999.
- [40] J. C. Liljegren, S.-A. Boukabara, K. Cady-Pereira, and S. A. Clough. "The effect of the half-width of the 22-ghz water vapor line on retrievals of temperature and water vapor profiles with a 12-channel microwave radiometer". *IEEE Trans. Geosci. Remote Sens.*, 43(5):1102–1108, May 2005.
- [41] R. Webster and M. Oliver. *Geostatistics for Environmental Scientists*. London, UK: John Wiley, 2000.
- [42] R. Olea. "A six-step practical approach to semivariogram modeling". *Stoch. Environ. Res. Risk Assess.*, 20:317–328, 2003.
- [43] S. Vecherin, V. E. Ostashev, G. H. Geodecke, D. K. Wilson, and A. Voronovich. "Time-dependent stochastic inversion in acoustic travel-time tomography of the atmosphere". *J. Acoust. Soc. Am.*, 119(5):2579–2588, May 2006.

- [44] S. Vecherin, V. E. Ostashev, A. Ziemann, D. K. Wilson, K. Arnold, and M. Barth. "Tomographic reconstruction of atmospheric turbulence with the use of time-dependent stochastic inversion". *J. Acoust. Soc. Am.*, 122(3):1416–1425, Sep. 2007.
- [45] T. H. Zapotocny, S. J. Nieman, P. W. Menzel, J. P. Nelson III, J. A. Jung, E. Rogers, D. F. Parrish, G. J. Dimego, M. Baldwin, and T. J. Schmit. "A case study of the sensitivity of the eta data assimilation system". *Wea. Forecasting*, 15:603–622, 2000.